ÉTUDE DES ACTIONNEURS POLYMÈRES SOUPLES BASÉS SUR UNE TRANSITION DE PHASE ORDRE-DÉSORDRE

par

Feijie Ge

Thèse présentée au Département de chimie en vue

de l'obtention du grade de Philosophia doctor (Ph.D.)

FACULTÉ DES SCIENCES

UNIVERSITÉ DE SHERBROOKE

Sherbrooke, Québec, Canada, Septembre 2019

STUDY OF SOFT POLYMER ACTUATORS DRIVEN BY AN ORDER-DISORDER PHASE TRANSITION

by

Feijie Ge

A Thesis

Presented to the Département de chimie

in Partial Fulfillment of the Requirements for the Degree of

Doctor of Philosophy (Ph.D.)

FACULTÉ DES SCIENCES

UNIVERSITÉ DE SHERBROOKE

Sherbrooke, Québec, Canada, September 2019

Le 26 Septembre 2019

le jury a accepté la thèse de monsieur Feijie Ge
dans sa version finale.

Membres du jury

Professeur Yue Zhao
Directeur de recherche
Département de chimie

Professeur Suzanne Giasson
Évaluateur externe
Université de Montréal

Professeur Armand Soldera
Évaluateur interne
Département de chimie

Professeur Patrick Ayotte
Évaluateur interne
Département de chimie

Professeur Claude Spino
Président-rapporteur
Département de chimie

SOMMAIRE

Les actionneurs souples à base de polymère pouvant être actionnés de manière réversible suscitent un grand intérêt car ils peuvent être construits à partir d'une vaste source de polymères et être déclenchés par divers types de stimuli pour la production répétée de travaux physiques. Parmi ceux-ci, les actionneurs thermo-sensibles et photo-sensibles à base de polymères semi-cristallins (SCPs) et / ou de polymères à cristaux liquides (LCPs) se développent rapidement en raison de leurs applications potentielles en tant que dispositifs intelligents dans de nombreux domaines. Les chercheurs ont consacré des efforts considérables ces dernières années à la mise au point de nouveaux matériaux et de nouvelles fonctions basés sur les SCPs et les LCPs, mais la demande de construction d'actionneurs en polymère robustes dotés de fonctions avancées utilisant des matériaux facilement disponibles et des stratégies faciles n'a pas été satisfaite. Le but principal de cette thèse est de développer et d'étudier de tels actionneurs polymères fonctionnels avancés et contrôlables thermiquement ou par la lumière afin de produire de l'énergie mécanique par un actionnement réversible, en utilisant du poly (éthylène-acétate de vinyle) (EVA) semi-cristallin disponible dans le commerce et un type de LCP photoréticulable avec addition de petites quantités d'additifs générant de la chaleur. Nos approches étaient simples, pratiques et robustes, car nous n'avions utilisé qu'un laser ou un substrat isothermique pour réguler plusieurs comportements d'actionnement réversibles de pointe. L'utilisation d'EVA a donné lieu à deux projets présentés dans les chapitres 1 et 2, respectivement, en tant que première partie de cette thèse. Dans cette partie, deux comportements d'actionnement réversibles ont été décrits. Le premier est contrôlé par une commutation marche / arrêt du laser, tandis que le second est auto-entretenu sur un substrat isotherme. Les deux comportements sont associés à un gradient de température établi dans la direction de l'épaisseur de l'actionneur et entraîné par une transition de phase cristallisation – fusion. La deuxième partie est présentée au chapitre 3 et démontre qu'une bande de LCP monolithique réticulée de manière non uniforme peut fonctionner comme un photoactionneur multifonctionnel commandé par une transition de phase LC – isotrope.

Dans le premier chapitre, nous avons préparé un type d'actionneur optique contenant des nanoparticules d'or basé sur une bande d'EVA étirée recevant des cristallites orientés. Lors de l'irradiation avec un laser (longueur d'onde de 532 nm), la résonance plasmonique de surface (SPR) de nanoparticules d'or (AuNP) est activée pour libérer de la chaleur qui fond partiellement les cristallites à T_{light}. Les cristallites dont la température de fusion (T_m) est inférieure à T_{light} sont fondus en tant que domaine d'actionnement afin de contracter la bande de manière asymétrique en raison du gradient de température, tandis que les cristaux de T_m supérieurs à T_{light} soutiennent en tant que cadre. Lorsque le laser est retiré, la recristallisation orientée du domaine d'actionnement induit une expansion dans la direction d'étirage pour détendre la bande. Les résultats montrent que la luminosité, la force mécanique optique, l'amplitude d'actionnement et la vitesse d'activation peuvent être réglés en ajustant l'intensité du laser, le contenu en AuNPs, l'allongement et l'épaisseur de l'actionneur. Une application potentielle de l'actionneur optique en tant que commutateur sans fil et contrôlable à distance a été démontrée.

Dans le deuxième chapitre, nous avons démontré le mouvement autonome sans précédent d'une bande d'EVA déposée sur un substrat en acier isotherme. La bande est fabriquée à partir d'EVA pur réticulé contenant des cristallites alignés de manière uniaxiale. Une fois en contact avec le substrat chaud, un gradient de température est immédiatement établi sur toute l'épaisseur et élève la section médiane de la bande en arc, provoqué par la contraction induite par la fusion asymétrique. Dans l'air, une recristallisation dirigée se produit et dilate la bande pour retomber à la forme plate initiale. Dans cet état, le substrat chaud chauffe la bande pour qu'elle se plie à nouveau afin de répéter le cycle de mouvement précédent. Une boucle de rétroaction thermo-mécanique-thermique est ainsi facilement établie et validée pour commander le mouvement continu, qui peut durer une heure ou environ 1 000 cycles. Nous avons étudié les facteurs qui affectent l'amplitude et la période du mouvement autonome et avons constaté que la température du substrat et l'allongement de la bande sont des paramètres importants, tandis que la durabilité est principalement altérée par le contact de plus en plus étroit entre la bande et le substrat. Le potentiel de conversion de l'énergie thermique en énergie mécanique a été démontré par une fonction d'auto-marche et la capacité de promouvoir la rotation d'une roue. Dans le troisième chapitre, un photoactionneur à base de LCP contenant un colorant proche infrarouge (NIR) a été préparé

par photoréticulation d'une bande de LCP alignée de manière uniaxiale d'un côté en monodomaine et de l'autre en polydomaine LC relaxée. L'actionneur est multifonctionnel et remplit trois fonctions: le transport guidé par la lumière, la rotation flexible en locomotion et le mouvement autonome. Avec deux extrémités confinées sur un substrat et maintenues à plat, la bande peut générer une bosse sur le site de l'irradiation laser, résultant du réarrangement des chaînes polymères lors de la contraction iso-contrainte à l'état isotrope et du passage ultérieur à l'état LC. Une cargaison en forme de tige placée à côté de la bosse peut être transportée de bout en bout lorsque la bosse se propage sous balayage laser. Avec une extrémité fixée sur le substrat et l'autre libérée dans l'air, la bande soumise à une irradiation laser constante peut exécuter un mouvement auto-entretenu selon plusieurs modes, qui sont dictés par l'angle incident du laser. Le mouvement autonome est basé sur le mécanisme d'observation automatique et piloté par le retour photo-thermo-mécano-thermique. Numériser la bosse découpée de la bande de manière uniforme avec le laser peut faire en sorte que la bosse rampe directement sur les surfaces horizontales et inclinées, tandis qu'un balayage asymétrique peut guider le sens de rotation avec souplesse.

Mots clés : Actionneurs en polymère; Actionneurs optiques; Polymères semi-cristallins; Polymères cristallins liquides; Transition de phase ordre-désordre; Mouvement autonome; Actionneurs multifonctionnels

ABSTRACT

Polymer-based soft actuators capable of reversible actuation are attracting wide interest and attention as they can be constructed from a broad range of polymers and triggered by various types of stimuli to output physical work repeatedly. Among them, thermoresponsive and photoresponsive actuators based on semicrystalline polymers (SCPs) and liquid crystalline polymers (LCPs) are increasingly developed due to their potential applications as smart devices in numerous fields. In recent years, massive efforts have been devoted by researchers to developing new materials and functions based on SCPs and LCPs, but the demand for constructing robust polymer actuators with advanced functions using readily available materials and facile strategies has not been fulfilled. The main purpose of this thesis is to develop and study such advanced and functional polymer actuators controllable by thermal or light to output mechanical energy through reversible actuation, using commercially available semicrystalline poly(ethylene-co-vinyl acetate) (EVA) and a type of photocrosslinkable LCP with addition of small amounts of heat-generating additives. Our approaches are simple, convenient and robust as we only use a laser or an isothermal substrate to regulate several leading-edge reversible actuation behaviors. The use of EVA elicited two projects which are presented in Chapter 1 and Chapter 2, respectively, as the first part of this thesis. In this part, two reversible actuation behaviors were described. The first one is controlled by on/off switching of the laser, while the second one is self-sustained on an isothermal substrate surface. Both behaviors are associated with a temperature gradient established in the thickness direction of the actuator and driven by melting–crystallization phase transition. The second part of this thesis, presented in Chapter 3, deals with an LCP actuator. We show that a monolithic LCP strip crosslinked non-uniformly can perform as a multifunctional photoactuator driven by LC–isotropic phase transition.

In the first chapter, we prepared a type of gold nanoparticle-containing optical actuator based on a stretched EVA strip accommodating oriented crystallites. Upon irradiation with a laser (532 nm in wavelength), surface plasmon resonance (SPR) of gold nanoparticles (AuNPs) is activated to release heat that partially melts the crystallites at T_{light}. The

crystallites with their melting temperature (T_m) below T_{light} are melted as the actuation domain that bends the strip towards the laser direction as a result of uneven contraction forces along the thickness due to the temperature gradient, while the crystallites with T_m higher than T_{light} sustain as the framework. When the laser is removed, oriented recrystallization in the actuation domain induces expansion along the stretching direction to unbend the strip. Results show that T_{light}, the photomechanical force, the actuation magnitude and the actuation speed are tunable by adjusting the laser intensity, the content of AuNPs, the elongation and thickness of the actuator. A potential application of the optical actuator as a wireless and remotely controllable switch was demonstrated.

In the second chapter, we demonstrate an unprecedented autonomous motion of an EVA strip deposited on an isothermal steel substrate. The strip is made from crosslinked pure EVA containing uniaxially aligned crystallites. Once in contact with the hot substrate, a temperature gradient is immediately established across the thickness and elevates the middle section of the strip to form an arch, caused by the melting-induced-contraction of the bottom side of the strip. Once in the air, the melted EVA chains are cooled and recrystallize, which generates opposite extensional force on the bottom side and brings the strip to fall back to the initial flat shape. In this state, the hot substrate heats the strip to bend it again, and the arching up and flattening down motion cycle is repeated. A thermo-mechanical-thermal feedback loop is thus easily established to drive the self-sustained motion, which can last hour-long or around 1000 cycles. We investigated the factors that affect the amplitude and period of the autonomous motion and found that both the substrate temperature and elongation of the strip are important parameters, while the durability is mainly decayed by the looser and looser contact between the strip and the substrate. Potential of converting thermal energy to mechanical energy was demonstrated by a self-walking function and the ability to promote the rotation of a wheel.

In the third chapter, a multifunctional LCP-based photoactuator containing a near-infrared (NIR) dye is described. It was prepared by photocrosslinking a uniaxially aligned LCP strip on one side in monodomain and the other side in relaxed LC polydomain. The actuator has three functions, which are the light-guided transportation, flexible turning in locomotion and autonomous motion. First, with its two ends fixed on a substrate and kept flat, the strip

can generate a bump at the site of laser irradiation, arising from polymer chains rearrangement during isostrain contraction in isotropic state and subsequent transition to LC state. A rod-shape cargo put beside the bump can be conveyed from end to end as the bump propagates under laser scanning. Secondly, with one end fixed on the substrate and the other released in air, the strip under constant laser irradiation can execute self-sustained motion in multiple modes, which are dictated by the incident angle of the laser. The autonomous motion is based on a self-shadowing mechanism and driven by the photothermo-mechano-thermal feedback. Thirdly, scanning the bump cut from the strip uniformly, with the two ends free, laser scanning can make the actuator crawl straightly on both horizontal and inclined surfaces, while unsymmetrical laser scanning can guide the turning direction in its movement.

Keywords: Polymer actuators; Optical actuators; Semicrystalline polymers; Liquid crystalline polymers; Order-disorder phase transition; Autonomous motion; Multifunctional actuators

ACKNOWLEDGMENTS

In the first place, I would like to express my sincere and deep gratitude to my supervisor Prof. Yue Zhao for his guidance, encouragement and care during my pursuit of Ph.D degree at Université de Sherbrooke. His insight and rigorousness in academic research, profound understanding of knowledge, passion on science and patience during lecturing have benefited me significantly and will influence my whole life.

I would like to thank Prof. Claude Spino and Prof. Patrick Ayotte for being member of my doctoral supervisory committee and serving in the jury of thesis. I would like to thank Prof. Armand Soldera and Prof. Suzanne Giasson (Université de Montréal) for being internal and external experts, respectively, in my thesis jury. I would like to thank all the professors and staff working in the Department of Chemistry, Université de Sherbrooke, for their support and kind help. I would also like to thank Dr. Daniel Fortin for conducting XRD measurements. I acknowledge Dr. Franck Camerel (Univ. Rennes) for the collaboration.

I acknowledge all our group members, colleagues and friends for their help and discussion during my study: Mrs. Xia Tong, Dr. Jun Xiang, Dr. Xili Lu, Dr. Rong Yang, Dr. Weizheng Fan, Dr. Hui Xiao, Dr. Hu Zhang, Dr. Bing Yu, Dr. Xin Zhao, Dr. Shengwei Guo, Dr. Liangliang Dong, Dr. Shangyi Fu, Dr. Li Han, Dr. Guo Li, Mr. Farhad Farnia, Ms. Amélie Auge, Mr. Damien Habault, Mr. Richardo Da Silva Lemos, Mr. Lu Yin, Mr. Yinming Chen, Mr. Zhichao Jiang, Mrs. Yaoyu Xiao, Ms. Jie Jiang, Ms. Chaza AI Akoumy, Ms. Nina Ravandi, Mr. Congcong Yin and Mr. Zhuo Li.

I acknowledge Le Fonds de recherche du Québec: Nature et technologies (FRQNT) and Chinese Scholarship Council (CSC) for awarding me a doctoral scholarship. I also thank the Education Office of the Consulate General of China in Montreal for their service.

I would like to express my sincere gratitude to my parents, my older sisters, my eldest brother and other family members for their consistent love, support and comfort.

Finally, I acknowledge the Natural Sciences and Engineering Research Council of Canada (NSERC), FRQNT and Université de Sherbrooke for financial support.

TABLE OF CONTENTS

LIST OF SCHEMES

CHAPTER 3

CHAPTER 4

LIST OF FIGURES

INTRODUCTION

CHAPTER 1

CHAPTER 2

LIST OF TABLES

INTRODUCTION

Actuators are controllable devices that produce work (1). Upon receiving the control signal, actuators draw energy from the power sources to shift in shape, perform motion, or move an object. As a result, actuators play a significant role as active components in machines, robots and many other systems. Interest in replacing traditional rigid metal actuators with polymers has risen because polymers are cost-effective, soft, light in weight, easily processable, more biocompatible, widely available for applications in different surroundings and environments, and produce less noise. Stimuli-responsive polymers (SRPs) are the dominant materials for polymer actuators as many sorts of stimuli are available for triggering actuations in various situations (2), for example, thermoresponsive polymers for implants (3), electroactive polymers (EAPs) for artificial muscles and electronics (4), pH-responsive polymers for drug delivery (5), water- and/or humidity-responsive polymers for wet environment (6, 7), chemical-responsive polymers for pollutant detection (8, 9), magnetic field-responsive polymers for non-contact manipulation (10, 11), and light-responsive polymers for wireless, remote and non-polluting actuation (12, 13). Currently the definition of actuation is very broad and polymer actuators can refer to both irreversible and reversible ones (14, 15). An irreversible system here means that the material or device is switchable to a different shape or state upon applying a stimulus, after removal of which the shape or state is maintained and does not respond to the subsequent triggering. A reversible system, in contrast, implies that the polymer actuator can switch regularly at least between two states upon on/off switching of the external stimulus or undergo continuous motion under constant stimulation. Irreversible polymer actuators can work only once, after which the actuation function is lost unless a reprogramming process is applied. Advantageously, reversible actuators can be used repeatedly with little or no fatigue of the function for many cycles. Roughly speaking, depending on the mode of reversible actuation, reversible actuators encompass three categories. The first class refers to those that are activated upon stimulation and recovered as the stimulus is removed. These actuators comprise the majority of reversible actuators. The second type are bistable, which means that the state or shape of the actuator upon activation can be maintained for at least some time even after the stimulus is removed. The original state or shape can be recovered spontaneously as time goes on or rapidly when another stimulation is applied. The third type of reversible actuators is capable

of continuous motion under constant stimulation. The motion is autonomous and self-sustained with no need of external intervention. Obviously, polymer actuators with reversible actuation behaviors are more robust and attractive in terms of advanced properties, durability and application field. This thesis concentrates on reversible soft polymer actuators with emphasis on heating or photothermal heating induced actuation. In section 1 of this introduction chapter, the stimuli, materials and actuation mechanisms are briefly introduced.

Among the considerable amount of SRPs, semicrystalline polymers (SCPs) and liquid crystalline polymers (LCPs) are distinguished candidates for polymer actuators due to their intrinsic capability of reversible order-disorder phase transitions. SCPs with two melting peaks or a broad melting range are developed as reversible shape memory polymers (RSMPs) based on the mechanism of melting-induced-contraction (MIC) and crystallization-induced-elongation (CIE). In the first work of this thesis, an optical actuator working as a switch was prepared and studied based on the above mechanism combined with a photothermal temperature gradient. Gold nanoparticles were modified and incorporated as photothermal agent for light absorption control. In the second work, a facile design based on pristine crosslinked SCPs and a new concept and mechanism for 'thermo-mechano-thermal' feedback loop were put forward, which enabled autonomous motion as a new function of the polymer actuators. Polymer actuators and materials relying on SCPs are reviewed in section I.2. On another front, LCPs are well-known smart polymeric materials and have attracted massive attention owing to the many orientation states of mesogens as well as the ease of polymer processing. When the order-disorder phase transition of mesogens is coupled to the polymer network structure, diverse macroscopic shape changes under external stimulation can occur. In the third work, a dye-doped photoactuator based on LCPs was developed with integration of light-guided multifunctionality. LCPs are introduced and summarized, with emphasis on the structured actuation and advanced functions, in section I.3. Both SCPs and LCPs depend on order-disorder phase transition at play to achieve reversible actuation and they are mainly triggered by thermal or light energy. In the whole introduction chapter, thermoresponsive and photoresponsive polymer actuators will be emphasized. A presentation of the objective of this thesis is given in the end.

I.1 Introduction to Soft Polymer Actuators

Polymer actuators essentially play the role of energy conversion, converting the energy drawn from the environment or an external energy source to mechanical energy. Soft polymer actuators are prepared mainly using smart soft polymeric materials which can transform molecular level movement into macroscopic shape changes or mechanical motions under external stimulation. The actuation is manifested as reversible, fast and directional with large amplitude of deformation (14). Stimuli provide polymer actuators with external control and necessary power sources. Various stimuli, either chemical or physical as listed in Figure 1, can be used to trigger the shape change of polymer materials between two shapes reversibly, and this reversible actuation has long been a pursuit by many researchers for applications in different situations. A plethora of stimuli-responsive polymer materials have been developed as the building blocks of reversible polymer actuators controllable by pneumatic actuation, direct or indirect heating, humidity or chemicals intervention, magnetic or electric field stimulation and light illumination.

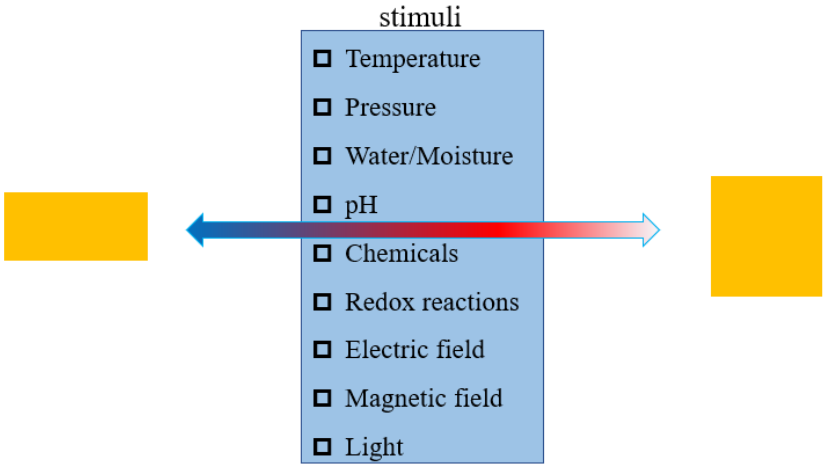

Figure 1. Reversible actuation for polymeric materials under different external stimuli.

Pressure can provide very large actuation stress to reversibly inflate elastomers. When the extensible elastomers are bonded with inextensible materials, the strain difference during pneumatic actuation can induce bending, which is valuable in the design of adaptive motion of soft robots (16). Water as a stimulus is most frequently applied in hydrogels where water

absorption/desorption drives the reversible volume swelling/shrinking (17). Moisture diffusion manipulates the actuation of hygroscopic polymer materials and allows application in humid environments instead of immersion in water (6, 18). The change in pH value can also induce swelling/shrinking actuation of polyelectrolyte hydrogel in solution by altering the ionic interaction, leading to reversible twisting and untwisting (19). Other chemicals including some organic solvents, vapors and ions can cause change in molecular order or non-uniform expansion, bringing in reversible bending/unbending and curling/uncurling properties (20, 21). Redox reactions that involve oxidation and reduction of metal ions are usually employed in hydrogels to induce reversible swelling/shrinking or autonomous motion of the hydrogel. The association/dissociation of the grafted complex moieties governed by the metal oxidation state change the crosslinking density that determines the swelling degree (22). The oscillating Belousov-Zhabotinsky (B-Z) redox reaction, on the other hand, can periodically switch the oxidation states of the grafted catalyst, leading to periodical change in lower critical solution temperature (LCST) of the polymer and, consequently, oscillating swelling/shrinking of the gel at constant temperature, driving autonomous self-walking of the hydrogel with designed gradient structure (23). Electric field is a widely used stimulus under which electroactive polymer actuators (EAPs) are operated (24), including ionic EAPs driven by ions diffusion, conducting conjugated polymers actuated by electrochemical redox reactions and non-ionic dielectric elastomers driven by electrostatic forces (4). Simultaneously, joule heating effect is also getting much attention (25, 26). Temperature is the most common and readily available physical stimulus, and numerous SRPs are thermally responsive. The change in temperature can induce asymmetric expansion/shrinkage in layered materials, swelling/shrinking in temperature-responsive hydrogels, melting/crystallization in SCPs and liquid crystal–isotropic phase transition in LCPs, all of which can make reversible actuation occur. In cases where direct heating is unrealistic, it may be substituted by indirect heating such as electrothermal heating, alternating magnetic field-induced heating and photothermal heating, provided that conducting wires or nanofillers, magnetocaloric agents and photothermal agents are respectively incorporated in the polymer actuators. Compared to pressure provided by external pumping systems tethered with tubes and electric circuits that need wires connected to the actuator, magnetic and light fields are ideal for wireless control. Magnetic particles can be embedded for

non-contact manipulation independent of heating effect in small-scale robot (27, 28), while photochemical effect is usually utilized in photoisomerisable polymer actuators at room temperature (RT) (29).

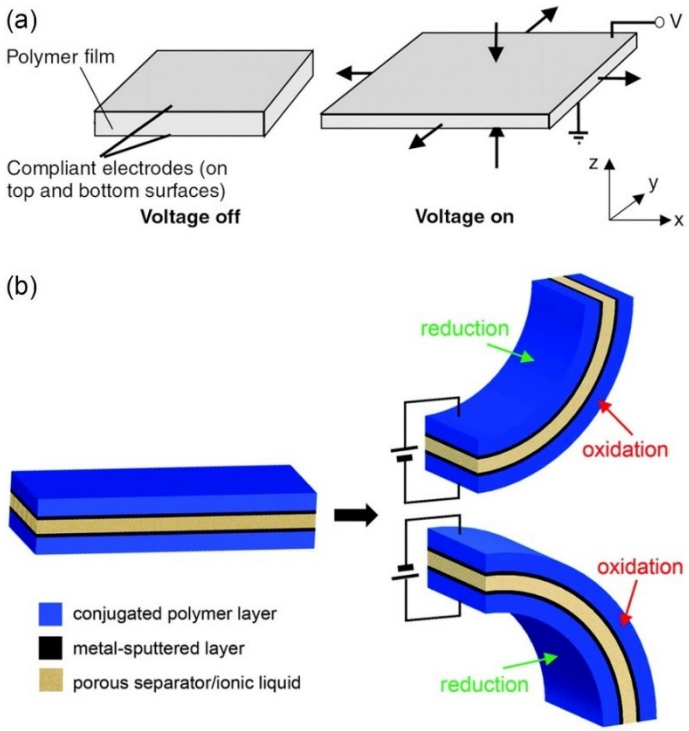

Figure 2. Schematic illustration of the electrical actuation of dielectric elastomers (a) and conducting conjugated polymers (b). In (b), metal sputtering at the polymer and separator interfaces is conducted to increase charge transfer; the ionic liquid is loaded in a porous membrane to increase ionic conductivity. Figure 2a is reproduced with permission from [30]. Copyright 2000, the American Association for the Advancement of Science. Figure 2b is reproduced with permission from [31]. Copyright 2018, the Royal Society of Chemistry.

From the standpoint of materials, soft polymer actuators are mainly constructed from dielectric elastomers, conducting polymers, hydrogels, bilayer structures, SCPs and LCPs (32). To enable reversible deformation for actuation, SCPs and LCPs generally require a specific processing or programming process, i.e. the procedure performed to store energy or establish molecular level order. Upon stimulation, the stored energy is released through order-disorder phase transition, causing macroscopic movement of a portion or the whole of the actuator. For some other materials,

the distribution of heterogenesis such as a gradient crosslinking density, an active/inactive bilayer structure or anisotropic porosity into the material is usually required. Under stimulation, the asymmetric changes in strain and stress in the material arise from the heterogeneous structure and lead to non-uniform deformations. As the external stimulus is removed, the original shape or position of polymer actuators should be recovered. This reversible shape change or motion can be used to do physical work. Exemples of materials and actuation mechanisms related to reversible volume change will be described in the following section, with an emphasis on direct heating or photothermal heating induced reversible actuation, while polymer actuators based on SCPs and LCPs driven by order-disorder phase transitions will be introduced in detail in later sections.

Dielectric elastomer actuators (DEAs) are polymer actuators which transform electrical energy into dramatic change in size, mimicking true-muscle like actuation (33-35). The elastomer is prestrained and sandwiched by two compliant electrodes, as illustrated in Figure 2a, which are oppositely charged under electric field excitation; the elastomer is compressed by the electrostatic force normal to the film surface, leading to large expansion in plane and contraction in thickness. Silicone, polyurethane and acrylic elastomers are outstanding materials due to their fast speed of dimension changing, large actuation stress and strain, and high energy density, although the driving voltage in kilovolts level is much too high due to large dielectric constants (36, 37). Bottlebrush elastomers and thermoplastic elastomers are emerging as new DEAs that require lower electric field (38, 39). In contrast to DEAs, conjugated polymers actuators (CPAs) are conducting and merely need several volts to drive the actuation. Conjugated polymers such as polypyrrole, polyaniline and polythiophene are modified by dopants to introduce charge centers through oxidation or reduction (4, 31, 33, 40). During electrochemical redox cycling, the uptake and migration of counterions between the polymer chains and the solvent induce swelling and shrinking of the conjugated polymer electrode, causing bending and reverse bending deformations as shown in Figure 2b. For EPAs, wires are needed for electricity supply and the liquid electrolyte has to be encapsulated for use in air, both of which are constraints for wide applications of EPAs.

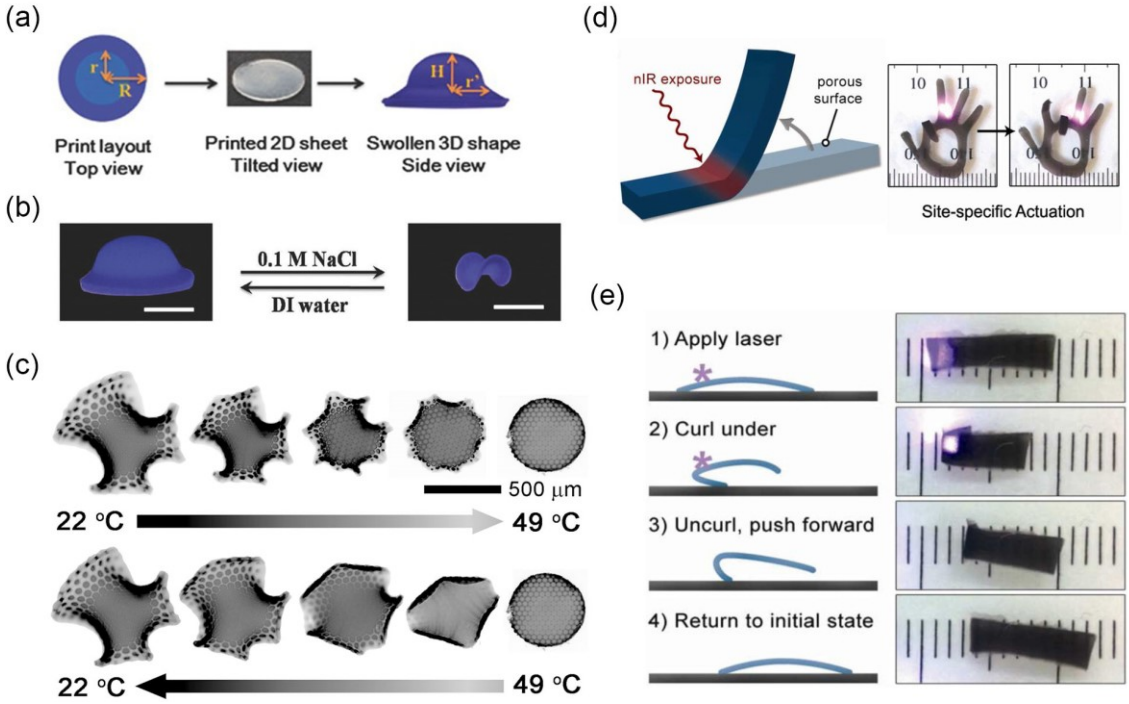

Figure 3. Shape morphing, bending and locomotion of hydrogel actuators. (a) A hydrogel printed with gradient crosslinking density, with the core in light blue slightly crosslinked and the ring in deep blue densely crosslinked. (b) Reversible shape changing of the hydrogel in water and NaCl solution. (c) Reversible shape morphing of a hydrogel based on PNIPAM copolymers containing benzophenone units during heating and cooling. (d) Schematic (left) and pictures (right) showing the NIR-induced bending of the polypeptide/graphene composite hydrogel. (e) NIR light-guided crawling of the hydrogel at ambient temperature and in air. Figures 3a and 3b are reproduced with permission from [41]. Copyright 2016, Wiley-VCH. Figure 3c is reproduced with permission from [42]. Copyright 2012, the American Association for the Advancement of Science. Figures 3d and 3e are reproduced with permission from [43]. Copyright 2013, American Chemical Society.

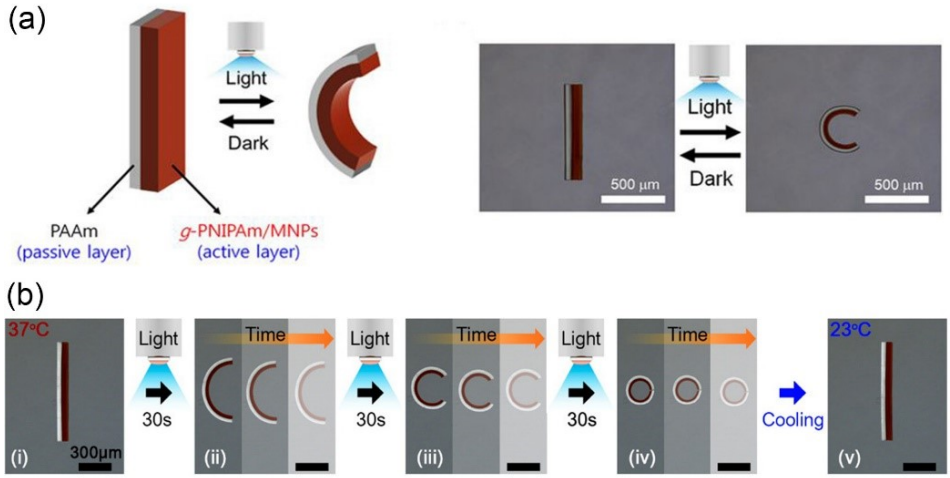

Figure 4. Schematics and images showing the light-controlled actuation of a hydrogel bilayer actuator. (a) Bending/unbending with no hysteresis. Reproduced from [44] under the terms and conditions of the Creative Commons Attribution 4.0 International License. (b) Bistable actuation with thermal hysteresis. Reproduced with permission from [45]. Copyright 2016, American Chemical Society.

Hydrogel actuators (HAs), which are based on crosslinked polymers sensitive in volume change to water absorption/desorption, contribute to a considerable amount of polymer actuators (46). The non-uniform swelling/shrinking arising from a gradient in crosslinking density render reversible complex 3D shape morphing (41, 42), which can be seen in Figure 3a and 3b. Hydrogels based on poly(N-isopropylacrylamide) (PNIPAM) materials are most popular for preparation of thermo- and/or photoresponsive HAs since PNIPAM bears an LCST, above which the hydrogels shrink and below which swelling happens. A thermoresponsive hydrogel based on PNIPAM copolymer containing benzophenone units, prepared through photo-patterning crosslinking that induced radial gradient crosslinking density, can transform between a 2D flat state to complicated 3D shapes during heating and cooling, respectively, as shown in Figure 3c. The discrepant structure distributions in the hydrogel resulted in inhomogeneous swelling and shrinking. It is also possible to actuate HAs at RT in the air with near-infrared (NIR) light. An example is a polypeptide/graphene composite hydrogel whose surface layer was embedded with anisotropic porosity. When exposed/unexposed to NIR light, vapor water molecules diffused into/out from the

upper porous layer rapidly under photothermal effect, causing fast bending/unbending which was transformed to selective-actuation and light-guided crawling (43), as seen in Figure 3d and 3e. Assembling hydrogels with different swelling degrees forms hydrogel bilayers, with a passive hydrogel layer comprising of polyacrylic acid (PAA) or polyacrylamide (PAAm) that does not respond to temperature change. As shown in Figure 4a, when laminated with PNIPAM, the formed bilayers bent to the active layer side due to the mismatch in shrinking upon rising the temperature above LCST through heating or photothermal heating, and subsequently recovered to the initial flat state when the temperature fell below LCST (44, 47). By grafting PNIPAM to methylcellulose (MC) and laminating the grafted PNIPAM-g-MC layer with PAAm with presence of magnetite as photothermal agent, the hydrogel bilayer was endowed with a large thermal hysteresis, which allowed bistable shape change of the actuator by light (45). Figure 4b shows that the bilayer remained in bent state after removal of light illunation and recovered to the initial flat state once cooled down below LCST. Ascribing to hydrogels' good biocompatibility, compliance and responsiveness to water, chemicals, pH scale, temperature and light, HAs have great potential in biomedical applications as drug delivery systems as well as in biomimetic robotic devices (47-50), although the response speed should be further enhanced.

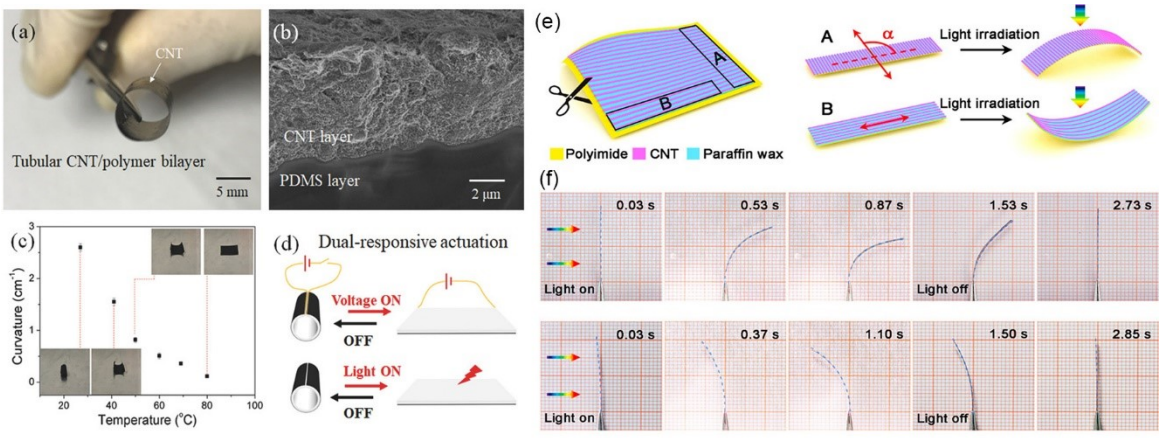

Figure 5. Bilayer actuators based on materials of different CTE and the actuation. (a) Picture of the rolled PDMS/CNT bilayer actuator. (b) Scanning electron microscopy image showing the cross-section of the bilayer. (c) Curvature change of the tubular bilayer with temperature. The insets are images of the bilayer at corresponding temperatures. (d) Schematic diagram showing the

reversible actuation of the bilayer by on/off control of electricity and light. (e) Schematic demonstration of the alignment of CNT in PI matrix and the relationship between the cutting angle α and the bending direction of the PI/CNT-wax bilayer strip. (d) Images showing the bending direction of Strip A (upper panel) and Strip B (lower panel) upon visible light illumination. Figures 5a–5d are reproduced with permission from [51]. Copyright 2017, Wiley-VCH. Figures 5e and 5f are reproduced with permission from [52]. Copyright 2016, American Chemical Society.

Bilayer structured actuators based on asymmetric expansion/contraction controllable by direct or indirect heating comprise a large portion of polymer actuators. Based on a sharp difference in coefficient of thermal expansion (CTE), many polymers such as PDMS, polyimide (PI), polycarbonate (PC) and polyvinylidene fluoride (PVDF) can be laminated with a light absorber material like carbon nanotubes (CNT) and reduced graphene oxide (rGO) to form an electroactive or photo-responsive bilayer photoactuator (51-54), as CNT and rGO have not only very low CTE but also good electrothermal and photothermal property. The PDMS/CNT-rGO bilayers are easily made as a rolled bimorph with CNT-rGO layer toward outside (55). During curing of the PDMS layer on top of the CNT-rGO layer at 100 ^{o}C, the PDMS layer with a much higher CTE was highly expanded but remained flat due to constraint of the substrate; when cooled to low temperature and peeled off from the substrate, the bilayer contracted to a much greater extent than the CNT-rGO layer, forming a rolled shape. NIR illumination on the roll increased the temperature rapidly and expanded it to flat shape within seconds. Upon removal of light illumination, the roll was recovered with a slower rate. Another PDMS/CNT bilayer prepared by a similar method has been shown to respond to temperature, light and electricity (Figure 5a-d) (51). The rolling/unrolling actuation can be well controlled by either photothermal or electrothermal effects. The rolled tubular bilayer with two ends blocked can even jump against the substrate and be launched into the air upon light illumination through releasing the elastic energy. These bilayer actuators are promising for application as smart windows and adaptive robots that can crawl over simple obstacles and even jump. Polyimide (PI) also has low CTE and has been used to laminate with CNT-dispersed wax, forming a PI/CNT-paraffin wax bilayer with very high sensitivity to photothermal effect, performing rapid bending/unbending upon exposure/removal of light illumination (52). The CNT were highly oriented and wrapped by the wax which has higher CTE than PI. As the aligned CNT

sheets were anisotropic material confining the wax expansion anisotropically during photothermal heating, expansion force perpendicular to the longitudinal direction of CNT was produced; contractile force was generated along the CNT orientation direction due to the non-uniform expansion from the middle to the edges of the strip. By manipulating the orientation direction of the aligned CNT layer with respect to the strip long axis at an angle (α) of 90° (perpendicular), apheliotropic bending (away from the light source) was observed (Strip A in Fgiures 5e and 5f) because the expansion force perpendicular to the alignment of CNT was predominant; oppositely, the contraction force along the long axis was dominant and phototropic bending (toward the light source) was observed with α of 0°, as shown by strip B in Figures 5e and 5f. Strip B was preshaped helical to enable untwisting and twisting upon light exposure and removal, respectively, and attached with a claw made of six strip A specimens to assemble a telescopic arm. The arm can conduct grabbing/releasing and elongation/contraction actions under visible light manipulation. By filtration of a solution of single-walled CNT (SWCNT) on a PC membrane, as shown in Figures 6a and 6b, a PC/SWCNT bilayer photoactuator capable of light-controlled bending/unbending has been reported (54). As the CTE of PC is 10 times larger than SWCNT, the bilayer was readily bent toward the SWCNT layer within seconds to a maximum bending angle of 90° upon light irradiation and recovered rapidly in a similar speed when the light was off. More interestingly, increasing the light intensity at the saturated bending angle led to oscillating movement of the bilayer film under constant light irradiation, due to the self-shadowing effect. When the film was rolled into a tubular shape with the SWCNT layer facing outside and irradiated by light from one side (Figure 6c), it could move away from the light source continuously. The light-driven autonomous motion including oscillating and continuous rolling are valuable advanced functions for consistent conversion of light energy to mechanical energy.

Bilayers combine materials and properties of discrepancy to form actuators with novel functions. With a broad source of polymers, more bilayer actuators with high performances can be expected for application in different fields. The delamination between layers at the interface, however, is a disadvantage of bilayer materials. Chemical modifications at the interface alleviate this problem, but it usually requires additional design and use of the chemistry (56-58). Single-material or

monolithic actuators based on SCPs and LCPs overcomes the delamination problem and even allows design of more complicated structures and functions by virtue of programming.

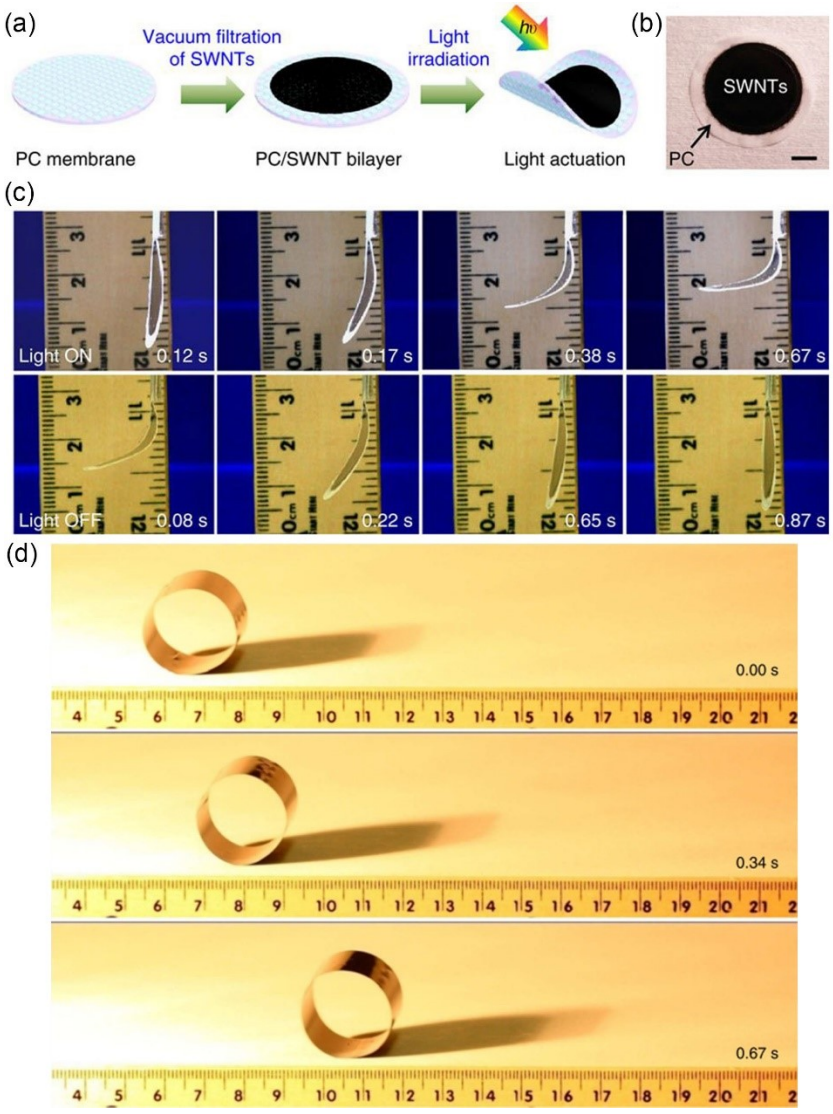

Figure 6. PC/SWCNT bilayer photoactuators. (a) Schematic illustration of the preparation and actuation of the bilayer structure. (b) Optical image of a circular bilayer prepared by vacuum filtration (scale bar, 5 mm). (c) Optical image showing the bending (first row) and unbending (second row) of the bilayer illuminated by 100 mW cm^{-2} white light from the left at light on and off states, correspondingly. (d) Optical images showing the forward-rolling of the bilayer motor

with time under illumination of a halogen lamp from the left side. Reproduced with permission from [54]. Copyright 2014, Springer Nature.

I.2 Actuators Based on Semicrystalline Polymers

Semicrystalline polymers (SCPs) are crystallizable polymers with varied degree of crystallinity, which usually differs from one to another and remains much lower than that of small molecule crystals because the long polymer chains make the packing and crystal growth rather slow and incomplete. Upon heating to a temperature T_{reset} (or T_{prog}) above the melting temperature T_m, the crystallites in SCPs are transformed from the crystalline state to the melted amorphous state; when cooled from the melt, crystallization occurs at crystallization temperature T_c and crystallites form. This reversible thermal phase transition endows many SCPs with shape memory effect (SME) after a pretreatment procedure called programming (3, 59). Crosslinking of the polymer is generally necessary in order to inhibit plastic flow during deformation. Typically, a covalently crosslinked sample in its permanent shape is deformed above T_m under stress to a temporary state with certain strain, and then cooled under the stress to a temperature T_{low} below T_m for shape fixation through polymer chain crystallization. Heating the sample again to T_{reset} induces contraction and recovers the initial shape due to entropy elasticity of the polymer network. The entropy elasticity indicates that the deformation and force generated in the material is caused by its conformational changes. Nevertheless, subsequent cooling can not bring the sample back to the deformed temporary shape unless another programming process is applied. This is also true for amorphous polymers with glass transition as the phase transition. Therefore, the shape recovery from conventional SME is irreversible or one-way change since the deformed shape can not be reversed spontaneously by cooling. Interestingly, a few SCPs, however, have been found to possess two-way or reversible SME (rSME) allowing reversible shape changes or actuation in response to temperature change. These are reversible shape memory polymers (rSMPs) (60), which have received much attention as potential candidates for soft polymer actuators. Highly oriented fibers spun from polyethylene (PE) and crosslinked in crystalline state by γ-radiation was first revealed to manifest a reversible strain of 25% during melting/crystallization cycling, as shown in Figure 7, without applying any external stress (61). The original shape was obtained by

heating the crosslinked fiber above T_m first, followed by cooling to RT. Subsequent heating and cooling induced interconvertible contraction and expansion, making PE fiber a promising material for polymer actuators. However, the ultra high degree of orientation originating from the spinning process, the difficulty in crosslinking PE in highly oriented state and the fibrous structure hindered the further development and application of PE fibers as actuators.

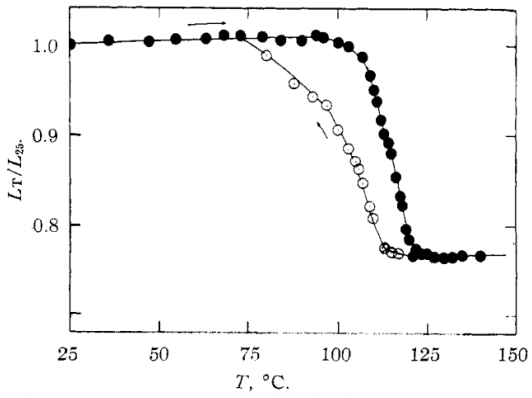

Figure 7. Plot of the length ratio of PE fiber crosslinked by γ-radiation as a function of temperature. L_T and L_{25} are the length at temperature T and RT, respectively. Black dot: on heating; white dot: on cooling. Reproduced with permission from [61]. Copyright 1959, American Chemical Society.

Later, reversible actuation under constant external stress was first realized using the crosslinked semicrystalline material with relatively broad melting transition (62, 63). Briefly, the poly(cyclooctene) (PCO) sample was first heated to T_{reset}, then deformed to shape C by applying a constant stress which oriented the melted polymer chains along the loading axis, followed by cooling to T_{low} under the stress. During cooling, the oriented chains recrystallized and rearranged to favoring formation of extended-chain crystallites, in the loading direction. As a result, crystallization-induced-elongation (CIE) of the sample was induced and resulted in a temporary shape B, while heating to T_{reset} led to recovery of shape C accompanied by melting-induced-contraction (MIC). Under constant external stress, the sample was reversibly transformed between shape C and shape B during heating/cooling cycles, giving rise to a polymer actuator with restricted actuation (63). The actuation temperature of the PCO-based SCPs was further decreased to around RT by incorporating co-monomer and adjusting the composition and crosslinking density (64).

The key condition to the reversible actuation of these SCPs is the directed crystallization induced by the applied stress during cooling, without which the expansion is unable to occur. This condition was further validated in other semicrystalline polymers including polyurethanes and poly(ester urethane) with poly(1,4-butylene adipate) as the crystallizable segments (65, 66). Xie and coworkers achieved similar actuation under stress with the commercially available random copolymer poly(ethylene-co-vinyl acetate) (EVA), a semicrystalline elastomer with a broad T_m range (67), which is attributed to the different crystallite sizes corresponding to different lengths of polyethylene chain segments.

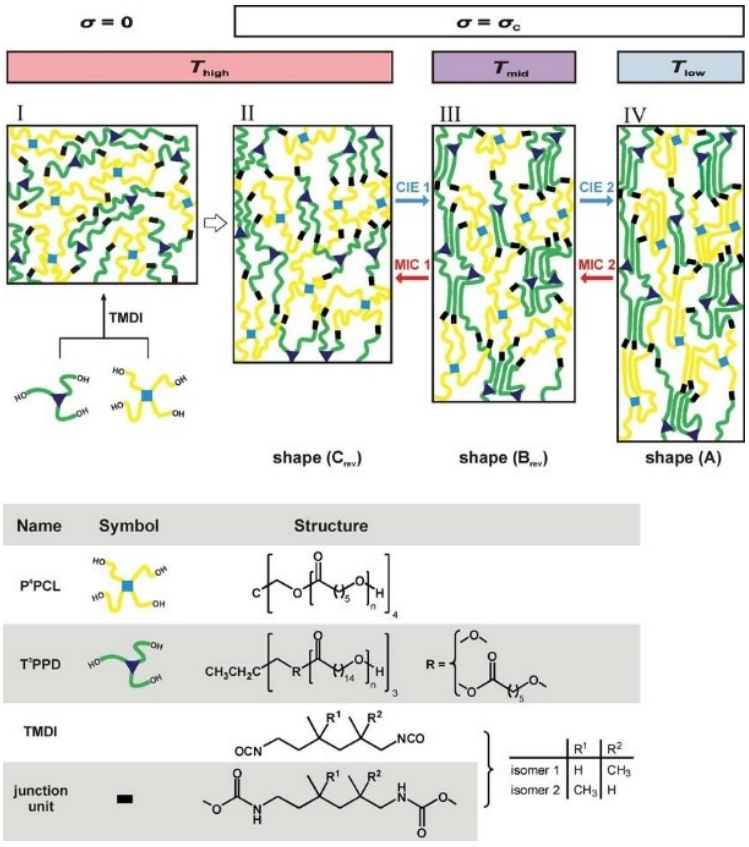

Figure 8. Precursors, PCL-PPDL polymer networks and the mechanism of rSME. I, synthesis of PCL-PPDL network; II, Shape C_{rev} at T_{high} under constant external stress σ_c; III, Shape B_{rev} at T_{mid} after crystallization-induced-elongation (CIE) from PPDL segments; IV, Shape A at T_{mid} after CIE from PCL segments. Reproduced with permission from [62]. Copyright 2010, Wiley-VCH.

Lendlein and coworkers further explored and developed the reversible triple shape memory effect (rTSME) with their synthesized multiblock copolyester urethanes under constant stress (62). The copolymer, poly(ε-caprolactone-co-ω-pentadecalactone) (abbreviated as PCL-PPDL), has two melting transitions $T_{m,\,PCL}$ and $T_{m,\,PPDL}$ ($T_{m,\,PCL} < T_{m,\,PPDL}$) and two crystallization transitions $T_{c,\,PCL}$ and $T_{c,\,PPDL}$ ($T_{c,\,PCL} < T_{c,\,PPDL}$) attributed to the crystallizable PCL segments and PPDL segments, respectively. Specially, on cooling the sample which was previously deformed at T_{reset} (forming shape C_{rev}) to an intermediate temperature T_{mid} that was between T_{low} and $T_{c,\,PPDL}$, PPDL segments crystallized first forming larger crystallites and the CIE led to the first temporary shape B_{rev} shown in Figure 8. Further cooling to T_{low} elongated the sample further to shape A due to CIE from PCL segments that crystallized at a lower $T_{c,\,PCL}$. By heating shape A from T_{low} to T_{mid} and to T_{reset} consecutively, shape changes toward shape B_{rev} and shape C_{rev} were observed successively while cooling from shape C_{rev} reversed the shape change order. This rTSME was still subject to the prerequisite of applying a constant external stress.

Although reversible actuation under stress could reach higher than 100 % in strain change and allows lifting objects up and down (63), the method is rather inconvenient and poses large constraints for application as polymer actuators. However, by optimizing the composition of the PCL-PPDL copolymers, Lendlein and coworkers successfully achieved free-standing rSME for the sample with PCL mass content of 75% (68). More clearly in this later work, the crystallites comprising PPDL segments with higher $T_{m,\,PPDL}$ were regarded as the skeleton domain (red domain in Figure 9a) like a physical network that dictated the programmed shape, while the actuation domain (green domain in Figure 9a) comprising PCL crystallites with lower $T_{m,\,PCL}$ governed the MIC during heating and CIE during cooling. During programming, the deformation at T_{reset} oriented both PCL and PPDL polymer chains in the macroscopic strain direction; on cooling to T_{low}, the skeleton domain and the actuation domain were formed from probably extended-chain crystallization along the deforming direction. When heated to T_{mid} (or T_{high}) between $T_{m,\,PCL}$ and $T_{m,\,PPDL}$, the sample in shape B contracted to shape A due to MIC of the actuation domain and extended back upon cooling to T_{low} in the deforming direction due to CIE of the actuation domain. Figure 9b shows that a helical shape B, deformed at T_{reset} = 100 ºC and fixed at 0 ºC, could be reversibly shifted to/from a bow shape A by heating and cooling, and the shape could also be

reprogrammed into different shapes while maintaining the reversible shape shifting ability. The rSME found in the PCL-PPDL copolymers is promising for application as thermal responsive soft grippers or fixators (68).

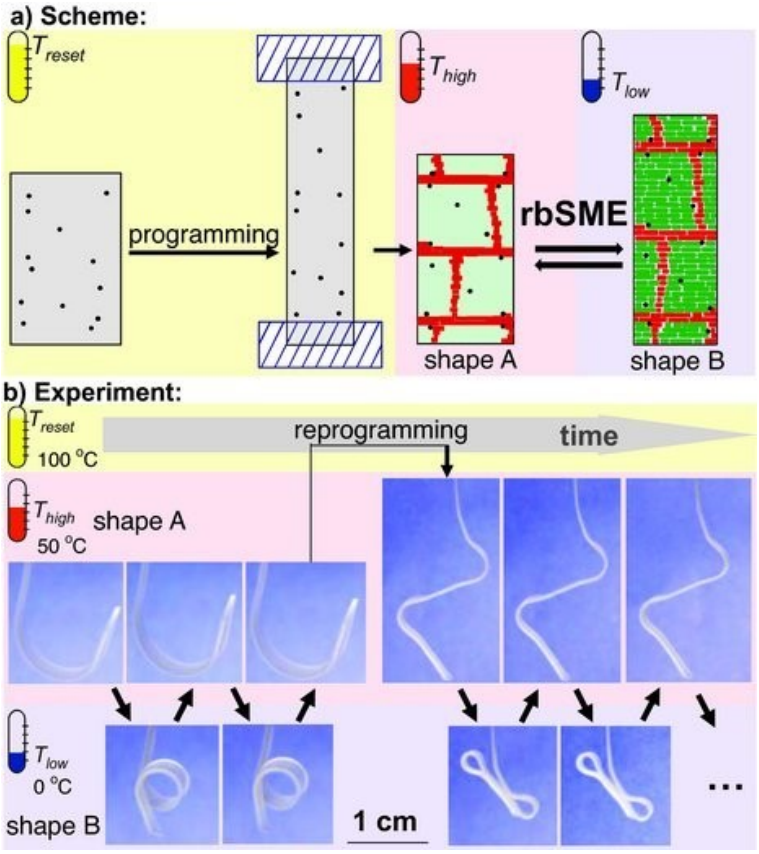

Figure 9. Reversible shape memory effect for PCL-PPDL copolymer networks. a) The sample is deformed at T_{reset} and cooled to T_{low} to form the skeleton domain (red) and the actuation domain (green). The reversible actuation is triggered by melting and crystallization of the oriented actuation domain. Black dots represent crosslinks. b) Photographs illustrating the rSME of a PCL-PPDL copolymer ribbon (40 mm × 4 mm × 0.4 mm). The bowed shape A was obtained by deforming the ribbon at T_{reset} into a helix shape which was fixed at T_{low}, followed by heating to T_{high}. The rSME was manifested as the shape shift between the bowed shape A at T_{high} and the helix shape B at T_{low}. The ribbon was reprogrammed at T_{reset} into a new shape A (open), which could shift to a new shape B reversibly. Reproduced with permission from [68]. Copyright 2013, Wiley-VCH.

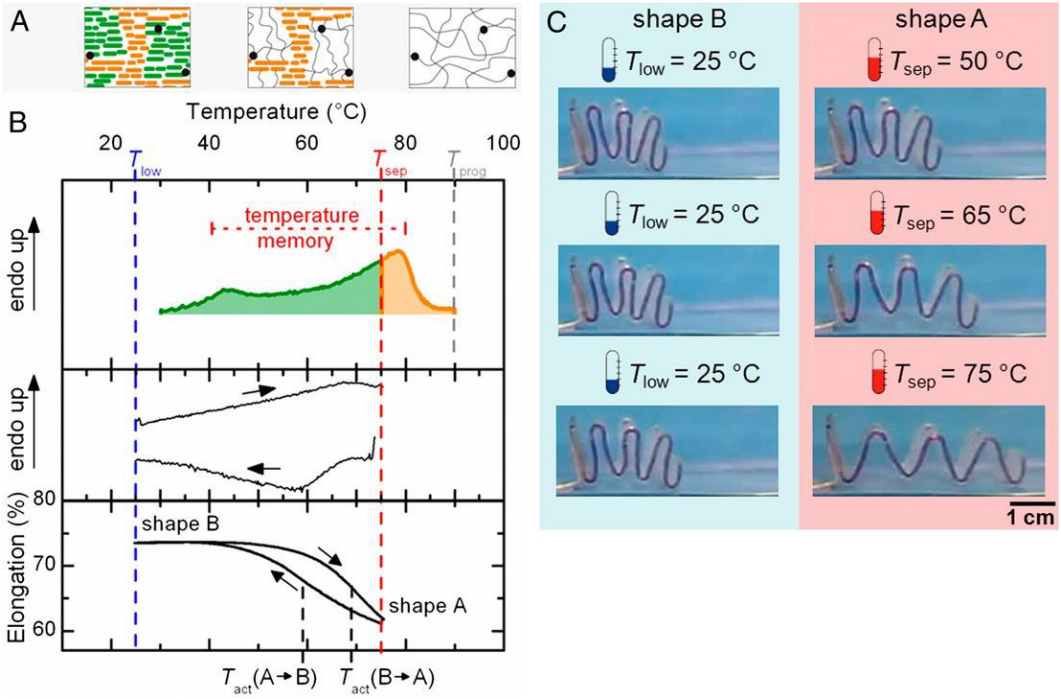

Figure 10. Temperature-memory polymer actuator and its working principle [69]. (A) The sample is programmed by first deforming in melted state at T_{prog} (right), followed by cooling to T_{low} for crystallization and shape fixation (left). On heating to T_{sep}, the sample contracts as the actuation domain (green) is melted while the skeleton domain (orange) is maintained (middle). Reversible actuation is realized between T_{low} and T_{sep} by melting and directed crystallization of the actuation domain in the polymer. The black dots represent crosslinking points. (B) Top: Thermogram showing that the crystallizable domains are divided by T_{sep} into skeleton domain and actuation domain. Middle: Thermogram of the first actuation cycle between T_{low} and T_{sep}. Bottom: Elongation with temperature for the sample programmed at T_{prog} = 90 °C, strain ε = 150 % and actuated for the first reversible cycle at T_{sep} = 75 °C, T_{low} = 25 °C. Shape A is obtained at T_{sep} with ε_A, and shape B is obtained at T_{low} with ε_B. (C) Photos showing the temperature-memory actuation of an EVA ribbon folded at T_{prog} = 90 °C, cooled to T_{low} = 25 °C and heated to varied T_{sep}. The concertina shape is reversibly switched between an expanded shape A and a contracted shape B. Reproduced from [69].

The broad T_m range of SCPs renders not only rSME, but also temperature-memory effect (TME) that remembers the temperature of actuation (T_{act}) (69, 70), making polymer actuators more intelligent. EVA polymers are the dominant materials as they own a very broad range of T_m spanning from near RT to 90 °C. The rSME of EVA copolymer networks is analogous to that of PCL-PPDL networks but the tunability of T_{act} of EVA deriving from the broadness of T_m proves to be a great advantage. Figure 10 presents the working principle of temperature-memory polymer actuators (TMPAs) (69). An intermediate temperature T_{sep} is introduced to divide the T_m range of EVA into two domains, as shown in Figure 10. The region with T_m between T_{sep} and T_{prog} (orange) is regarded as the skeleton domain, and the rest domain (green) with T_m between T_{low} and T_{sep} is designated as the actuation domain. The sample is programmed by deforming at T_{prog} followed by cooling under strain to T_{low} for crystallization and shape fixation. During partial heating to T_{sep}, the sample contracts due to MIC of the actuating domain; upon cooling to T_{low}, the sample elongates in the stretching direction due to directed crystallization of the actuation domain (Figure 10B). It was demonstrated that a folded shape B unfolded partially to shape A during heating and contracted back during cooling because strain differences existed at the folding regions, which unfolded during heating and folded during cooling (Figure 10C). These TMPAs were able to be reprogrammed to different shapes while thermally actuated reversibly in free standing state at constant T_{act}, which was tunable by varying T_{sep}. Since the dimension change rate maximized at T_{act}, the reversible actuation with different speed and amplitude were achievable easily by adjusting T_{sep} and controlling the temperature. A copolymer network poly(ε-caprolactone-co-butylacrylate) (coPCLBA) was also proved to be appropriate for TMPAs showing reversible actuation while amorphous materials failed (69). These TMPAs may find application as thermal mechanical engine for energy conversion or smart windows that sense temperature alteration and adjust incident sunlight dose correspondingly.

The above introduced SCPs which have reversible actuation capability in free-standing state present reversible strains between 5 % – 25 % excluding the contribution from thermal expansion. Increase of parameters such as T_{sep}, programming strain, crystallinity and crosslinking density can usually enhance the reversible strain, also called reversibility, which is the ratio of the difference between the programmed strain and the recovered strain to the programmed strain, to different

extents. With the increase of T_{sep}, a larger fraction of crystallites will lie in the actuation domain and thus increase the reversibility. However, the rigid skeleton region will be destroyed if T_{sep} exceeds T_{prog} and as a consequence, the reversible actuation will be lost. If T_{sep} is too low, the percolating skeleton will impede the recovery of the programmed shape during heating as the fraction of melted crystallites is too small. At a properly large programming strain, polymer chains are more oriented and the crystallinity may also be increased, benefiting the increase of reversibility. Crosslinking density is very important as it controls the interplay between the chemical network and the physical skeleton network. Sheiko and coworkers found that the densely crosslinked network of the semicrystalline polymer poly(octylene adipate) (POA) enabled a reversibility as high as 80% and simultaneously the recovery rate was also increased (71).

In addition to the materials introduced above, many other SCPs including polyurethane (PU) (72), poly(ε-caprolactone) (PCL) (73, 74), poly(1,4-butadiene) (PBD) (75), binary PE/PCL or EVA/PCL blends (76, 77), and copolymers of polyethylene glycol (PEG) and poly(butyl acrytale) (PBA) (78), have also been studied, and their thermoresponsive reversible actuation performance in freestanding state varies. Similar to the previously discussed examples, these materials contain crystalline phase and amorphous phase with the crosslinking junctions. The amorphous phase is considered necessary in providing the network elasticity that governs the skeleton shifting, and the junctions allow transfer of the molecular-level conformational alterations into macroscopic dimensional changes, while the oriented crystal growth along the deforming direction is the origin of reversible actuation. Most of the SCPs are actuated by partial melting to maintain the skeleton crystallites for subsequent reversible actuation, except in cases of bilayers where one ultrathin PCL layer (500 nm) is laminated with an inert gelatin layer (1.5 μm) (79). The PCL in this bilayer is so thin that the interfacial interaction is strong enough to keep the PCL chains oriented parallel to the film surface even after complete melting of the crystallites. During cooling, crystallization happens along the confining direction inducing shape recovery. Anthamatten et al. further show that a single phase PCL material crosslinked in two steps also enables two-way reversible actuation even if T_m is exceeded (74). The slightly crosslinked PCL is deformed in melted state with a large strain, followed by further crosslinking to maintain internal stress and high degree of polymer chains orientation. The sample elongates along the stretching direction during cooling, directed by the

built-in stress, and contracts upon heating above T_m, reversibly. Furthermore, physically crosslinked poly(ethylene-co-methacrylic acid) ionomer (80), thermoplastic copolymer elastomers such as polyester urethanes (PEU) and polyolefin devoid of chemical crosslinking have also been found to have load-free reversible actuation behavior under the mechanism of the MIC and CIE, despite the reversible strain is typically low (81, 82). These materials rely on polymer chain entanglements or ionic interactions as physical crosslinking and allow easy processing due to plasticity in melted state, which in turn may also lead to decay of the reversible strain in subsequent actuation cycles.

The wide availability, low cost and property tunability of SCPs greatly promote the development of soft polymer actuators in many fields. Some biocompatibile and biodegradable components such as PCL, PPDL and PEG even offer the possibility of applications in the biomedical field (78, 83, 84). However, to significantly enhance the reversible strain and actuation speed of actuators based on SCPs for higher and faster power output remain very challenging. Besides, the requirement of uniaxial polymer chain orientation during the programming process makes it difficult to design and prepare devices capable of complicated shape morphing and actuation. SCP-based actuators in response to light with functions such as shape morphing and locomotion are still scarce. With more studies underway, SCPs will continue to be a promising candidate for soft polymer actuators.

I.3 Actuators Based on Liquid Crystalline Polymers

Liquid crystalline or liquid crystal polymers (LCPs) are polymeric materials with rigid mesogenic moieties connected to the polymer chain, ether on the backbone or as side groups. Mesogens appear as calamitic or discotic chemical moieties that form liquid crystal (LC) phases with no more than two-dimensional order. Typically, when heated above the LC–isotropic phase transition temperature (T_{iso}), liquid crystals turn to disordered isotropic state; on cooling back, ordered LC phases form again. Several important and common LC phases are shown in Figure 11a. In nematic phase, mesogens orient preferentially along one direction, termed LC director, but have no positional order. In smetic A and C phases, however, oriented mesogens are confined within layers and thus have both orientational order and positional order, with the director parallel or tilted to the normal to the layer surface, respectively. For cholesteric phase, also called chiral nematic phase, the directors of mesogens in layers twist around an axis normal to the surface plane. As illustrated in Figure 11b, mesogens may sit on the main chain forming main-chain LCPs, or are part of the side group in side-on or end-on manners, forming side-chain LCPs. Some representative mesogenic monomers and crosslinkers are shown in Figure 12. LCPs can be synthesized by grafting reactive mesogenic groups onto polymer chains under thermally initiated reaction with presence of initiator or through radical polymerization of reactive mixture of mesogenic monomers, crosslinkers and initiator under UV light (85). In addition, polycondensation reaction between bifunctional mesogens is also an important method (86-89), and ring-opening metathesis polymerization is favored for well-controlled molecular weight and narrow polydispersity (90-92). LCPs are often subjected to crosslinking during or after synthesis, forming liquid crystalline polymer networks (LCNs) for construction of polymer actuators. Lightly crosslinked LCPs with T_g lower than RT are termed liquid crystalline elastomers (LCEs) due to the flexibility of the polymer chains under ambient conditions. Side-chain LCEs were first synthesized by Finklemann et al. by attaching the vinyl terminated mesogenic molecules to polymethylsiloxane chain through hydrosilylation reaction, with presence of the less active crosslinking component and initiator (93). In a typical two-step crosslinking process, the polymer is initally crosslinked slightly during synthesis, and then deformed under constant load to a certain strain. During deformation, the mesogens are aligned with rotation of local LC directors toward the stretching direction due to

coupling with the polymer chains and finally orient uniformly along the stretching direction. An LCP sample having a uniform orientation of mesogens is considered as having a monodomain structure, while the sample before the formation of uniform orientation has the mesogens in a polydomain structure with random distribution of local LC directors (94). Such polydomain-monodomain (P-M) transition is an important programming step for actuators using LCEs or LCNs (95). The monodomain should be further crosslinked to lock the network anisotropy. Nematic LCEs programmed as such can even be free of orientation defects and therefore called nematic liquid single crystal elastomers (94). Such LCEs actuators in the form of strips or films contract in isotropic phase and elongate in LC phase along the LC director (often the strain direction), as shown in Figure 11c, while in the orthogonal directions the opposite changes occur. The reversible actuation stems from the cooperative interplay between the LC order and the elasticity of the crosslinked polymer network. In isotropic state the mesogens are disordered and the polymer chains contract to random coils driven by entropy increase, while in LC state mesogens orient to ordered state accompanying elongation of the polymer chains. Particularly, the reversible actuation of LCEs can proceed both under constant stress and free of stress. The reversible degree (RD) in response to temperature change is the ratio of the length difference between the LC state and the isotropic state to the length in isotropic state. Since the pioneering work of Finklemann (94), the reversible actuation driven by the order-disorder thermal phase transition has aroused great interest in studying LCNs as polymer actuators (96). When photochromic azobenzene derivatives are incorporated as monomer or crosslinker into LCNs (Figure 12), the photoisomerization between the calamitic *trans*-isomers in ordered state and the bent *cis*-isomer in disordered state can also govern the reversible actuation by coupling to the order parameter change (97). Numerous works have been done on exploring azobenzene-containing LCNs (azo-LCNs) as photoresponsive polymer actuators (29, 98, 99).

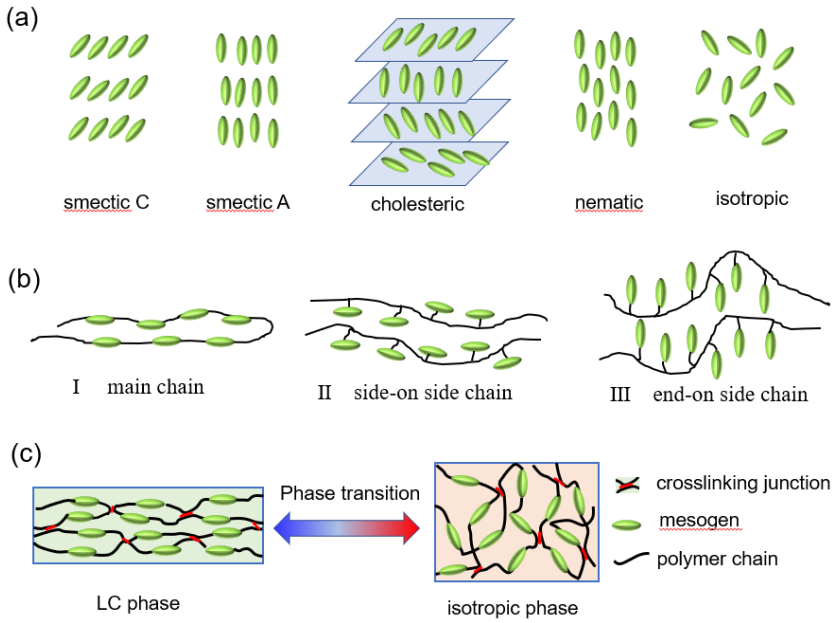

Figure 11. Schematic presentation of liquid crystals, liquid crystal polymers/networks and their actuation. (a) Several common liquid crystal phases. (b) Liquid crystal polymers with various ways of mesogen attachment to the polymer backbone. (c) Reversible actuation of LCNs driven by an order-disorder phase transition.

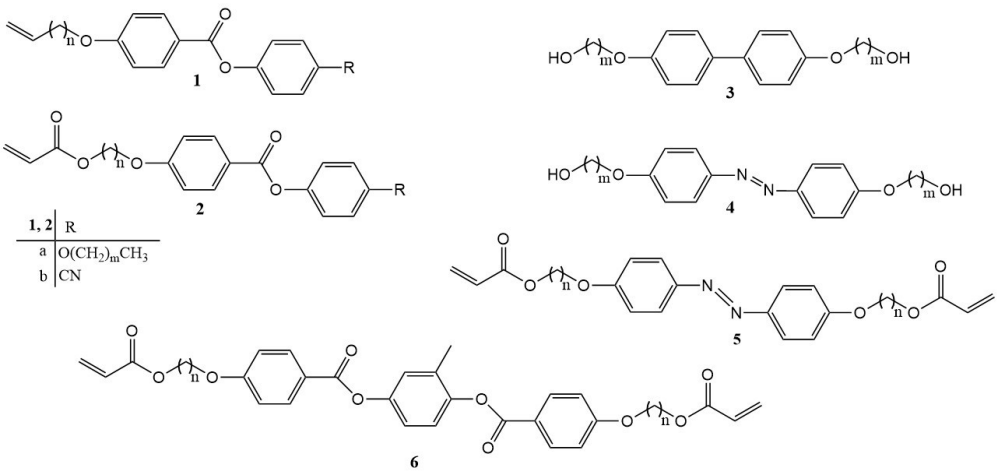

Figure 12. Chemical structures of mesogenic phenyl benzoate monomers (**1** and **2**) and crosslinker (**6**), biphenyl monomer (**3**), azobenzene monomer (**4**) and crosslinker (**5**).

Forming crosslinked monodomain plays a critical role in preparing LCNs-based actuators capable of reversible actuation. Mechanical deformation to date is still an important and frequently used programming step to induce the polydomain-monodomain transition in synthesized LCPs, after which the monodomain can be crosslinked by radicals or UV light (100-104). Fibers could be drawn by pulling from polymer melt mixed with diisocianate as the crosslinker, followed by crosslinking to fix the orientation (105), or spun from a spinning machine (88). A microfluidic device could even produce aligned microparticles as well as fiber (106), which were crosslinkable by UV light. In terms of lifting weight (Figure 13a), LCN fibers remain highly competitive as they can be bundled together and each of them is highly aligned with excellent mesogen orientation and high RD. In conventional two-step crosslinking method, the oriented polymer chains are crosslinked by radicals uniformly fromed in the film or strip, and the obtained sample can only perform uniaxial contraction-expansion upon stimulation as a result of the uniform crosslinking of the monodomain (100, 104). To achieve asymmetric actuation like bending-unbending, laminating an uniaxially oriented layer of LCNs with a passive layer is an effective option (107), although delamination poses a threat to the service life. Dynamic transesterification that can be activated by heating and photothermal heating has recently been introduced to LCNs to allow for local and selective formation of monodomains, which endow the samples with reversible bending/unbending, protruding/receding and more asymmetric shape changes and motions (108-110). Nevertheless, different shapes were individually stretched to induce monodomain and needed assembling through the transesterification-induced welding to obtain more sophisticated shapes, most of the time manually, thus restricting the production efficiency and flexibility. Our group has recently developed UV-crosslinkable LCPs containing cinnamyl groups which permits flexible spatial inscription of the monodomain into desired regions of an LCP film by patterned crosslinking of the active monodomain, while the uncrosslinked regions were relaxed in isotropic state to inactive polydomain (102, 103). The resulting LCE actuators comprising heterogeneous distribution of polydomain and monodomain exhibit 3D structures under structured actuation, and demonstrate reversible, flexible and complex shape changes as shown in Figure 13b. As a further development, by incorporating anthracene derivative as the reversible photo-crosslinker, complicated 3D structures were proved reconfigurable by selectively decrosslinking local

monodomain from a uniformly crosslinked shape in monodomain (Figure 13c), and reversible actuation were preserved in the meantime (101). These UV-crosslinkable LCPs were subjected to plastic mechanical deformation to induce the P-M transition, thus the available thickness and production efficiency may be limited. The patterned crosslinking/decrosslinking ideally should make unlimited structured actuation possible provided that different photomasks are available. More interestingly, the softness of the materials makes them very appealing for preparing biomimetic soft polymer actuators.

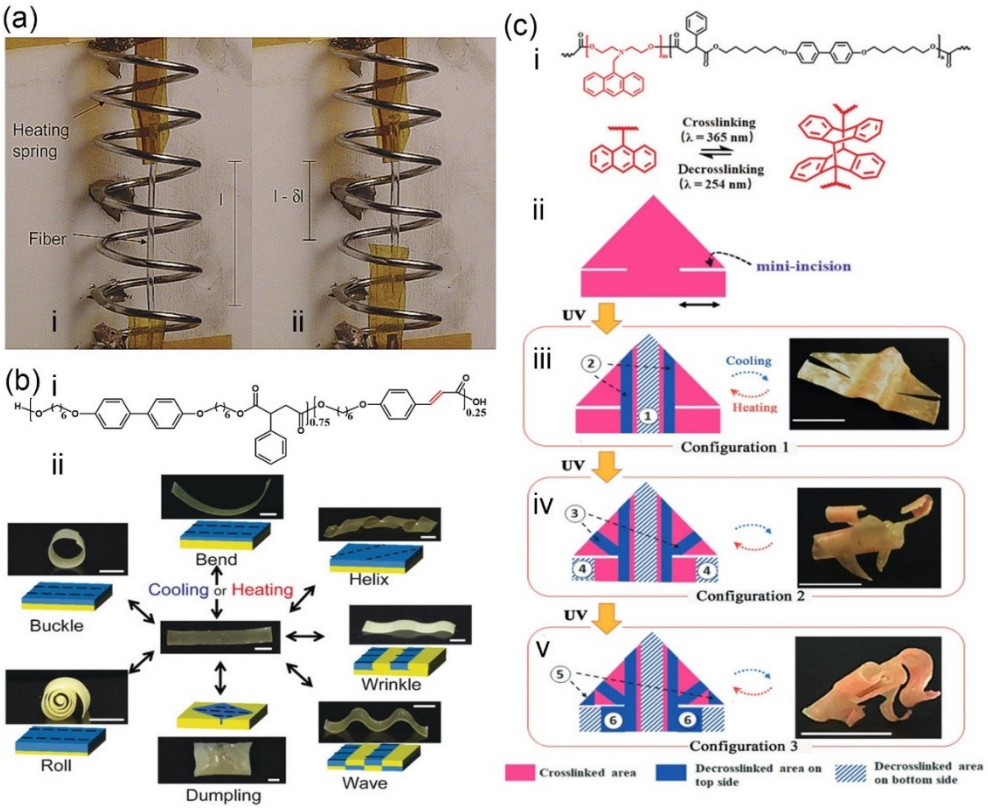

Figure 13. (a) A side-chain LCE fiber actuating under a load of 0.002 N. The fiber is extended in nematic LC state (i) and contracted in isotropic state (ii). Reproduced with permission from [105]. Copyright 2003, American Chemical Society. (b) Chemical structure of the UV crosslinkable main-chain LCE material (i) and 2D-to-3D reversible thermal actuation of programmed structures (ii). Scale bars: 2 mm. Reproduced with permission from [102]. Copyright 2017, Wiley-VCH. (c) Chemical structure of the UV crosslinkable and decrosslinkable anthracene-containing LCE (i)

and reconfiguration from uniformly crosslinked LCEs through UV light-induced decrosslinking of selected regions in monodomain (ii–v). Scale bars: 0.5 cm. Reproduced with permission from [101]. Copyright 2019, Wiley-VCH.

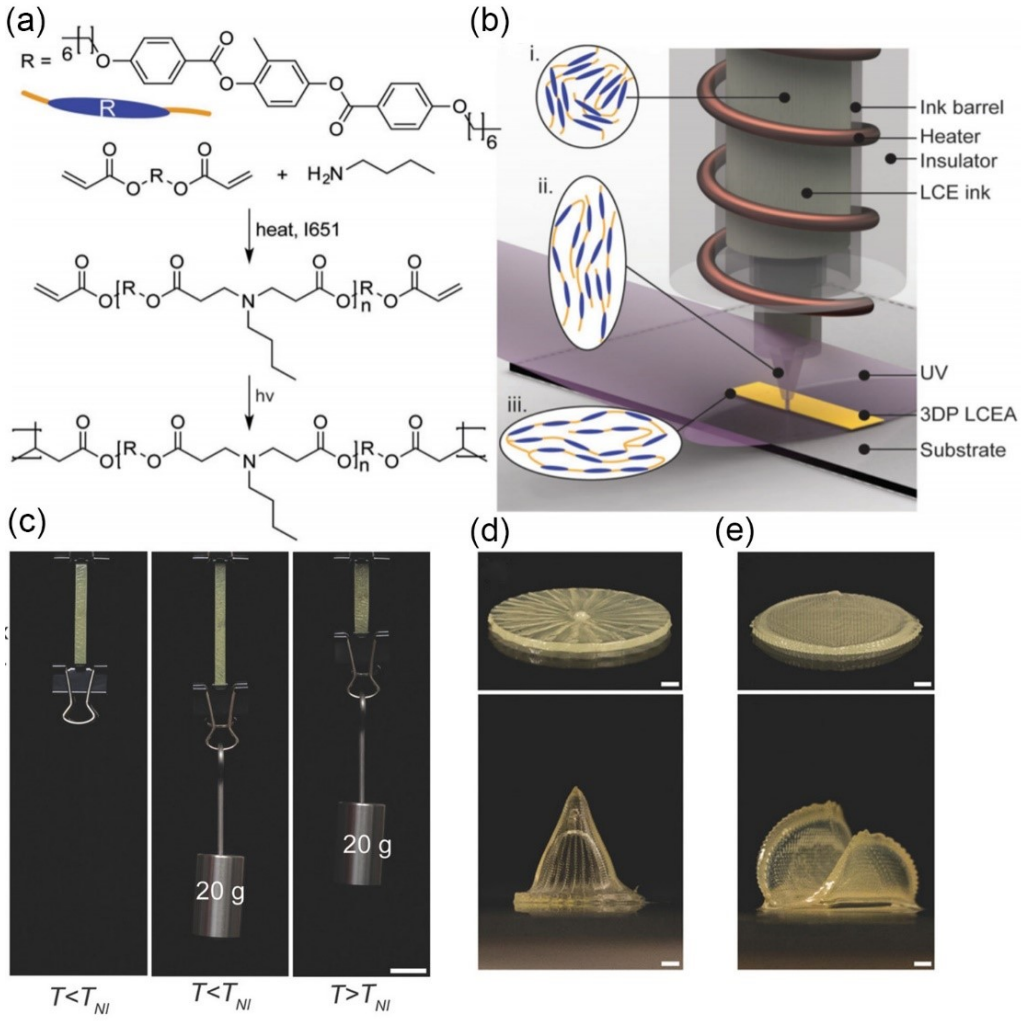

Figure 14. (a) Composition and synthesis of the photopolymerizable LCE ink containing a spacer (yellow chain connected to the mesogen), mesogen (R) and initiator (I651). (b) Schematic illustration of 4D printing LCE-based actuators by direct ink writing followed by UV crosslinking. The disordered ink in the barrel (i) is extruded and aligned through the nozzle (ii) along the printing path, resulting in oriented (iii) LCE filament. (c) Images of the LCE actuator (1 mm-thick) printed with uniaxial printing path. Left, free of load in nematic phase; middle, under load of about 0.2 N

in nematic phase; right, actuating in isotropic state under load of about 0.2 N. Scale car: 10 mm. (d, e) Images of disc-shape LCE actuators (about 0.4 mm-thick) printed along spiral (d, top) and perpendicular (e, top) paths. On heating to isotropic state, the disc-like shapes morph into a cone (d, bottom) or a saddle (e, bottom) shape. Scale bars: 1 mm. Figures are reproduced with permission from [111]. Copyright 2018, Wiley-VCH.

Mechanical deformation is simple and fast while spinning or extrusion lacks flexible design of the geometric configuration, especially when design and production of complex 3D structures are encountered. 3D/4D printing provides a potential solution to those issues as it allows computer-aided design and controllable and autonomous production in large scale. 4D printing integrates the stimuli-responsiveness into the material used in 3D printing and produces 3D structures capable of shape changing, morphing and dynamic motions. Directly printing LCPs before crosslinking is impractical because of two factors. One is the high viscosity of the polymers in LC state; the other is the difficulty in forming monodomain after printing the isotropic polymer melt. Recent progress has succeeded in printing oligomer inks with much lower viscosity through direct ink writing (DIW) on the substrate, accompanied by subsequent UV-initiated radical polymerization to lock-in the LC orientation (111-114). The alignment of mesogens during printing is in fact induced along the print path by the shearing force during extrusion, as illustrated in Figure 14b. Not only multilayer strip capable of reversible uniaxial deformation was easily printed in this way, but also dynamic 3D structures responsive to temperature change were formed from printed planar sheets (113). Figure 14c shows that the printed strip could lift weight 1000 times their own weight during thermal actuation (111), confirming the excellent actuation performance. 2D planar sheets with spiral and vertical alignments of mesogens were thermally morphed to 3D cone and saddle shapes, respectively, as seen in Figure 14d and 14e, and partially recovered on cooling to LC state. More complex structures such as helix, mesh and honeycomb, and motion like snap-through have been realized by 4D printing (112, 113), which paves the way to customizing LCN actuators for desired functions and large scale industrial production. To print microstructured LCN-based actuators with micron-scale resolution, however, is still challenging. Direct laser writing techniques based on two-photon absorption polymerization can greatly enhance the resolution, and micron-sized gratings and robots have been fabricated (115-117).

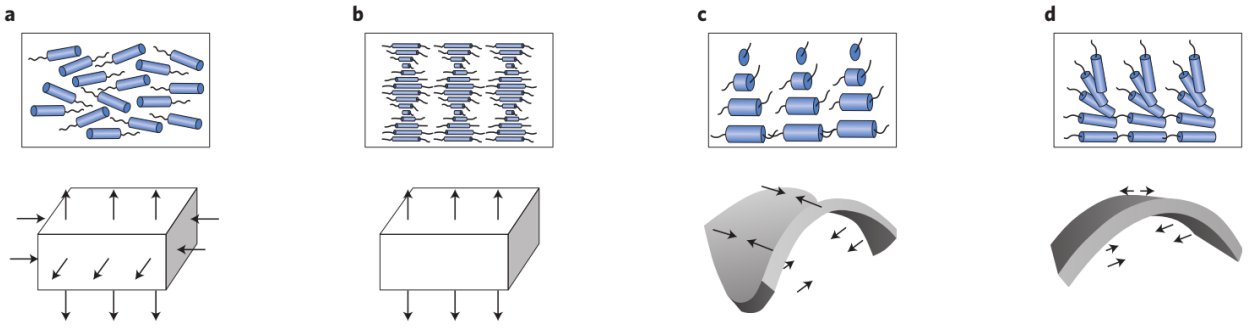

Figure 15. Director profiles of (a) planar uniaxial, (b) cholesteric, (c) twist nematic and (d) splay configurations and their corresponding deformations with a decrease in order parameter. Arrows indicate the direction of deformation. Reproduced with permission from [118]. Copyright 2015, Springer Nature.

LCPs or weakly crosslinked LCEs need to be mechanically deformed to induce molecular orientation of mesogens which can then be retained following weak elastic recovery and crosslinking. However, the mechanical deformation approach cannot be applied in all situations and for all actuating devices. The mesogen orientation during each individual deformation step such as the manual uniaxial drawing, fiber spinning and extrusion during 3D printing, is uniaxial, uniform and 2D at most. This indicates that heterogeneous distribution of the mesogen orientation in 3D cannot be obtained directly; instead, most of the time additional steps such as relaxation in isotropic phase, gradient crosslinking and layer-by-layer printing need to be implemented. As a result, the types of available 3D structures are inadequate and the motions are either simple combinations of expansion-contraction in different directions or mainly comprised of bending-unbending. 3D printed structures enable more complex shape changes and actuation, but the concern is the strength of interlayer bonding, which may be weak considering the attenuation of UV light during crosslinking. To acquire more complicated structures and natural shape morphing, especially in a single material and in less steps, more programming techniques of distributing the mesogen directors (i.e. director profiles) in not only planar directions, but also in thickness direction or even titled directions, are needed. The solution to this issue can be found by orienting the mesogenic monomers to desired directions first, then polymerizing and crosslinking the aligned mesogens to obtain LCNs with sophisticated director profiles (118).

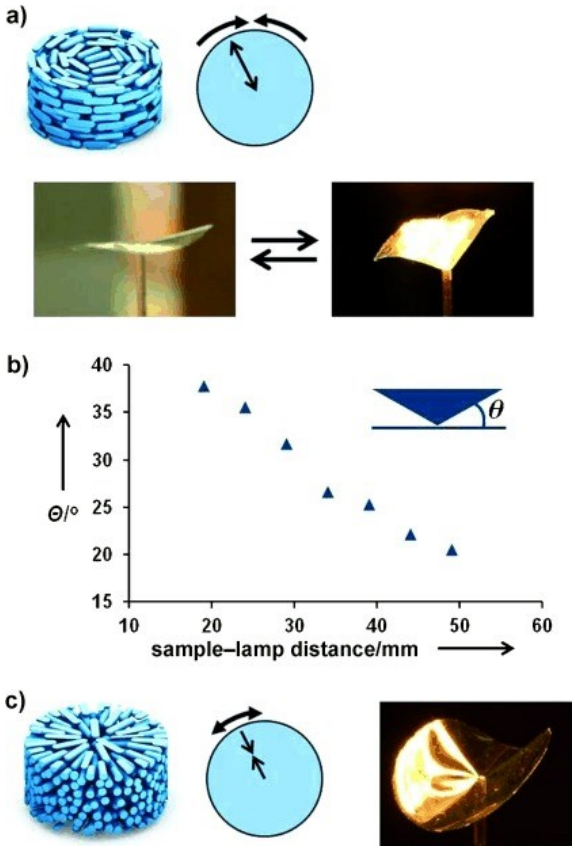

Figure 16. (a) Actuation of an LCN film with azimuthal alignment and a +1 topological defect by an IR lamp. (b) Angle of the upward bend of the cone as a function of the sample-to-lamp distance. (c) Actuation behavior of an LCN film with radial alignment. The arrows along the radius and the periphery indicate the direction of deformation. Reproduced with permission from [119]. Copyright 2012, Wiley-VCH.

To this regard, surface-alignment treatments involving photoalignment, surface rubbing and surface-channels confining, are most effective in tuning the LC directors in planar and thickness directions, while magnetic fields can control the tilting angle of mesogens to the sample surfaces. Figure 15 shows several director profiles including planar, cholesteric, twisted nematic and splay orientations enabled by surface alignment layer and their corresponding shape changing upon actuation (118). Surface alignment methods rely on special alignment layers on which LC monomer mixtures are loaded, aligned and polymerized to prepare anisotropic LCNs. The monomer and crosslinker are usually mesogenic monoacrylate and crosslinkable diacrylate LC

molecules, which are polymerizable under UV light in the presence of light-active initiator (120). The substrate material for photoalignment can be azobenzene- or cinnamate-based materials (121, 122), which are able to be oriented perpendicular or parallel by lineally polarized light to the light polarization direction. Surface rubbing by a velvet cloth on polyimide surface creates microgrooves that orient mesogens toward the rubbing direction (123, 124), and surface microchannels with designed structure can confine the mesogen orientation in controlled directions (125). The established anisotropy of the alignment layer can be transferred to the loaded LC monomers and preserved after polymerization and crosslinking. Photoalignment facilitates the development of discrete mesogen orientations in plane which allows 2D-to-3D shape morphing upon actuation. Azimuthal and radial alignments on LCN films were achieved by Broer et al. using photoaligment and developed into cone and anticone structures (Figure 16), respectively, on photothermal actuation (119). There is a topological defect in the middle of each of the azimuthal and the radial patterns, with a defect strength (m) of +1. The value of m dictates the result of shape morphing. White et al. extended the application to LCN films containing arrays of the topological patterns with different defect strengths, forming nine cones with high stroke from a flat film and other more complicated structures containing shapes mimicking valleys and dimples (126-128). Photoalignment enables very high resolution of oriented domains while the photoalignment process is slow. Instead, surface rubbing or channel confining method contributes to faster transfer of anisotropy to the loaded LCNs. However, as the rubbed surface is uniaxially oriented, the resulted orientation of LCNs remains uniaxial. Yang et al. used patterned crosslinking to crosslink the exposed monodomain first, followed by crosslinking the rest in isotropic phase, thus creating inert polydomain regions neighboring active monodomain. By adjusting the pattern line direction with respect to the rubbing direction and cutting the film at different angles, bending, curling and accordion-like folding were achieved (129). Moreover, applying two parallel alignment layers with distinct orientations helps to change the mesogen orientations across the film thickness, inducing twist nematic alignment at presence of chiral dopants when the two alignment layers have orthogonal orientations or splay alignment when one of the alignment layers induces homeotropic alignment (130, 131). In twist nematic alignment, the director rotates in plane for totally 90^{o} across the thickness (Figrue 15c), while in splay alignment the director changes gradually from planar to

homeotropic (Figure 15d). Likewise, patterned crosslinking can be applied concomitantly to enrich the director profile. Cholesteric LCNs formed from rubbed surface vary in mesogen orientation in plane only, thus patterned crosslinking was introduced to create surface corrugation upon actuating the film (132). In twist nematic LCN films, the cutting angle and aspect ratio were also adjusted as important parameters, giving helical ribbons and helicoidal structures (130, 133). Monodomain with uniaxial mesogen orientation and twist nematic domain were combined in alternative manners in a film, producing localized curls (130).

LC mesogens are well known to be readily aligned by magnetic fields. The field direction can be adjusted arbitrarily, which renders desired encoding of mesogen orientation into LCNs structures along different directions. Aizenberg et al. have shown various actuation modes in a hexahedral microplate based on an LCE material, where the mesogens could be aligned parallel to different planes and along different angles, resulting in uncommon in- and out-of-plane tilting and twisting of the plate (134). By applying spatially gradient magnetic fields during synthesis, the resulting LCEs molded as micro-array showed a gradient of tilting angles upon actuation. Patterned magnetic fields were also employed to induce non-uniform mesogen orientations of the microstructure array, and the obtained different deformation modes enabled information storage.

Shape changing or shape morphing for LCN-based polymer actuators described above only partly reflect the actuation concept. A more significant purpose of actuation lies in the ability to do physical work, which can be represented by the advanced functions such as locomotion, including walking or crawling (135, 136), jumping and swimming (137, 138); and autonomous motions such as oscillation (139-144), continuous rotation and consistent rolling (145-147); intelligent actions such as object recognition (148, 149), and sense-and-actuate abilities (149, 150). While some of these functions can be enabled by other stimuli such as moisture (151), organic solvent and pH scale (20, 152), most of the functions are realized under light control. Light as a clean energy has many advantages such as wireless and remote manipulation, local control, less noise and broad range of wavelengths. Photothermal and photochemical effects are the two main sources for the actuation of LCN-based actuators. Photothermal actuation usually requires incorporation of species such as CNTs (153), graphene (154), gold nanoparticles (155), dyes (156), conjugated

polymers and so on (100), which absorb light and release heat, heating LCNs to reach the threshold value of the phase transition temperature. Visible and near-Infrared (NIR) light are generally preferred to UV light as they are human-friendly and can penetrate deeper in case for biomedical applications. In contrast, photochemical actuation needs specially designed structure of the LCNs, usually azo-LCNs, and both visible light and UV light are generally involved for alternating irradiation. Figure 17 showcases some of the fascinating functions enabling output of physical work. A "Ω"-shape microrobot with splay alignment of mesogens (Figure 17a) expanded toward flat shape under illumination of 488 nm wavelength visible light and recovered when the light was off, mimicking the locomotion of a caterpillar (136). The alignment of mesogens was homeotropic in the bottom side while planar in the top. The photothermal effect arising from Disperse Red 1 (DR1) derived the order-disorder phase transition that induced expansion in the lower side and contraction in the upper side. On a ratchet substrate surface, the previous deformation was directed, and displaced the microrobot body when the light was off. For a uniaxially oriented submillimeter-scale cylinder based on azo-LCNs, dynamic structured light with periodic patterns was projected on the surface and scanned from one end to the other at a constant frequency, achieving peristaltic locomotion in fluid (Figure 17b) (138). The radial expansion and longitudinal contraction of the exposed section propagated as traveling deformation waves along the cylinder, as shown in Figure 17b (i and iii), dragging the surrounding liquid and propelling the cylinder opposite to the laser scanning direction. This true microswimmer was simply made from a uniaxially pulled fiber, leading the way to achieving biomimetic locomotion of LCN-based devices with simple director profiles by applying dynamic structured light, which is a periodic light pattern of bright and dark regions (138). In contrast to using structured light, White et al. successfully realized autonomous oscillating in monodomain azo-LCNs cantilevers by constant laser illumination (139, 144). Autonomous motion of an actuator indicates that once the actuation is initiated by a stimulus or signal, the motion can be self-sustained without external intervention (i.e. without on/off switching of the stimulus). Figure 17c shows that the originally vertically placed azo-LCNs cantilever was continuously exposed to laser illumination in the front surface and the back surface sequentially as it was inertially deflected through the beam path, establishing a downstroke-upstroke-downstroke feedback loop. The frequency could be tuned from tens of Hz to about 270 Hz by

varying the aspect ratio, while the amplitude of oscillation decreased with atmospheric pressure, indicating that light energy was transformed to mechanical energy of the cantilever, which also accomplished physical work to the surrounding air. The photodriven oscillating cantilever was also achieved in LCNs with splay alignment of mesogens based on the self-shadowing photothermal effect, although the frequency was lower (140, 157). Broer et al. further demonstrated that by exposing oblique-incidence UV light to a constrained azo-LCN strip with fast *cis*-to-*trans* thermal relaxation, continuously propagating waves could be generated, under the self-shadowing mechanism (142). The direction of the wave was dictated by the mesogens in splay alignment. As Figure 17d (i) shows, the wave moved away from the light source when the planar side faced up and propagated toward the light source when the homeotropic side was up (142). The propagating waves were able to shake off objects on the strip surface, as shown in Figure 17d (ii), manifesting a surface self-cleaning function. When confined in a frame, the framed strip could also perform light-driven locomotion. Figure 17e shows that a spiral azo-LCN strip with twisting nematic alignment was prepared and driven to roll intermittently from left to right under constant irradiation of broad spectrum UV-visible light (320-500 nm) (146). As the spiral strip was irradiated from above, the upper portion tended to twist tighter than the lower shadowed portion due to gradient photostrains across the thickness. As the photostrains were accumulated, the net twist moment overcame the opposed resisting moment arising from friction, inducing slip of the spiral structure. Once the rolling was initiated, a new portion of the surface would be irradiated and thus leading to perpetual self-sustained directional rolling. These azo-LCN strips could roll on an arbitrary surface and even climb an inclined surface. Some other LCN-based actuators have been endowed with intelligent functions mimicking the motion of natural species, for instance, a flytrap capable of opening and closing automatically. An artificial flytrap was prepared by integrating a splay-aligned LCE film into the tip of an optical fiber, as Figure 17f (i) shows, from which blue light laser was emitted through a transparent window on the LCE strip (149). When an object went into the field of view of the device and produced enough reflected/scattered light as optical feedback, the actuator bent due to photothermal heating toward the object and finally closed to have it captured (Figure 17f, ii and iii). The actuator was also able to respond to non-reflective objects which could not emit light but absorb and transfer light into heat, heating the LCE material

through diffusion. As the latter feature was slower, the actuator might be used to distinguish different objects. The ability of recognition was further demonstrated by a splay-aligned LCE microactuator fabricated by DLW (148). When the green laser was illuminating around the microactuator, a black or purple object with its absorption spectrum matching the illuminating light wavelength (Figure 17g, i) could be captured as it approached the actuator, as seen in Figure 17g (ii and iii), while yellow or white objects induced no response.

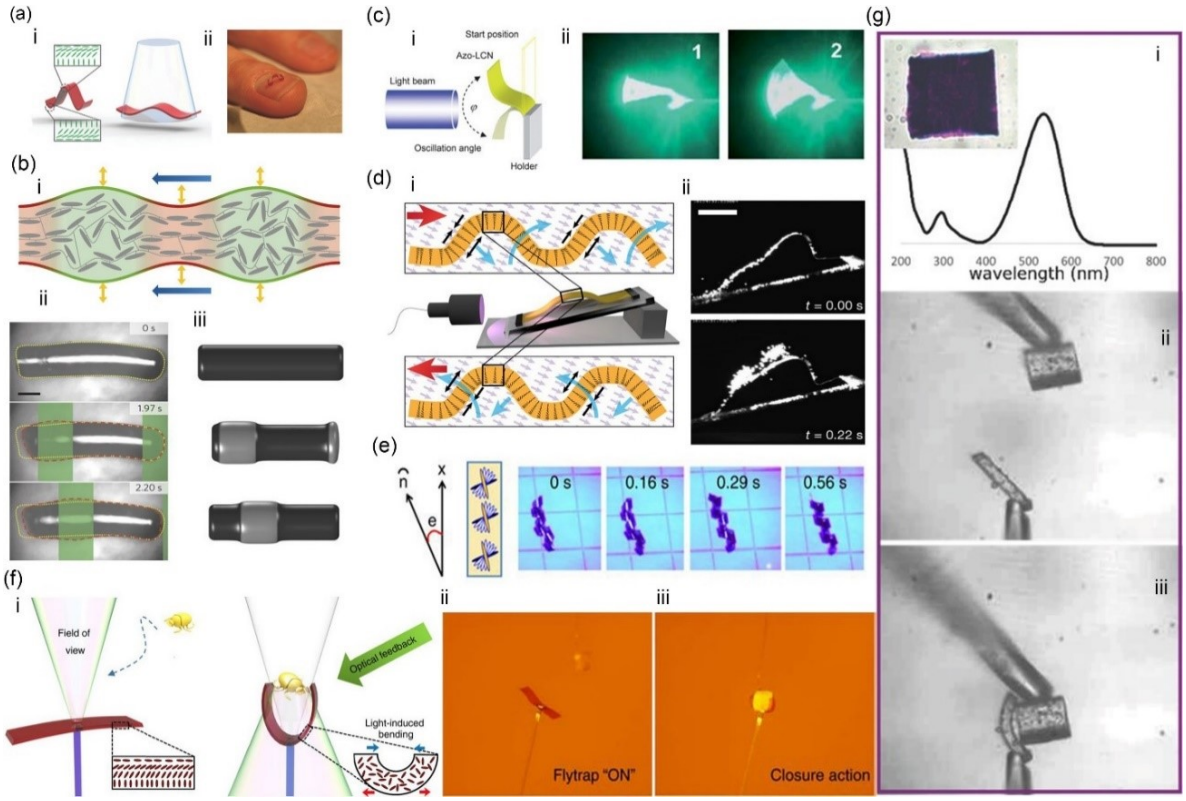

Figure 17. Photodriven LCN-based actuators. a) An inching walker with splay alignment (i) on a human finger (ii) (136). b) Microswimmer actuated by structured light (138). i, schematic illustration of selectively actuated soft microrobot; images (ii) and models (iii) showing the locomotion and travelling waves of the microswimmer under green light laser scanning from left to right. c) Schematics (i) and snapshots (ii) of an oscillating azo-LCN strip (139). The power levels are 76 mW (1.08 W cm^{-2}) (ii, 1) and 85 mW (1.2 W cm^{-2}) (ii, 2). d) Generating oscillating waves in an azo-LCN strip confined at two ends (i) and the light-driven self-cleaning behavior (ii) (142). e) Light-induced autonomous rolling of a spiral azo-LCN strip in twist nematic alignment

(146). The director offset is 15° on the top and -75° at the bottom, respectively, to the long axis of the strip. Upon irradiation with 320-500 nm light of 200 mW cm^{-2}, a spiral ribbon forms and rolls to the right under continuous irradiation. f) Schematics and images showing the working principle of an artificial flytrap (149). It closes as an object enters the field of view and produces enough optical feedback (i, ii) and finally captures the object (iii). g) UV-Vis absorption spectrum (i) of a purple object which absorbs light, heats the microactuator and gets captured (ii, iii) (148). Figures were reproduced with permission from: a, ref. [136]; b, ref. [138]; c, ref. [139]; d, ref. [142]; e, ref. [146]; f, ref. [149]; g, ref. [148]. Copyright: a, 2017, Wiley-VCH; b, 2016, Springer Nature; c, 2010, the Royal Society of Chemistry; d, 2017, Springer Nature; e, 2016, The Author(s) of ref. 146, and f, 2017, The Author(s) of ref. 149, both licensed under a Creative Commons Attribution 4.0 International License; g, 2017, Wiley-VCH.

The actuation of LCN-based soft polymer actuaors is intrinsically driven by the order-disorder phase transition, which can be induced by various external stimuli. An actuator capable of responding to multistimuli and performing multiple functions is highly desired; however, the integration of multi-responsiveness and multifunctionality into a monolithic material is a significantly challenging task. As artificial intelligence is probably leading a new industrial revolution, efforts devoted to the research and development of such LCP-based polymer actuators are extremely valuable and appealing as smart materials allow for numerous functions and applications, some of which are worthy of more exploitation. Only a limited number of multistimuli-responsive LCN-based actuators have been reported (134, 158, 159), and much research remains to be done, especially on multifunctional actuators controllable by one stimulus such as light. To develop photodriven monolithic LCN-based actuators that possess multifunctionality will be a big step forward for more intelligent actuators and deserves continuous investment.

I.4 Objective of the Thesis

The main objective of this thesis is to propose and explore novel strategies and approaches to achieving new soft polymer actuators with enhanced performance or multiple functionality driven by an order-disorder phase transition induced by heat or light. We utilize photothermal effect to

control both directional melting–crystallization in semicrystalline polymers containing gold nanoparticles and LC–isotropic transition in LCPs doped with a dye. In addition, we put forward a new concept and establish new strategies for realization of robust functions of polymer actuators. The research works described in this thesis mainly comprise two parts following the introductory section and are presented in the form of published papers in three chapters.

The first part reports our progress on developing optical actuators and thermal actuators based on crosslinked EVA, a semicrystalline polymer. In Chapter 1, we have incorporated modified EVA-stabilized AuNPs into EVA matrix and prepared EVA/AuNPs composite actuators controllable by a laser. The object of this project is to investigate the mechanism governing the light-controlled reversible actuation, study the effect of parameters such as laser intensity, laser power varying speed, AuNPs content, elongation and thickness of the composite on the actuation speed and magnitude, and demonstrate the potential application. Chapter 2 reports a novel function of the EVA-based actuators, which can oscillate continuously on a surface of constant temperature. We put forward the "thermo-mechano-thermal feedback loop" concept for the first time and investigate the effect of substrate temperature, sample thickness and sample elongation on the oscillating amplitude and period. Additionally, we have proved the direct thermomechanical energy conversion of the actuators undergoing self-walking and pumping a wheel rotation.

The second part aims at integrating photomobile multifunctionality into a monolithic LCE actuator. In Chapter 3, we create hierarchical layers composed of crosslinked polydomain and monodomain in dye-doped LCE strip actuators and study the light-guided transportation, flexible locomotion and multiple modes of autonomous motion. We show multiple types of light-driving actuation: an object placed on the strip actuator can be transported from one end to the other when scanned with an NIR laser, the soft actuator can perform turning in locomotion, and a suspended arm under constant laser illumination can execute self-sustained motion of various modes dictated by the laser incident angle.

In Chapter 4, the thesis is concluded with general discussion and proposition of some new ideas for future research works that deserve exploration.

CHAPTER 1 AN OPTICAL ACTUATOR BASED ON GOLD-NANOPARTICLE-CONTAINING TEMPERATURE-MEMORY SEMICRYSTALLINE POLYMERS

1.1 About the Project

Optical polymer actuators embody conversion of light energy into mechanical energy and can be reversibly actuated by light. The tunability in wavelength, intensity, polarization and patterning for light enables spatial and temporal manipulation of the actuation. Most optical actuators known to date are based on azobenzene-functionalized LCPs, which require not only polymer structure design and synthesis often at high cost, but also usage of high energy, often detrimental UV light as the stimulus. In contrast, many SCPs are commercially available and cheap. They possess well-known rSME due to a broad melting temperature range and allow thermal actuation between different shapes, which may be regulated by light as well with the presence of a small amount of photothermal additives. We envision that AuNPs with high extinction coefficient and tunable surface plasmon resonance (SPR) band can be dispersed into SCPs to prepare optical actuators. Semicrystalline EVA, a random copolymer with polyethylene segments functioning as the crystallizable segments, is chosen as the matrix material and at the same time modified as ligand of AuNPs to stabilize their dispersion in EVA. A laser is used as the light source that permits distant, wireless and locoal control of the melting and anisotropic crystallization in the actuator. We explore the actuation mechanism and the conditions under which the reversible actuation can be driven by the light-induced order-disorder phase transition. Parameters including the content of AuNPs, laser power density, power decreasing rate, sample elongation and sample thickness are investigated to reveal their effect on the actuation magnitude and speed. The durability of reversible actuation of the actutaor is proved robust through hundreds of cycled actuations without performance deterioration, and potential application as part of an optical switch is demonstrated.

1.2 Contributions

This work was published in *Angewandte Chemie International Edition*, **2017**, *56*, 6126 by Feijie Ge, Xili Lu, Jun Xiang, Xia Tong and Yue Zhao. The research was conducted in Université de Sherbrooke under the supervision of Prof. Yue Zhao. Prof. Zhao and I designed the experiments in the study. I conducted most of the experiments and characterizations, including synthesis and surface modification of gold nanoparticles (AuNPs), preparation of EVA/AuNP composite films and actuators, spectral measurements, thermal properties measurements, photothermal tests, the reversible actuation measurements and photomechanical force tests. I processed all the data and produced all the Figures, Tables and Schemes. Xili Lu helped with the thermogravimetric analysis of the polymer-stabilized AuNPs. Jun Xiang helped with analysis of the UV-Vis spectra of AuNPs. Xia Tong assisted in the photomechanical measurements of several strips made from the polymer/AuNP composites. All co-authors participated in the discussion during analysis of all the data. I wrote the first version of the manuscript and submitted it to Prof. Yue Zhao for modification, revision and finalization.

1.3 Paper Published in Angewandte Chemie International Edition 2017, 56, 6126.

An Optical Actuator Based on Gold-Nanoparticle-Containing Temperature-Memory Semicrystalline Polymers

Feijie Ge, Xili Lu, Jun Xiang, Xia Tong, and Yue Zhao*

Département de Chimie, Université de Sherbrooke, Sherbrooke, Québec, J1K 2R1, Canada.
E-mail: yue.zhao@usherbrooke.ca

1.3.1 Abstract

Photoresponsive actuators based on semicrystalline poly(ethylene-co-vinyl acetate) (EVA) loaded with small amounts of gold nanoparticles (AuNPs) are described. Upon absorption of light (532 nm), the heat released by the AuNPs raises the temperature in the irradiated region to T_{light} to melt crystallites with lower melting temperatures ($T_m < T_{light}$), resulting in a contraction force on the sample sustained by the crystalline skeleton domains with $T_m > T_{light}$. Once the light is turned off, the recrystallization of oriented chains in the actuation domains upon cooling gives rise to an expansion force. We show that the photoinduced contraction force, T_{light}, and the speed for reaching T_{light} can readily be adjusted, which makes EVA/AuNP a robust, fast optical actuation system tunable in both speed and magnitude. The material design can easily be extended to other temperature-memory semicrystalline polymers in combination with various light-absorbing and heat-generating additives.

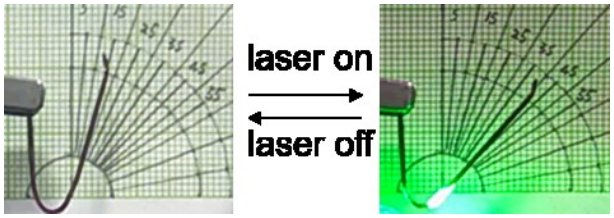

1.3.2 Introduction

Reversible shape memory polymers (rSMPs), which can transform reversibly between a temporary and a permanent shape, are promising candidates for polymer actuators.[1] Generally, SMPs have a crosslinked network structure to maintain the original shape; they can be deformed above a phase-transition temperature T_{tr} (glass transition T_g or melting temperature T_m) and then cooled under strain to $T < T_{tr}$ for fixation of the temporary shape. During this programming process, mechanical energy is stored as potential energy.[2] Upon applying an external stimulus that brings the SMP to $T > T_{tr}$, the polymer recovers its original shape owing to entropic elasticity. Aside from direct heating, other stimuli such as light,[3] ultrasound,[4] and magnetic fields[5] can also be used through a stimulus-induced heating effect. Unlike traditional one-way SMPs that need reprogramming of the temporary shape for reuse, rSMPs are capable of repeated cycles of shape transformation upon changes in temperature. Generally, rSMPs are liquid crystalline elastomers (LCEs) or networks (LCNs) whose reversible shape change (e.g., contraction/extension) is governed by a thermal LC–isotropic phase transition.[6] Using azobenzene mesogens, reversible shape change (bending/unbending) can also be achieved by means of UV and visible-light irradiation as a result of the *trans–cis* photoisomerization of azobenzene.[7] As LCEs and LCNs are specialty polymers, the usually demanding synthesis and processing conditions restrict the range of their applications. Recently, a number of crosslinked semicrystalline polymers (SCPs) have been found to embody reversible shape-memory effects owing to their broad range of T_m, with crystallites melting at high T_m acting as the skeleton domain and crystallites melting at lower T_m working as the actuation domain. Of the many SCPs that can function as rSMPs,[8-12] poly(ethylene-*co*-vinyl acetate) (EVA) has been investigated most intensely[12] as it has versatile functions,[13] is commercially available, and economically viable. Those rSMPs, termed temperature-memory polymers,[12a,14] have been explored as thermally activated polymer actuators through direct heating/cooling.

Given that optically controlled polymer actuators offer the advantages of remote activation and spatiotemporal control, which can be an asset for certain applications, we herein present a study that demonstrates the effective use of rSMPs as optical actuators through a photothermal effect. This effect has already been introduced to one-way SMPs

as an alternative to direct heating[15] in combination with a variety of light-absorbing and heat-generating nanofillers.[16-20] Of them, gold nanoparticles (AuNPs) are readily prepared, have very high extinction coefficients,[21] and show an extremely strong photothermal effect when illuminated with a wavelength near the surface plasmon resonance (SPR).[22] In this work, to obtain optically controllable SCP-based actuators, AuNPs were surface-functionalized with thiol-substituted EVA, the structure of which was confirmed by FTIR (see the Supporting Information, Figure S1) and ^{1}H NMR spectroscopy (Figure S2), and introduced into EVA to obtain a stable and homogeneous dispersion as revealed by the absorption spectra (Figure S3) and a TEM image (Figure S5) of the nanocomposite. Having been chemically crosslinked and simultaneously hot-pressed into sheets, the nanocomposite can be processed into a desired shape through elongation in the melt, followed by cooling to room temperature under strain.

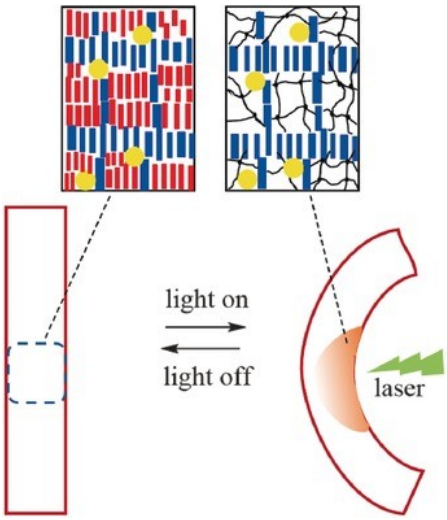

Figure 1. Reversible optical actuation of deformed EVA/AuNP specimen as a result of imbalanced, melting-induced contraction and crystallization-induced expansion forces. Golden spheres are AuNPs; upon visible-light irradiation, their surface plasmon resonance raises the temperature to T_{light}. Blue arrays represent the skeleton domain formed by crystallites of high T_m ($> T_{light}$), red arrays represent the actuation domain formed by crystallites of low T_m ($< T_{light}$), and black lines and dots are the crosslinked amorphous polymer network.

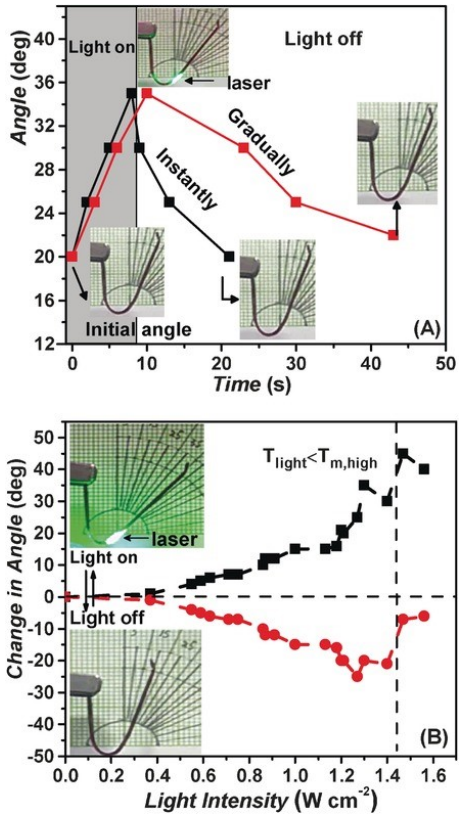

Figure 2. A) Angle change of two separate samples of EVA0.1-0.9 mm-60 % (0.1 wt % AuNPs, original thickness 0.9 mm, and 60 % elongation) upon exposure to a laser (532 nm, 1.13 W cm^{-2}) and subsequently either upon instantaneous turning off the light (fast cooling) or gradual attenuation of the light intensity to zero (slow cooling). B) Angle change (positive for clockwise bending and negative for anticlockwise recovery) as a function of the actinic light intensity for a EVA0.1-0.9 mm-60 % sample; the angle bending was measured after 7 s of light irradiation, and the angle recovery was measured 20 s after turning off the light. Photographs are shown to visualize the reversible optical actuation.

1.3.3 Results and Discussion

On the basis of the thermal actuation principle,[12a] Figure 1 illustrates how reversible optical actuation can work. The broad, approximately 40 °C wide[23] melting temperature range of EVA ($\Delta T_m = T_{m,high} - T_{m,low}$) was found to be hardly affected by the presence of a small amount of AuNPs (Figure S6 and Table S1). When a film of EVA/AuNP was exposed to light of a wavelength near the SPR of the AuNPs, the photothermal effect can locally raise the temperature, denoted as T_{light}. As long as T_{light} is within the melting range,

crystallites with T_m between T_{light} and $T_{m,high}$ form rigid skeleton domains while those with T_m between $T_{m,low}$ and T_{light} constitute the actuation domains. In the light-on state, the crystal melting in the actuation domains induces a contraction force, whereas in the light-off state, the heat release is stopped, and the recrystallization of oriented chain segments upon cooling results in an expansion force. As depicted in Figure 1, photoinduced bending/unbending actuation is expected, which is reminiscent of azobenzene LCE/LCN actuators. As the light intensity decreases with the penetration depth owing to absorption and scattering, the irradiated region is heated to different extents from the surface to the interior, inducing a temperature gradient along the thickness direction as confirmed experimentally (Figure S7). Therefore, the contraction/expansion forces experienced upon switching the light on/off are imbalanced and give rise to bending/unbending. As shown further on, key parameters, such as the photoinduced contraction force, T_{light}, which determines the proportion of actuation domains with respect to the skeleton domains, and the speed for reaching T_{light}, can be readily adjusted. This makes EVA/AuNP a robust optical actuation system with flexible photocontrol over the actuation magnitude and speed at a low AuNP content (0.02 %–0.1 wt %) and relatively weak light intensity (1.13 W cm^{-2}). When an elongated EVA/AuNP strip (original dimension $30\times1.7\times d$ mm^3 with a variable thickness of d = 1.9, 1.2, 0.9, 0.7 or 0.5 mm) is exposed to a laser (λ = 532 nm), it bends towards the actinic light, while upon removal of the light, it is unbent to recover the initial shape (Movies S1 and S2). As a way to quantify the reversible optical actuation, the elongated strip was processed into a U shape, unless otherwise stated. As seen in Figure 2, by fixing one arm and applying the light horizontally to the fold from the outside, the other arm undergoes a clockwise motion and the bent angle increases. Upon turning off the light, the arm can recover the initial angle by doing an anticlockwise motion. We monitored the change in angle by varying a number of parameters that affect the optical actuation speed and magnitude. The results in Figure 2 are a representative example, obtained with EVA0.1-0.9 mm-60 %, a sample containing 0.1 wt % AuNPs with an original thickness of 0.9 mm and final 60 % elongation. In Figure 2 A, two separate U-form specimens were exposed to light (1.13 W cm^{-2}), and it took about 9 s for the angle to increase from 20° to 35°. For one sample, the light was turned off, and the angle went back to the initial state in 13 s. For the other sample, light irradiation was attenuated gradually, and the angle was

recovered more slowly. This result shows that 1) the light-induced deformation is fast and reversible and 2) the recovery speed is governed by the recrystallization kinetics, which can be adjusted optically (Figure S8). Figure 2 B shows the photocontrol of the actuation magnitude by plotting the angle as a function of the actinic light intensity; a positive angle change (clockwise motion) was measured under illumination for 7 s, and a negative angle change (anticlockwise motion) was observed after turning off the light for 20 s. The photocontrol stems from the control of T_{light} by varying the laser intensity (Figure S9). At low intensities below 0.5 W cm^{-2}, no angle change was observed, implying the absence of actuation domains ($T_{light} < T_{m,low}$). From 0.6 W cm^{-2}, the actuation magnitude (angle change) increased with increasing light intensity owing to the increase in T_{light} and thus in the proportion of the actuation domains. Up to 1.14 W cm^{-2}, the positive and negative angles are essentially the same (mirror image), indicating reversible actuation. Above that intensity, the negative angles dropped, meaning that the initial shape can no longer be recovered as all crystallites in the sample are basically melted as $T_{light} > T_{m,high}$. This result shows that the magnitude of the reversible optical actuation can be conveniently controlled by the light intensity. As long as some crystalline skeleton domains are preserved, that is, $T_{light} < T_{m,high}$, the actuation is reversible. Using an intensity of 1.13 W cm^{-2}, the reversible actuation was repeated for 350 cycles with almost the same performance (Figure S10).

The actuation speed is determined by the speed at which T_{light} is achieved upon illumination. In addition to the obvious effect of the light intensity, we carried out experiments to investigate the effect of the AuNP content, specimen thickness, and elongation degree (Figure 3; the actuation was purposely halted at a certain angle change to reveal differences in speed). First, under otherwise identical conditions, a higher AuNP content led to faster bending under irradiation (Figure 3 A). It is easy to picture that with more AuNPs loaded, the temperature increases more rapidly to melt crystallites in the actuation domains, hence resulting in faster motion. After turning off the light, a similar unbending speed was observed, implying similar crystallization kinetics (a bit slower for the sample with the smallest amount of AuNPs). Second, the effect of the specimen thickness was studied (Figure 3 B). The thickest sample, EVA0.1-1.9 mm-60 %, behaved differently. Under irradiation (1.13 W cm^{-2}), its bending is slower than that of thinner samples, and its angle at the light-off state is only about 50 % for the first cycle, as

compared to 75 % for EVA0.1-1.2 mm-60 % and 100 % for EVA0.1-0.5 mm-60 %. For the thinnest sample, data were recorded with a lower light intensity (0.71 W cm^{-2}) because at 1.13 W cm^{-2}, it responded too fast to be monitored. The effect of the thickness is understandable. For a thicker specimen, the fraction of melted crystallites in the surface region over the whole sample is smaller and so is the contraction force that drives the bending motion. Third, with EVA0.1 stretched to different strains but with the same final thickness, the actuation speed increases with increasing the elongation (Figure 3 C). A sample of larger elongation should have more oriented crystallites and the melting that is due to the photothermal effect should result in the release of larger strain energy, leading to a stronger contraction force. The elongation seems to impact the recovery after turning off the light. The unbending is lost at zero elongation owing to a lack of oriented lamella crystallites, while larger elongation favors faster recovery as a result of more rapid crystallization.

Furthermore, we carried out an isostrain experiment to measure the photoinduced contraction force and to determine whether it is consistent with the optical actuation behavior. The experiment on EVA0.1-0.9 mm-60 % is presented in Figure 4. Using a tensile tester, the sample was first equilibrated at 90 °C ($> T_{m,high}$) in the melt and then stretched to 60 % strain before cooling to room temperature. The initial tensile force developed as a result of the elastic extension of chemically crosslinked EVA, and then dropped upon sample cooling owing to the formation of crystallites that freeze in the polymer chains. Interestingly, when the sample was cooled to below 40 °C, the force underwent an upturn, which reflects the continuing reorganization of crystallites in the sample. The remaining force is indicative of the mechanical stress retained in the sample, likely arising from the elastic deformation of amorphous EVA chains. Then, with the sample held under constant strain, light of different intensities was applied. In all cases, once the laser was on, a contraction force developed quickly, but once the laser was turned off, the force dropped. This result confirms that the contraction force results from melting of crystallites in the actuation domains caused by the photothermal effect, and that recrystallization occurs upon cooling upon removal of illumination. Moreover, higher light intensities give rise to a greater photoinduced contraction force, which is in agreement with the observed effect of light intensity on the actuation magnitude and speed.

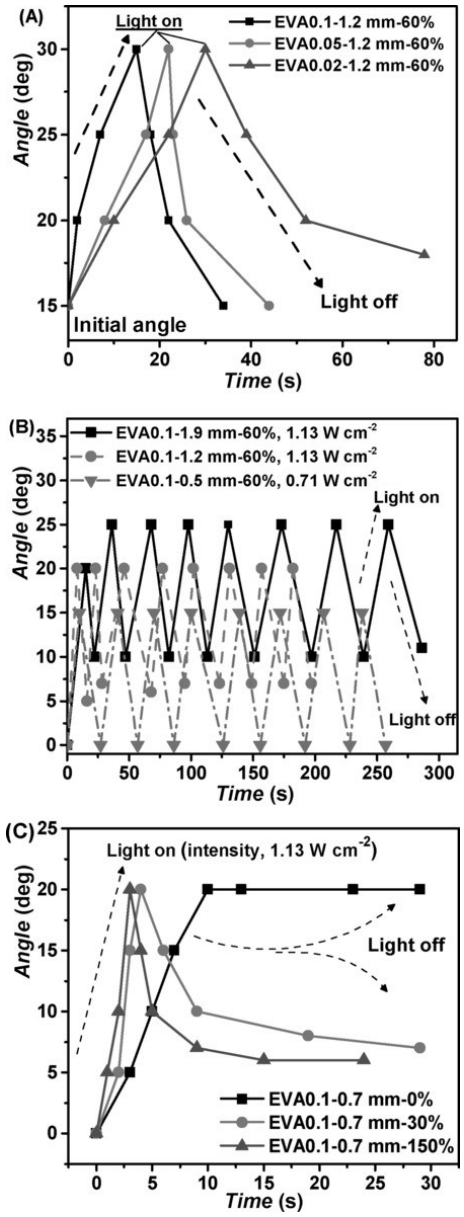

Figure 3. A) Angle variation with time upon light irradiation (1.13 W cm^{-2}) and switching the light off for samples of the same thickness, the same elongation, but different AuNP content. B) Repeated angle bending and recovery cycles for samples of identical elongation but different thickness. C) Angle variation with time for samples stretched to different elongations while having the same final thickness (0.7 mm).

The effect of AuNP content and specimen thickness on the optical actuation is also reflected by the photoinduced contraction force. As seen in Figure 5 A, a comparison of

two samples differing in the AuNP content shows that a larger contraction force is generated under light for the sample containing more AuNPs, especially at low light intensities. Figure 5 B shows the force curves of two samples with different initial thicknesses. With the thinner one, as expected, upon stretching to 60 % strain, the absolute tensile force is smaller than for the thicker sample. The same can be noticed for the photoinduced contraction force. However, the magnitudes of the photoinduced force and the tensile force appear to be similar.

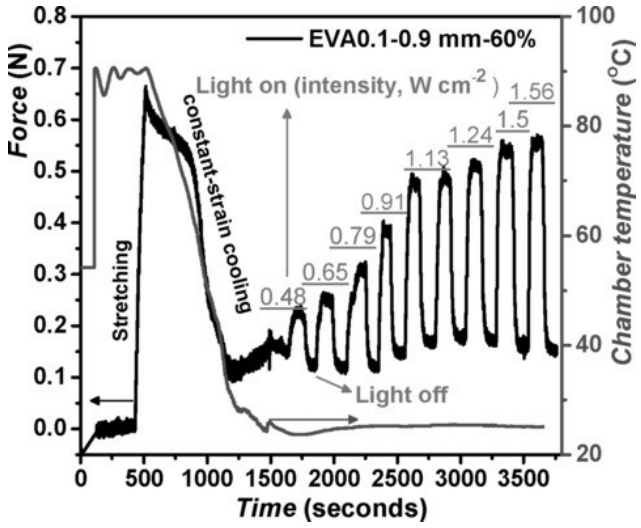

Figure 4. Force curve of an EVA0.1-0.9 mm sample (original dimension: 11.8×1.7×0.9 mm^3) subjected to the following sequence of treatment: heated to 90 °C for equilibrium, stretched to 60 % elongation at a rate of 5 mm min^{-1}, cooled to room temperature at a rate of 5 °C min^{-1} under constant strain, and finally exposed to various light on/off cycles at room temperature with different light intensities as indicated. The temperature profile of the sample chamber is also shown.

The photocontrol of the polymer actuator in terms of both speed and magnitude suggests potential applications in tunable optical actuators. Figure 6 shows an optical switch that can be activated using a laser from a long distance. Here, the electrical connection for a bulb was made (switched on) when the EVA/AuNP actuator underwent an angle increase upon laser exposure, while the disconnection occurred owing to the angle recovery upon removal of the laser from the actuator. The test was realized using a laser

that was 2 m away from the photoelectrical switch (distance limited by vision with the naked eye).

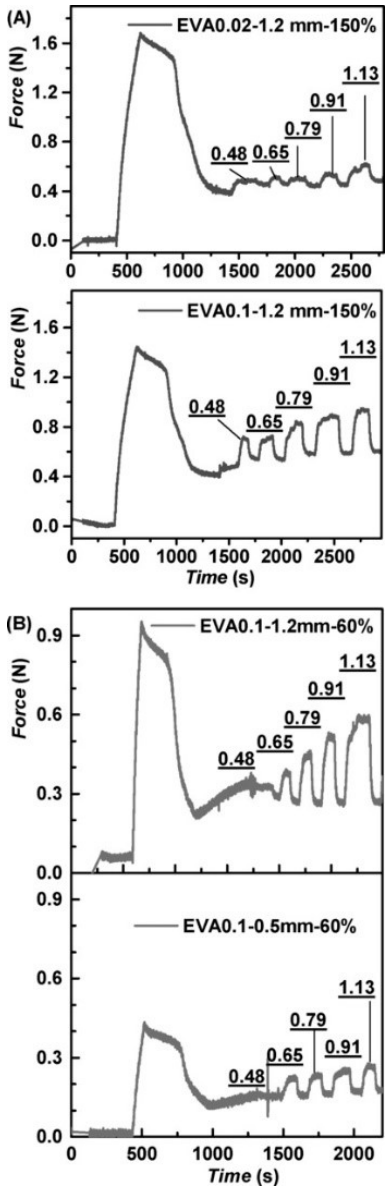

Figure 5. Force curves (stretching at 90 °C followed by cooling to room temperature followed by various light on/off cycles with different light intensities) for A) EVA0.02-1.2 mm-150 % versus EVA0.1-1.2 mm-150 % and B) EVA0.1-1.2 mm-60 % versus EVA0.1-0.5 mm-60 %.

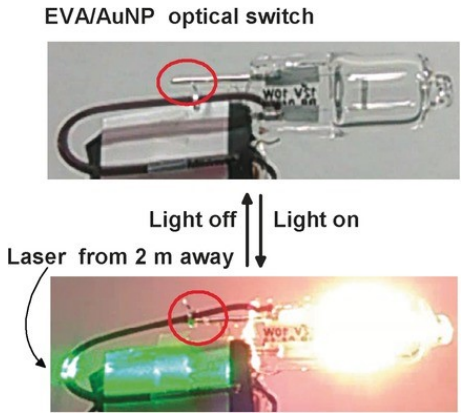

Figure 6. Photographs showing a photoelectrical switch (48 × 1.38 × 0.9 mm^{-3}) made from a stripe of EVA0.1-0.9 mm-60 %. The switch linking the electrode wire from a battery terminal was actuated to connect it with the electrode lead of a bulb to turn the bulb on upon receiving a laser beam emitted from a distance of 2 m, and the disconnection was made by turning off the laser.

1.3.4 Conclusions

In conclusion, we have systematically studied photocontrolled polymer actuators that were obtained by loading crosslinked EVA with a small amount of AuNPs. We have shown that both the actuation magnitude and speed can be tuned by adjusting the laser light intensity, the AuNP content, the specimen thickness, and the elongation degree. Considering the demonstrated advantages of facile, robust, and flexible photocontrol, as well as the fact that the general material design can readily be expanded to other commercially available SCPs in combination with many possible light-absorbing and heat-generating additives, this type of polymer optical actuators is of great interest for further development and exploitation for applications.

Acknowledgements

Y.Z. acknowledges financial support from the Natural Sciences and Engineering Research Council of Canada (NSERC) and le Fonds de recherche du Québec: Nature et technologies (FRQNT). F.G., X.L., and J.X. are grateful to FRQNT and/or the China Scholarship Council (CSC) for scholarships. Y.Z. is a member of the FRQNT-funded Center for Self-

Assembled Chemical Structures (CSACS) and the Centre québécois sur les matériaux fonctionnels (CQMF).

Conflict of interest

The authors declare no conflict of interest.

Keywords: gold nanoparticles · optical actuators · photoresponsive materials · semicrystalline polymers · shape memory

References

[1] a) J. Zhou, S. S. Sheiko, *J. Polym. Sci. B Polym. Phys.* **2016**, *54*, 1365 – 1380; b) H. Meng, G. Li, *J. Mater. Chem. A* **2013**, *1*, 7838–7865.

[2] Q. Zhao, H. J. Qi, T. Xie, *Prog. Polym. Sci.* **2015**, *49–50*, 79–120.

[3] H. Koerner, G. Price, N. A. Pearce, M. Alexander, R. A. Vaia, *Nat. Mater.* **2004**, *3*, 115–120.

[4] a) M. Bao, Q. Zhou, W. Dong, X. Lou, Y. Zhang, *Biomacromolecules* **2013**, *14*, 1971–1979; b) X. Lu, G. Fei, H. Xia, Y. Zhao, *J. Mater. Chem. A* **2014**, *2*, 16051–16060.

[5] a) M. Y. Razzaq, M. Behl, K. Kratz, A. Lendlein, *Adv. Mater.* **2013**, *25*, 5730–5733; b) J. Thévenot, H. Oliveira, O. Sandre, S. Lecommandoux, *Chem. Soc. Rev.* **2013**, *42*, 7099–7116.

[6] a) C. Ohm, C. Serra, R. Zentel, *Adv. Mater.* **2009**, *21*, 4859–4862; b) H. Qin, P. T. Mather, *Macromolecules* **2009**, *42*, 273–280; c) I. A. Rousseau, P. T. Mather, *J. Am. Chem. Soc.* **2003**, *125*, 15300–15301; d) D. L. Thomsen, P. Keller, J. Naciri, R. Pink, H. Jeon, D. Shenoy, B. R. Ratna, *Macromolecules* **2001**, *34*, 5868–5875; e) H. Yu, T. Ikeda, *Adv. Mater.* **2011**, *23*, 2149–2180.

[7] a) M. Yamada, M. Kondo, R. Miyasato, Y. Naka, J.-i. Mamiya, M. Kinoshita, A. Shishido, Y. Yu, C. J. Barrett, T. Ikeda, *J. Mater. Chem.* **2009**, *19*, 60–62; b) Y. Yu, M. Nakano, T. Ikeda, *Nature* **2003**, *425*, 145; c) T. Ikeda, M. Nakano, Y. Yu, O. Tsutsumi,

A. Kanazawa, *Adv. Mater.* **2003**, *15*, 201–205; d) T. Nakai, D. Tanaka, M. Hara, S. Nagano, T. Seki, *Langmuir* **2016**, *32*, 909–914; e) T. Seki, *J. Mater. Chem. C* **2016**, *4*, 7895–7910; f) T. Ikeda, J. Mamiya, Y. Yu, *Angew. Chem. Int. Ed.* **2007**, *46*, 506–528; *Angew. Chem.* **2007**, *119*, 512–535.

[8] a) J. Zotzmann, M. Behl, D. Hofmann, A. Lendlein, *Adv. Mater.* **2010**, *22*, 3424–3429; b) M. Behl, K. Kratz, J. Zotzmann, U. Nochel, A. Lendlein, *Adv. Mater.* **2013**, *25*, 4466–4469.

[9] T. Chung, A. Romo-Uribe, P. T. Mather, *Macromolecules* **2008**, *41*, 184–192.

[10] a) Q. Li, J. Zhou, M. Vatankhah-Varnoosfaderani, D. Nykypanchuk, O. Gang, S. S. Sheiko, *Macromolecules* **2016**, *49*, 1383–1391; b) J. Zhou, S. A. Turner, S. M. Brosnan, Q. Li, J.-M. Y. Carrillo, D. Nykypanchuk, O. Gang, V. S. Ashby, A. V. Dobrynin, S. S. Sheiko, *Macromolecules* **2014**, *47*, 1768–1776.

[11] L. Lu, G. Li, *ACS Appl. Mater. Interfaces* **2016**, *8*, 14812–14823.

[12] a) M. Behl, K. Kratz, U. Noechel, T. Sauter, A. Lendlein, *Proc. Natl. Acad. Sci. USA* **2013**, *110*, 12555–12559; b) J. Li, W. R. Rodgers, T. Xie, *Polymer* **2011**, *52*, 5320–5325.

[13] H. Xu, C. Yu, S. Wang, V. Malyarchuk, T. Xie, J. A. Rogers, *Adv. Funct. Mater.* **2013**, *23*, 3299–3306.

[14] a) K. Kratz, S. A. Madbouly, W. Wagermaier, A. Lendlein, *Adv. Mater.* **2011**, *23*, 4058–4062; b) K. Kratz, U. Voigt, A. Lendlein, *Adv. Funct. Mater.* **2012**, *22*, 3057–3065; c) L. Wang, S. Di, W. Wang, H. Chen, X. Yang, T. Gong, S. Zhou, *Macromolecules* **2014**, *47*, 1828–1836.

[15] D. Habault, H. Zhang, Y. Zhao, *Chem. Soc. Rev.* **2013**, *42*, 7244–7256.

[16] J. Deng, J. Li, P. Chen, X. Fang, X. Sun, Y. Jiang, W. Weng, B. Wang, H. Peng, *J. Am. Chem. Soc.* **2016**, *138*, 225–230.

[17] a) J. Liang, Y. Xu, Y. Huang, L. Zhang, Y. Wang, Y. Ma, F. Li, T. Guo, Y. Chen, *J. Phys. Chem. C* **2009**, *113*, 9921–9927; b) Y. Hu, G. Wu, T. Lan, J. Zhao, Y. Liu, W. Chen, *Adv. Mater.* **2015**, *27*, 7867–7873.

[18] a) H. Zhang, H. Xia, Y. Zhao, *ACS Macro Lett.* **2014**, *3*, 940–943; b) H. Zhang, Y. Zhao, *ACS Appl. Mater. Interfaces* **2013**, *5*, 13069–13075; c) H. Zhang, H. Xia, Y. Zhao, *J. Mater. Chem.* **2012**, *22*, 845–849.

[19] a) Q. Shou, K. Uto, M. Iwanaga, M. Ebara, T. Aoyagi, *Polym. J.* **2014**, *46*, 492–498; b) H. Zhang, J. Zhang, X. Tong, D. Ma, Y. Zhao, *Macromol. Rapid Commun.* **2013**, *34*, 1575–1579.

[20] W. Liu, L.-X. Guo, B.-P. Lin, X.-Q. Zhang, Y. Sun, H. Yang, *Macromolecules* **2016**, *49*, 4023–4030.

[21] X. Liu, M. Atwater, J. Wang, Q. Huo, *Colloids Surf. B* **2007**, *58*, 3–7.

[22] S. Maity, J. R. Bochinski, L. I. Clarke, *Adv. Funct. Mater.* **2012**, *22*, 5259–5270.

[23] a) X. M. Shi, J. Zhang, J. Jin, S. J. Chen, *Express Polym. Lett.* **2008**, *2*, 623–629; b) F. Li, W. Zhu, X. Zhang, C. Zhao, M. Xu, *J. Appl. Polym. Sci.* **1999**, *71*, 1063–1070.

1.3.5 Supporting Information

Experimental Section

Materials

Gold (III) chloride trihydrate, trisodium citrate dihydrate, poly(ethylene-co-vinyl acetate) (EVA, 18 wt.% of vinyl acetate content), dicumyl peroxide (DCP), thioglycolic acid (TGA) were all purchased from Sigma-Aldrich (Canada) and used without further purification unless otherwise noted. EVA was dried in vacuum at 60 ℃ overnight.

Synthesis of Polymer-stabilized AuNPs and Preparation of Samples

Synthesis of Thiol-substituted Polymer Ligand

Thiol-substituted EVA (abbreviated as EVSH) ligand was synthesized referring to reported procedures[s1] involving first hydrolysis and then esterification of EVA. EVA (5.03 g) was dissolved in toluene (50 ml) at 80 ℃ and partially hydrolyzed for 20 min after addition of 8.1 ml of alcoholic sodium hydroxide solution (0.5 mol L^{-1}). To stop the hydrolysis, 6.5 ml HCl (a.q., 1 mol L^{-1}) was added to neutralize the residual alkali. The obtained solution was precipitated into cold methanol. The polymer was recovered by filtration, washing with methanol and drying in vacuum oven at 40 ℃ for 48 h, giving 4.55 g polymer (abbreviated as EVOH) with a yield of 91 %. FT-IR proved the partial hydrolysis of EVA (Figure S1).

EVSH was synthesized via esterification between EVOH (1.006 g) and TGA (0.5 ml, 7.2 mmol) in toluene (15 ml) at 110 ℃ for 24 h under protection of nitrogen. After precipitation into cold methanol, filtration, washing and drying for 48 h in vacuum oven at room temperature, EVSH was obtained (0.90 g, yield of 90 %). Its chemical structure was confirmed by NMR spectrum (Figure S2).

Synthesis of AuNP

Aqueous gold nanoparticles were synthesized according to reference[s2] with modification. In brief, $HAuCl_4 \cdot 3H_2O$ (85 mg, 0.216 mmol) was first dissolved in 180 ml deionized water to form homogeneous aqueous solution. Under magnetic stirring the solution was heated to boiling and instantly added with 20 ml aqueous trisodium citrate dihydrate (195 mg,

0.660 mmol). The mixture was maintained at boiling for 15 min for complete reaction, afterwards cooled to room temperature naturally.

Preparation of Polymer-stabilized AuNP and EVA/AuNP Composite Films

To enable homogeneous dispersion of AuNP in EVA matrix, EVSH was used as ligand to bond to the surface for stabilization of AuNP. EVSH (65 mg) dissolved in tetrahydrofuran (30 ml) was mixed with the previously prepared citrate-stabilized AuNP aqueous solution (30 ml) at 50 ℃ for ligand exchange for 5 min. Hot toluene (50 ℃, 30 ml) was added subsequently to induce phase transfer. The upper layer solution of EVS-AuNP was collected using a separating funnel and ultracentrifuged at 15000 rpm for 15 min to remove unreacted EVA. EVS-AuNP solution of 20 ml (0.106 mg ml^{-1}) was mixed with 10 ml toluene, heated to 80 ℃, added with EVA (2.0 g) and DCP (45 mg) and held (under magnetic stirring) for 15 min step by step. When cooled to 50 ℃ the previous solution was poured into a glass petri dish and allowed to evaporate slowly overnight, after which it was dried in vacuum oven at 40 ℃ for 48 h to form solid composite containing DCP (2.2 wt.%) and EVS-AuNP (0.1 wt.%). The composite was compressed into sheets of different thickness (1.9 mm, 1.2 mm, 0.9 mm, 0.7 mm and 0.5 mm) and crosslinked at 170 ℃, 1.5 MPa for 10 min, 190 ℃, 2.0 MPa for another 10 min and 200 ℃, 3.0 MPa for 25 min, respectively. Films containing different amounts of EVS-AuNP (abbreviated as EVA, EVA0.1, EVA0.05 and EVA0.02, with the number referring to the content of AuNP) were all prepared following the above procedure by adjusting the amount of added EVS-AuNP solution.

Methods and Characterizations

Methods

Optical reversible actuation was quantified by measuring the bending and recovering angle of the programed “U” shape samples with time of light illumination. Specimen with original dimension of 30 × 1.7 × d (d = 1.9 mm, 1.2 mm, 0.9 mm, 0.7 mm or 0.5 mm) were programmed in the chamber oven of Instron (Instron 5965 universal testing system, UK) by stretching at 90 ℃ to different elongations, bending on a U shape metal mold and cooling to room temperature at 5 K min^{-1} for shape fixation. The melting-induced

contraction force upon laser illumination and the force decrease due to recrystallization on cooling after turning off the laser were monitored by Instron with Bluehill 3 software for operational control and data collection.

The laser illumination was performed using a PM-532-2000 laser (Changchun New Industries Optoelectronics Tech. Co., Ltd., China) with wavelength of 532 nm and tunable output power from 0 to 1.2 W. The actual power was determined by a laser power meter (TUNER model, gentec-co company, Canada), based on which the light intensity was calculated by dividing the detected power over the laser spot area (6 mm^2). The angle variation with time upon laser illumination was collected from videos with a graph paper as the background.

Characterization of EVA ligands

Fourier Transform Infrared (FT-IR) absorption spectra were recorded by an IR spectrometer (370 DTGS, Nicolet AVATAR series, Thermo Electron Corporation, USA) with CaF_2 as window. Samples were scanned 32 times in the range of 4000-500 cm^{-1} with a resolution of 4 cm^{-1}. The FT-IR absorption spectra (Figure S1) confirmed successful partial hydrolysis of EVA with peak at 3399 cm^{-1} ascribing to hydroxyl O-H stretching and weak peak at 1740 cm^{-1} ascribing to carbonyl C=O stretching. Nuclear Magnetic Resonance (^{1}H NMR) spectra were obtained from a Bruker spectrometer at 300 MHz, with deuterated chloroform as solvent and tetramethylsilane (TMS) as internal standard (Figure S2). The peaks at around $\delta = 0.88$ are ascribed to H_1 of methyl group at the end of EVA polymer chain and its branches. The strong peaks at $\delta = 1.25$ are attributed to H_2 from the methylene hydrogens of the polyethylene backbone, while the peak at $\delta = 1.55$ arises from the resonance of H_3 from the methylene group of the vinyl acetate part. The weak peaks at around $\delta = 4.89$ are responsible for the methine hydrogens H_4 from vinyl acetate unit. The thiol hydrogen H_a shows triplet at about $\delta = 1.99$, neighboring to which the singlet at $\delta = 2.03$ is ascribed to H_c of the acetate hydrogens. The doublet at $\delta = 3.22$ are assigned to the methylene hydrogens H_b from thioglycolic acid.

Characterization of AuNPs and EVA/AuNP nanocomposites

The surface plasmon resonance (SPR) bands of both AuNP solutions and AuNP-containing EVA/AuNPs composite films were characterized by a UV-Vis spectrophotometer (50 Bio, Varian Australia PTY LTD, Australia). The samples were scanned in the range of 400 nm to 800 nm, in the mode of absorption. As shown in Figure S3, AuNPs in solution showed narrow and strong SPR band at 522 nm before ligand exchange, and 532 nm after ligand exchange. The composite films showed narrow and strong SPR band at 532 nm, which coincided with the wavelength of actinic laser. The fact that the SPR band of AuNPs for films is very similar to that of AuNPs homogeneously dispersed in solution indicates the excellent dispersion of the nanoparticles in the nanocomposite, because any significant aggregation of AuNPs in films will result in broadening and red-shift of the SPR band.

Thermogravimetric Analysis (TGA) was performed to measure the weight fraction of AuNPs and ligand on a thermogravimetric analyzer from 25 ℃ to 700 ℃ at 10 K min^{-1} under argon flow of 50 ml min^{-1}. 13.82 mg EVS-AuNPs was used for the measurement. The result showed the weight fraction of ligands to be 0.619 (Figure S4).

EVA0.1 sample was frozen-sectioned and subject to Transmission Electron Microscopy (TEM, HITACHI H-7500) operated at 80 KV for observation of the dispersion of AuNPs in the EVA matrix, and measurement of the size of AuNPs. A total of 300 particles were analyzed (by AMT Image Capture Engine Software) to obtain the average diameter of AuNPs, which was calculated to be 15 nm. As can be seen in Figure S5, the AuNPs were dispersed well in the EVA matrix.

The degree of functionalization (grafting density, chains nm^{-2}) of AuNPs was calculated by combing the results of TGA and TEM referring to literature.[s3] Grafting density $g_d = N_A L d / M_n$, where N_A is Avogadro's constant, 6.02×10^{23}, L is the thickness of the ligand on the gold surface, d is the bulk density of the ligand (assumed to be the same with EVA), 0.94 g cm^{-3}, and M_n is the number average molecular weight of EVA18, 25000 g mol^{-1} as reported.[s4] The calculated graft density of 1.16 chains nm^{-2} was obtained.

The melting and crystallization temperatures as well as the degree of crystallinity of the crosslinked samples were characterized by Differential Scanning Calorimeter (DSC, TA Q200, USA). Three scans with the first heating from 25 ℃ to 100 ℃ at 10 K min^{-1}, the

first cooling from 100 °C to 0 °C at 5 K min^{-1} and the second heating at 5 K min^{-1} from 0 °C to 100 °C were performed under nitrogen flow. The degree of crystallinity is calculated by $X_c = (\Delta H_m / \varphi \Delta H^*_m) \times 100\%$,

where φ is the weight fraction of EVA in the composite, ΔH_m is the enthalpy of fusion of the sample and ΔH^*_m is the enthalpy of fusion of perfect polyethylene crystal with 100 % crystallinity, 277.1 J g^{-1} based on literature[s5].

Evaluation of light-induced temperature gradient along the thickness direction

To obtain experimental evidence of photoinduced temperature gradient along the specimen thickness direction, the probe of a traceable expanded-range thermometer (Fisher Scientific) was coated with films of different thicknesses d (d ± 0.07 mm) of the nanocomposite EVA0.1 (uncrosslinked for good adhesion). Immediately after exposing the outer side of film to the laser (1.13 W cm^{-2}) for 10 seconds, the temperature underneath the laser spot was measured. The obtained temperature decreased with the film thickness, providing evidence of the temperature gradient (Figure S7).

Supporting Figures and Tables

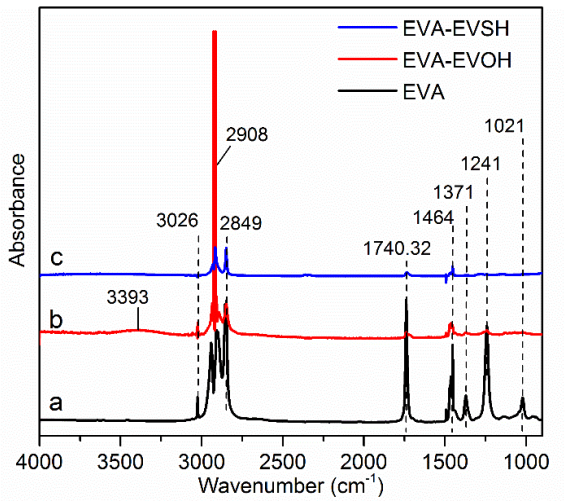

Figure S1. FT-IR absorption spectra of EVA (a), partially hydrolyzed EVA (b) and thiol-substituted EVA (c).

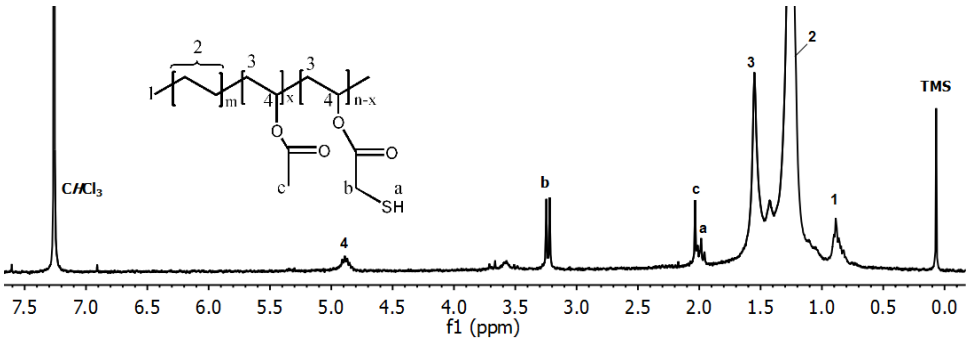

Figure S2. ^{1}H NMR spectrum of EVSH ligand.

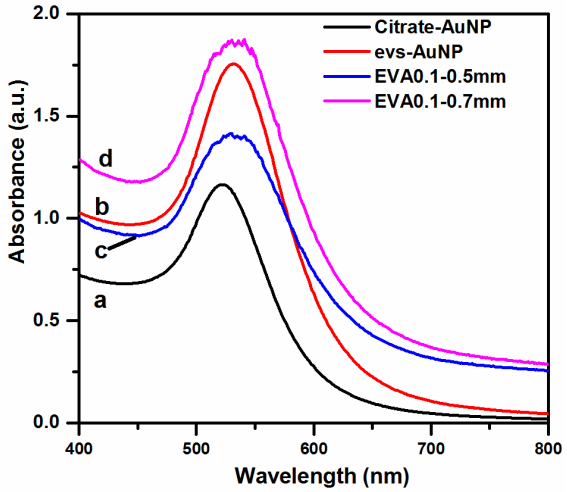

Figure S3. Visible light absorption spectra of (a) Citrate-stabilized AuNP aqueous solution (5×10^{-5} g ml^{-1}), (b) EVS-AuNP solution in toluene (1×10^{-4} g ml^{-1}), (c) EVA0.1 sheet with thickness of 0.5 mm and (d) EVA0.1 with thickness of 0.7 mm.

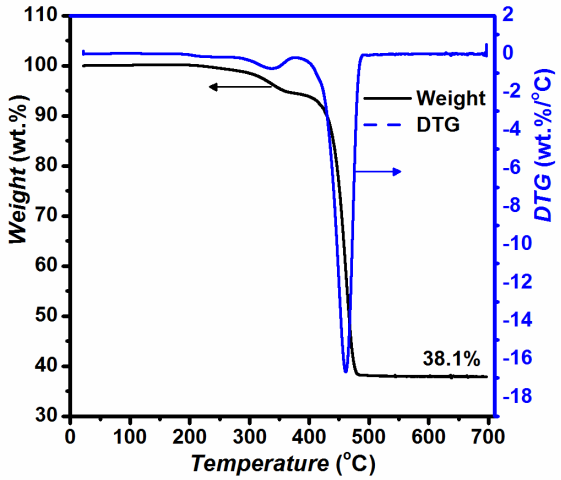

Figure S4. TGA and DTG curves for EVA-functionalized AuNPs.

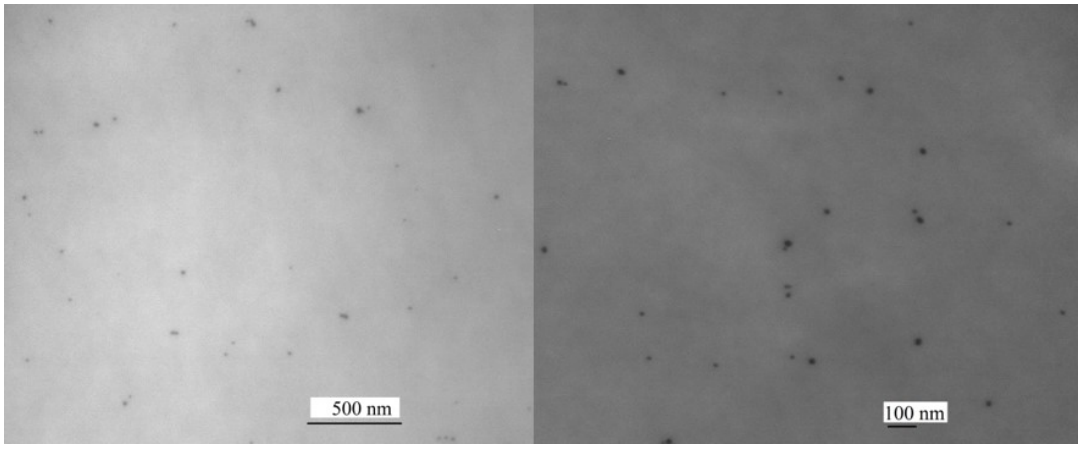

Figure S5. TEM images of EVSH-stabilized AuNPs dispersed in EVA matrix. The scale bar in the left image is 500 nm and 100 nm in the right.

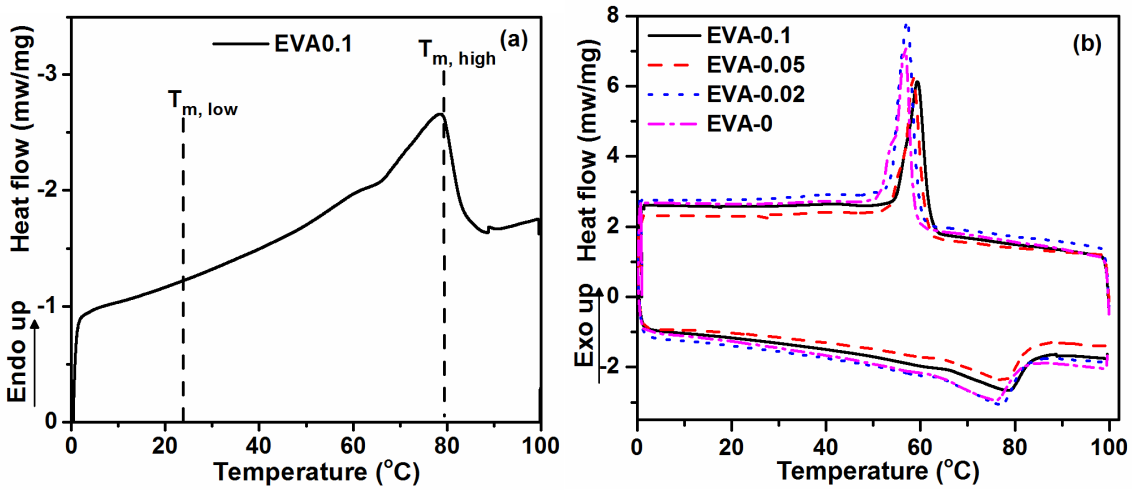

Figure S6. DSC second heating curve of sample EVA0.1 (a) and second heating and cooling curves for all samples containing different amounts of AuNPs (b).

Table S1 Thermal Properties of EVA/AuNP composites obtained from DSC.

Sample	T_c [a] (°C)	T_m [b] (°C)	ΔH_c [c] (J g^{-1})	ΔH_m [c] (J g^{-1})	X_c [d] (%)
EVA-0	57.2	76.4	38.93	-46.86	16.9
EVA-0.02	57.2	77.0	40.70	-53.43	19.3
EVA-0.05	58.5	77.6	34.97	-46.17	16.7
EVA-0.1	59.4	78.5	34.95	-43.45	15.7

[a] T_c is the cold crystallization temperature. [b] T_m is the peak melting temperature during the second heating cycle. [c] ΔH_c and ΔH_m are the enthalpy of crystallization and the enthalpy of melting, respectively, during the second heating scan. [d] X_c is the crystallinity obtained from the second heating.

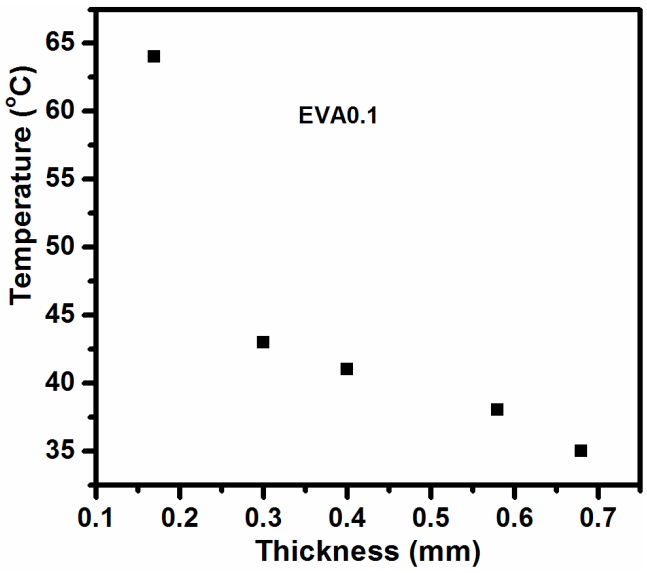

Figure S7. Temperature variation over varying thickness of an EVA0.1 sample (detected by thermocouple after 10 seconds of laser irradiation, light intensity 1.13 W cm^{-2}), showing evidence of a temperature gradient along the thickness direction.

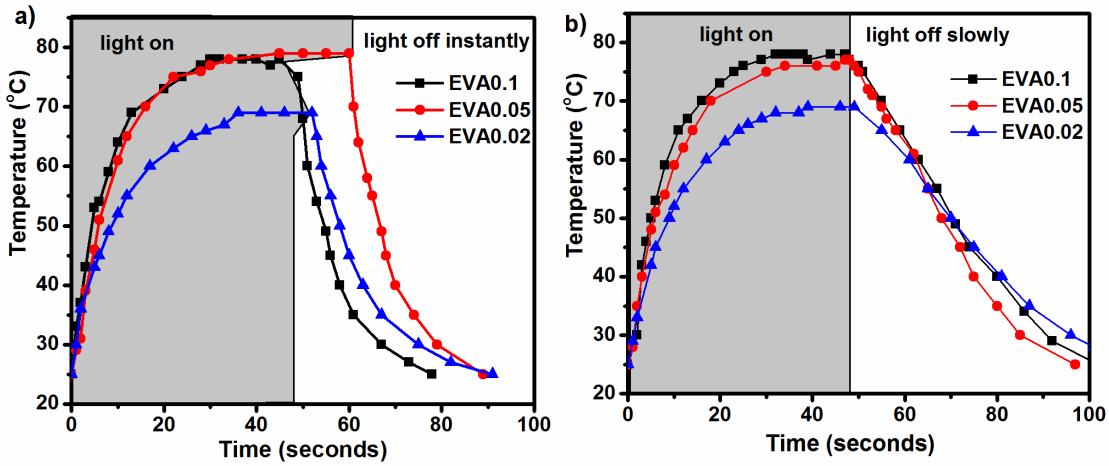

Figure S8. Temperature variation with time for samples containing different amounts of AuNPs upon laser illumination (intensity of 1.13 W cm^{-2}) and upon intensity decrease at different speeds, a) laser turned off instantly; b) laser turned off slowly at 0.1 W s^{-1}. The probe of the thermometer was coated with uncrosslinked EVA/AuNP nanocomposite with thickness of 0.17 ± 0.06 mm, at which the maximum steady temperature was detected.

It is shown in Figure S8 that the temperature of the composites containing more AuNPs was raised faster. When the light was turned off instantaneously (a), the temperature was

decreased fast; but when the light was turned off slowly (b) by decreasing the power at a rate of 0.1 W s^{-1}, the temperature was decreased slowly. The crystallization kinetic can be controlled in such a way that the speed of recovery of the actuator can also be adjusted.

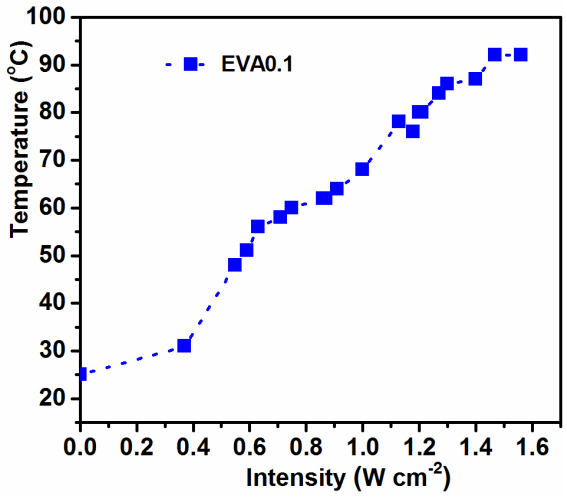

Figure S9. Variation of the maximum temperature reached in the sample EVA0.1 with laser intensity. For temperature measurement, uncross-linked EVA0.1 was melted and coated on the probe of the thermometer as in Figure S8.

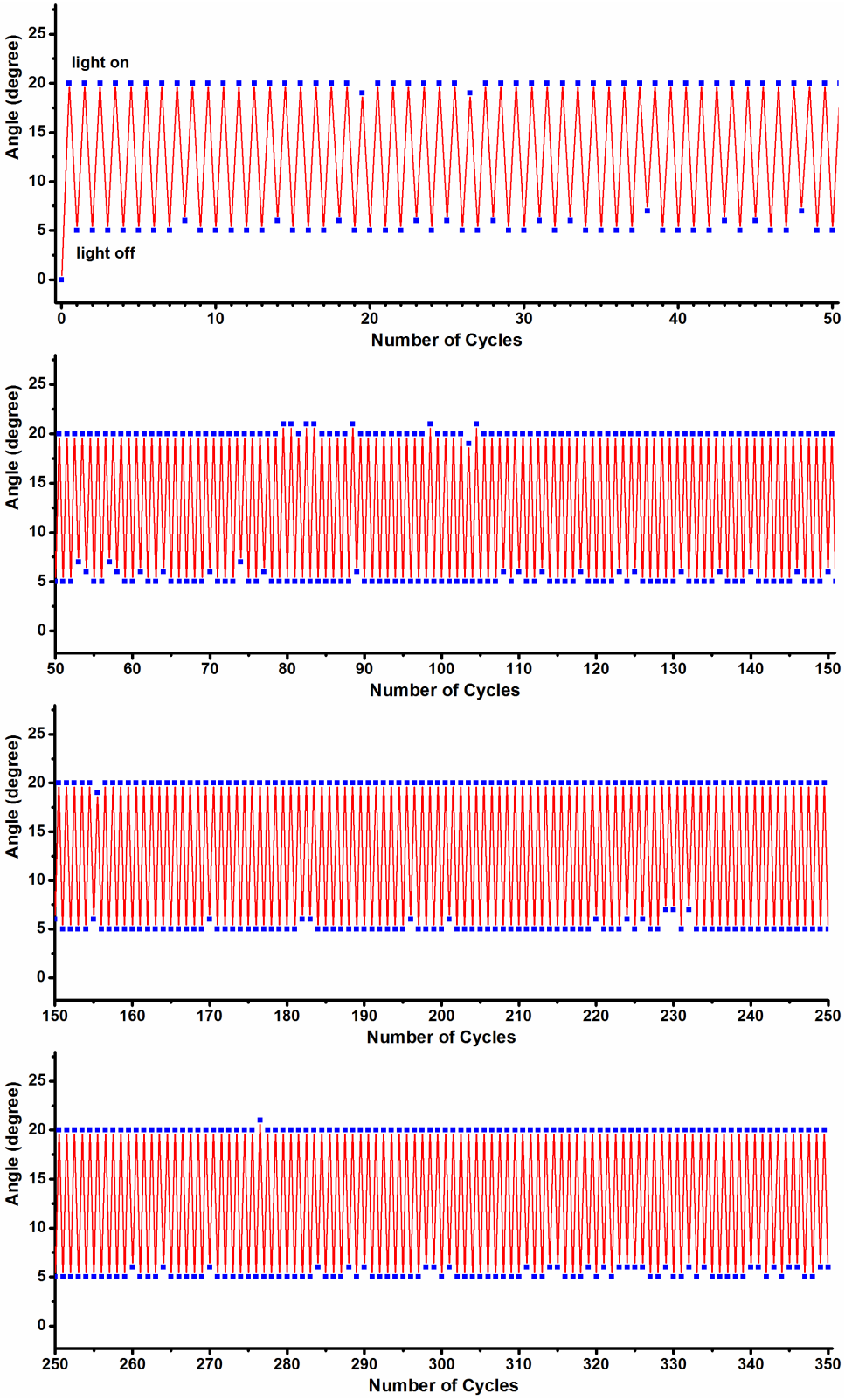

Figure S10. Reversible bending and unbending actuation over 350 cycles for a sample of EVA0.1-0.9 mm-100 % subjected to laser (intensity of 1.13 W cm^{-2}).

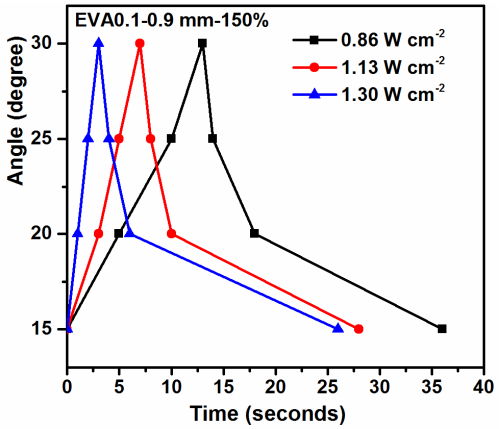

Figure S11. Angle variation with time for the same sample triggered by different light intensity.

Supporting Movies

Movie S1

Movie S2

Movie S1 and Movie S2 (speed ×8): in Movie S1 the sample had an initial thickness of 0.5 mm and the laser intensity was 0.7 W cm^{-2}, while in Movie S2, the sample thickness was 0.9 mm and the laser intensity 1.13 W cm^{-2}.

Supporting References

[s1] a) Y. Hirata, S. Marais, Q. T. Nguyen, C. Cabot, J.-P. Sauvage, *J. Membrane Sci.* **2005,** *256*, 7–17; b) M. Tang, J. Hou, L. Lei, X. Liu, S. Guo, Z. Wang, K. Chen, *Int. J. Pharm.* **2010**, *400*, 66–73; c) R. V. Barbosa, B. G. Soares, A. S. Gomes, *J. Appl. Polym. Sci.* **1993**, *47*, 1411–1418.

[s2] G. Frens, Z. Kolloid, *Nat. Phys. Sci.* **1973**, *241*, 20–22.

[s3] X. Jia, X. Jiang, R. Liu, J. Yin, *Chem. Commun.* **2011**, *47*, 1276–1278.

[s4] J. Kalish, Ph.D. Thesis, University of Massachusetts Amherst, Amherst, 2011.

[s5] J. Brandrup, E. H. Immergut, E. A. Grulke, *Polymer handbook 4th edition*. Wiley-Interscience Publication, New York (**1999**).

1.4 Summary of the Project

In this work, we demonstrated a robust photoactuator based on oriented and crosslinked semicrystalline EVA polymer containing a small amount of dispersed AuNPs, and studied several factors that impact the reversible optical actuation. The synthesized AuNPs were stably dispersed and compatible within the matrix, as confirmed by UV-Vis spectrometry, TGA and TEM analysis. The photothermal effect of the composites, monitored by a thermocouple, was strong and tunable by varying the AuNPs content and the laser intensity. The actuators were programmed by stretching crosslinked EVA in melted state followed by cooling under strain to RT. The formed crystallites with a broad T_m range could be partially melted at T_{light} upon laser irradiation, with the melted crystallites as the actuation domain and the rest as the skeleton domain. Due to light scattering and restriction on the light penetration depth, a temperature gradient was generated across the thickness and drove the actuator to bend toward the light source and unbend upon turning off the light. The actuation magnitude increased with T_{light}, which increased with laser intensity and the content of AuNPs. Both the actuation and recovery speeds could be tuned by the power of the laser; the faster T_{light} was reached, the more rapid the actuation speed was. Interestingly, the recovery speed of the actuator could be slowed down and controlled to some extent by reducing the laser power slowly. It was also found that larger elongation caused faster actuation while larger thickness decreased the actuation speed and weakened the recovery degree. With our optimized actuator in "U" shape, more than 350 cycles of reversible laser-driven bending/unbending were achieved with no notable decay. This work opens the window for the design and manufacture of optical actuators with commercialized SCPs and application of these optical actuators for light-to-mechanical energy conversion.

CHAPTER 2 A NEW FUNCTION FOR THERMAL PHASE TRANSITION-BASED POLYMER ACTUATORS: AUTONOMOUS MOTION ON A SURFACE OF CONSTANT TEMPERATURE

2.1 About the Project

The reversible actuation of polymer actuators typically requires repetitive on/off switching of the used external stimulus for multiple cycles of actuation and rapid switching for a continuous energy conversion process. In fact, many important motions are autonomous and self-sustained, i.e. the movements proceed continuously without external intervention. Examples of such actuations include hearbeat, beating of wings, rotation of windmills and motors. Using polymer actuators to mimick these autonomous and continuous motions by on/off control of external stimuli is operose and inefficient. We have shown in Chapter 1 that EVA/AuNP composite photoactuators bend toward the light source on irradiation owing to the generation of photothermal temperature gradient across the thickness. When the irradiaiton is removed, spontaneous unbending takes place arising from directed crystallization. Inspired by this reversible bending/unbending actuation accompanied by a temperature gradient, in the present work we have established, for the first time, an intelligent system capable of continuous motion with the only need of placing a solid polymer strip on a substrate of constant temperature T_{surf}. We use the crosslinked secmicrystalline EVA to prepare the autonomous actuator which contains aligned crystallites. The programmed strip is placed on a substrate at T_{surf} which is lower than the highest T_m of EVA. The strip bends to form an arch shape instantly upon touching the hot substrate, induced by the temperature gradient, and then flattens back on the substrate, which heats the strip again to bend it up and resume the cycle. We put forward the thermo-mechano-thermal feedback loop concept to explain well the autonomous up-and-down oscillation. Several parameters are varied to disclose their effects on the self-sustained oscillation. We demonstrate examples that show how the EVA actuators can directly convert themal energy to mechanical energy. This finding based on thermal phase transition of SCPs is unprecedented and can be extended to many other materials for energy conversion.

2.2 Contributions

This work was published in *Chemical Science*, **2017**, *8*, 6307 by Feijie Ge and Yue Zhao. I conducted the study in Université de Sherbrooke under the supervision of Prof. Yue Zhao. I designed the experiments with Prof. Zhao. All the experiments and most of the characterizations were ascribed to my work. Specifically, I prepared all the materials and samples, and carried out all the autonomous motion tests and thermomechanical force tests. I collected all the data, plotted them into figures and tables. Prof. Zhao and I analysed the data, and I wrote the first version of the manuscript. Prof. Zhao revised and finalized the manuscript.

2.3 Paper Published in Chem. Sci. 2017, 8, 6307. Reproduced with permission from the Royal Society of Chemistry.

A new function for thermal phase transition-based polymer actuators: autonomous motion on a surface of constant temperature

Feijie Ge and Yue Zhao*

Département de Chimie, Université de Sherbrooke, Sherbrooke, Québec, J1K 2R1, Canada.
E-mail: yue.zhao@usherbrooke.ca

2.3.1 Abstract

It is very challenging to make materials capable of autonomous oscillation known in many living systems (such as the heartbeat). Herein, we describe an approach to creating a thermo-mechano-thermal feedback loop for thermal phase transition-based polymer actuators, which leads to hour-long, autonomous motion on a substrate surface of constant temperature. We investigated the variables that determine the amplitude and period of the motion, and demonstrated exemplary physical works powered by direct thermomechanical energy conversion. Such continuous motion of a solid polymer driven by thermal energy without the need for temperature up/down switching is unprecedented, and the validated feedback loop can be implemented into other thermal phase transition-based polymer actuators.

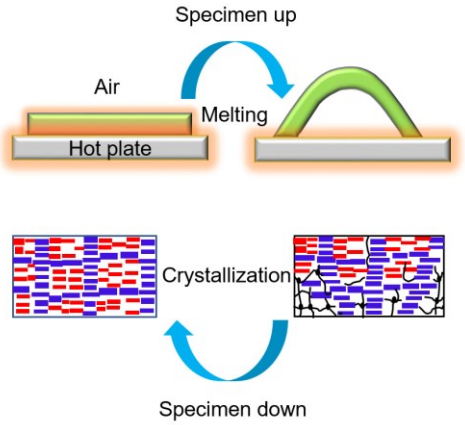

2.3.2 Introduction

Polymers that are responsive to diverse stimuli have been continuously exploited for application as soft actuators in the past few decades.[1] But a major challenge arises when it comes to autonomous actuators that, like in living systems (e.g., heartbeat), can undergo continuous, self-sustained oscillating motions with no need for on/off switching of external stimuli, i.e., without external intervention. The rare systems capable of autonomous actuation are mainly stimuli-responsive polymer brushes[2] and hydrogels under the effect of an oscillating reaction[3] or a water-gradient,[4] and photoresponsive polymers based on photothermal effect[5] or photoisomerization reactions.[6] In the latter case, liquid crystal networks (LCNs) bearing azobenzene moieties are the most developed, for which the reversible *trans–cis* photoisomerization of azobenzene is at the origin of either rotation under synchronized irradiation with two separate beams of UV and visible light,[7] oscillation of a cantilever under one focused light beam[8] or chaotic oscillation driven by sunlight.[9] Other examples of autonomous actuators are powered by triggered depolymerization reactions[10] or catalytic decomposition[11]. Of particular note is a hydrogel-based microstructure developed by Aizenberg's group,[12] which is capable of self-sustained oscillation between two liquid layers, driven by a chemo-mechano-chemical feedback loop. The key to achieving autonomous actuation under unchanged or "constant" stimulation is a feedback loop. Besides the aforementioned systems, thermally fuelling a solid polymer actuator for continuous motion has not been realised thus far. Herein, we demonstrate a strategy for creating a thermo-mechano-thermal feedback loop that allows a solid polymer to undergo continuous, self-powered actuation with the only requirement being exposure to a substrate surface of constant temperature. We also investigated the factors that determine the amplitude and period of the thermally driven oscillating motion.

Our envisioned thermo-mechano-thermal feedback loop can be depicted as follows (Fig. 1a). When the lower-side of a polymer strip with oriented chains touches the substrate surface, should a temperature gradient be quickly established, the polymer may undergo a phase transition (e.g., melting) mainly in the lower surface region to give rise to an imbalanced longitudinal contractile force that pushes the middle section of the strip upward to form an arch. Once in the air, as the lower side of the strip cools down, the reverse phase

transition occurs, resulting in an extensional force that brings the deformed strip back to the flat shape and, by doing so, makes the lower side touch the surface again to renew the motion cycle. To validate this design and the related mechanism, we chose to use a crosslinked semicrystalline random copolymer poly(ethylene-*co*-vinyl acetate) (EVA) that, as reported by Lendlein and coworkers[13,14], is a thermal polymer actuator displaying a two-way shape memory, or temperature-memory, effect. The melting temperature T_m of EVA spans over a wide range of about 40 °C, between $T_{m,low}$ and $T_{m,high}$. After elongating a specimen in the melt ($T > T_{m,high}$), cooling it under strain induces crystallization of the oriented polymer chains and allows the elongated shape to be frozen at room temperature below $T_{m,low}$. After this programming phase, by heating the elongated specimen to a temperature T^* within the melting range ($T_{m,low} < T^* < T_{m,high}$), crystallites with $T_m < T^*$ melt in the actuation domains, while those with $T_m > T^*$ remain and form a rigid skeleton, resulting in a contraction force that shrinks the specimen along the elongation direction. On subsequent cooling, oriented chain segments in the actuation domains recrystallize under the constraints of the crystalline skeleton, giving rise to an expansion force that elongates the specimen to the initial shape. Therefore, reversible thermal actuation (shrinkage/extension) is achieved by switching the temperature up and down. In a previous study,[15] we transformed this thermal actuator onto an optical actuator by loading a small amount of gold nanoparticles (AuNPs) in EVA, and used the photothermal effect arising from the surface plasmon resonance (SPR) of the nanofiller to realise the on-off switching of temperature through on–off switching of light. It was found that with one side of the specimen exposed to light, a temperature gradient could be formed due to attenuation of light absorption along the thickness direction, leading to reversible bending/unbending upon light on/off respectively. Inspired by this finding, it could be foreseen that when a specimen sufficiently thick is in contact with a hot substrate surface, a temperature gradient could be formed due to heat diffusion along the thickness direction, which leads to a superficial melting-induced contractile force that pushes the specimen up and, once cooled in the air, yields a crystallization-induced extensional force that flattens the specimen on the substrate surface to reactivate the motion cycle. Therefore, EVA was utilised in the present study to investigate the thermally driven autonomous motion under the envisioned thermo-mechano-thermal feedback loop. Before discussing the results, it should be

emphasized that the reversible actuation mechanism of EVA was reported in ref.13, while the present study is about a mechanism of autonomous motion by introducing the feedback loop. In ref.13, all actuations were achieved by externally heating and cooling the polymer repeatedly, whereas in what follows, we show fast actuations self-sustained on a surface of constant temperature, without external intervention of switching the temperature up and down.

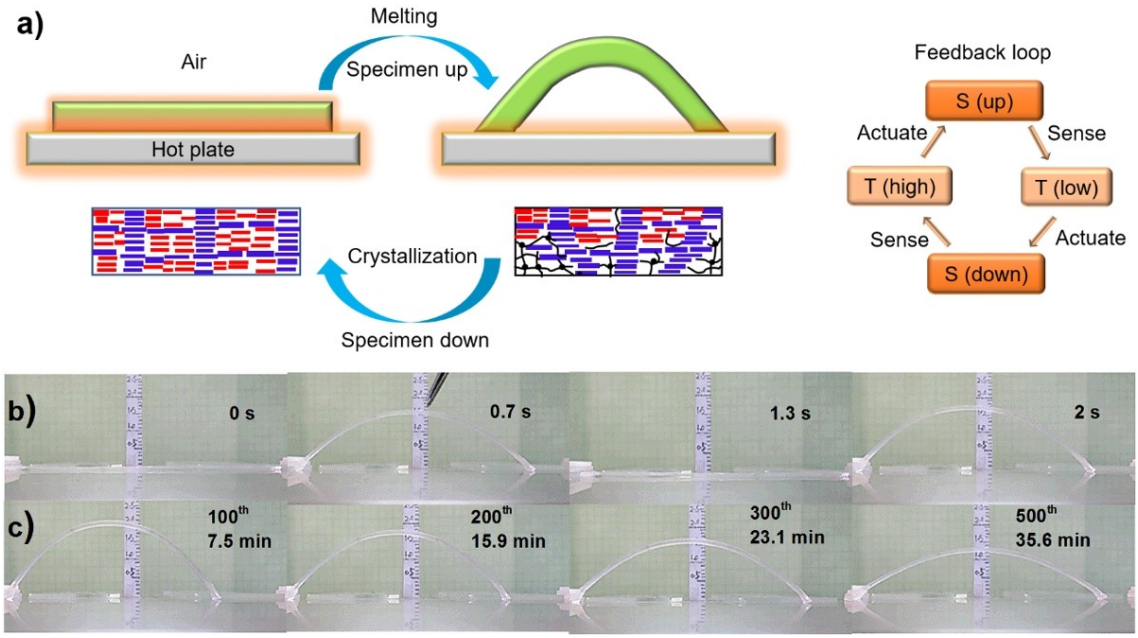

Fig. 1. Autonomous actuation. (a) Schematic for melting-induced superficial contraction making the specimen arch up and the crystallization-induced superficial extension bringing the specimen down, which goes on in a continuous and self-powered manner due to a thermo-mechano-thermal feedback loop (S: sample, T: temperature); the blue arrays and red arrays represent polymer crystallites with high T_m and low T_m, respectively, while the black lines and dots represent the amorphous polymer chains and crosslinks, respectively. (b) Snapshots showing the first two jumps of an EVA specimen (100 % elongation, 65 × 3 × 0.6 mm^3) placed on the surface of a steel plate at T_{surf} = 84 °C. (c) Snapshots showing the actuation amplitude of the same specimen after hundreds of jump/descent movements (the number of cycles and the corresponding actuation times are indicated).

2.3.3 Results and discussion

Autonomous, continuous motion was indeed achieved (Fig. 1b and c, Movie S1). To prepare the specimen of EVA used, a strip of initial length of 35 mm (4.3 mm in width and 0.9 mm in thickness) was stretched at 90 ℃ to a length of 75 mm, followed by cooling under a constant strain to room temperature for shape fixation. Prior to the actuation test, the elongated strip was heated on the hot surface of a steel plate (T_{surf} = 75 ℃) to purposely shrink it to 65 mm (remaining strain 100 %, see Methods in ESI) to release part of the entropic elastic strain energy that, if overpowering the internal stress arising from the volume change associated with melting and crystallization, can cause irreversible contraction. This programming phase resulted in the test specimen denoted as 0.6 mm-100 %, i.e., 100 % elongation and 0.6 mm in thickness (all specimens were prepared to have the same length of 65 mm and width of 3 mm). It was then placed on the substrate surface (T_{surf} = 84 ℃) located in a hood with air flow velocity of 160 ± 5 feet per min, and the autonomous actuation was recorded by a camera from which frame-by-frame analysis (photos or data) could be conducted. As is seen in Fig. 1, once in contact with the hot surface, the middle of the strip jumped up in the air to form an arch, which is a clear manifestation of an inward contractile force acting on the bottom layers of the specimen due to the melting of crystallites. Shortly after, the strip went down to flatten on the surface, which indicates an extensional force acting on the same side of the specimen as a result of the recrystallization of oriented chain segments in the air. This oscillating motion then went on continuously in a self-sustained and self-powered manner, fuelled only by thermal energy provided by the hot surface. The first two jumps occurred within 2 seconds (Fig. 1b). Although the height of arch decreased over time, it remained substantial even after 500 cycles over 35 min of actuation (Fig. 1c). Therefore, giving a substrate surface as a heat source and air flow above, a thermo-mechano-thermal feedback loop is established and governs the actuation of the polymer from sensing high temperature (melting) to jumping up (motion) to sensing low temperature (crystallization) to falling down (motion). The expected temperature variation of the strip during the jump/descent cycles on the substrate surface was observable with an infrared camera (Fig. S1). In principle, this autonomous actuation would go on perpetually if the melting/crystallization generates the

same superficial contraction/extension force in every cycle. In practice, as will be discussed further on, "imperfections" may prevent this from happening.

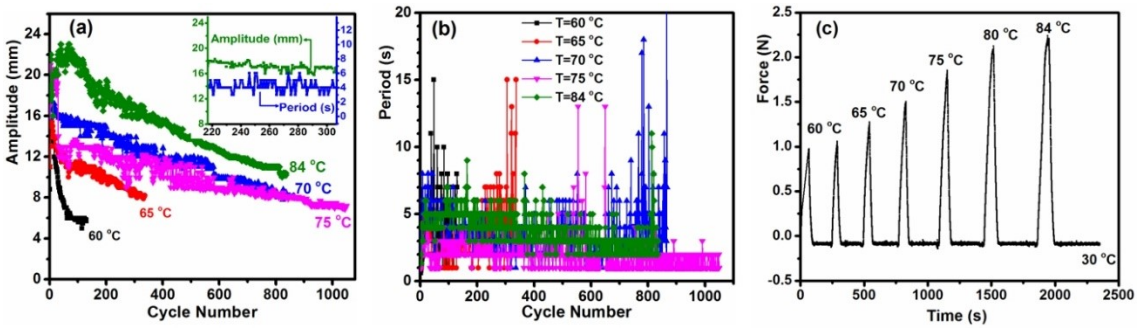

Fig. 2. Effect of substrate surface temperature. (a) and (b) Variation of actuation amplitude (in mm) and period (in seconds), respectively, with the number of jump/descent cycles for specimen 0.6 mm-100 % placed on substrate surface set at different temperatures. The inset in (a) (T_{surf} = 84 °C) shows the relatively steady state for both amplitude and period over certain actuation time period. (c) Contractile force for the specimen 0.6 mm-100 % heated to different temperatures in the isostrain experiment. Before being heated to a given temperature, the sample under constant strain was cooled to 30 °C.

We investigated the effect of three key parameters on the autonomous actuation by measuring the motion amplitude, defined as the height of elevation, and the period, defined as the time for completing one cycle of jump and descent. They are the substrate surface temperature T_{surf}, specimen elongation and thickness. Intuitively, both the actuation amplitude and period should be related to the superficial contraction force that pushes the specimen upward at a certain speed. Therefore, to get more insight into the role played by each variable, we also utilised the isostrain experiment to measure the contraction force developed in the specimen under constant strain while undergoing partial melting of crystallites. Since the jumping sample in air was previously heated during contact with the substrate, its body temperature is higher than that of the air and decreases with time before touching the substrate again. This ensures that the crystallization-induced expansion happens during the non-isothermal process. Although such measured force is generated by the whole sample, the data reveal the effect of a given parameter on the superficial contraction force. First, the substrate surface temperature obviously is important, because

it influences the number of crystallites to be melted, which, in turn, determines the contraction force. The results obtained at various T_{surf} values show clear trends. Overall, as compared to the relatively low T_{surf} of 60 and 65 ℃, higher temperatures of 70, 75 and 84 ℃ led to larger amplitudes during the whole process, longer duration (from 35 to 52 min) and more cycles (from 800 to1000) (Fig. 2a). However, the larger amplitude apparently resulted in longer period, which is particularly evident by comparing the data at 84 and 75 ℃ (Fig. 2b). As for the contraction force, it increased with increasing temperature (Fig. 2c), which is no surprise because a higher temperature increases the number of melted crystallites and thus the proportion of the actuation domains in the specimen. It becomes clear that the actuation amplitude is essentially determined by the contraction force, which, at T_{surf} below 60 ℃, is not strong enough to drive the actuation. The effect on the period is more complex. Even though a larger amplitude pushes the arch further from the hot surface, a higher T_{surf} makes the air above warmer, which may actually slow down the crystallization speed. In the end, the period is mainly affected by the time required for the arch to return to the flat state (Movie S1), which is determined by how fast the crystallization can generate a sufficient extensional force to drive the motion. Finally, some features of the autonomous actuation can be noticed on closer inspection of the data at 84 ℃. At the early stage (within about the first 80 cycles), the amplitude increased to a maximum (23 mm) before going down, displaying large fluctuations. Then, with the amplitude decreasing gradually over time, the actuation appeared to enter a relatively steady state in both amplitude and period, as can be seen from the inset (in Fig. 2a) showing the changes over about 100 cycles. The period decreased with the decreasing amplitude before rising sharply after a total of more than 800 cycles, signalling the end of actuation.

When two specimens of the same dimension but different elongation degrees were subjected to the autonomous actuation at T_{surf} = 75 ℃, they behaved differently in both amplitude (Fig. 3a) and period (Fig. 3b). The one with a larger elongation (200 %) showed a higher jumping amplitude and shorter period than the one with a smaller elongation (100 %). The reason can be found from the contraction force (Fig. 3c). The force generated in the specimen with 200 % elongation is much stronger than that in the specimen with 100 % elongation. Indeed, the elongation degree determines the amount of strain energy stored in a sample. Upon melting of crystallites in the actuation domains, more strain

energy is released from relaxation of more oriented chains in the amorphous region, thus generating a greater contraction force to make the specimen jump faster and to a larger magnitude. For the return to flat state, since T_{surf} is the same, meaning the same temperature gradient in the air above the surface is present, a larger amplitude allows the specimen to crystallize more quickly in the colder air and flattens the arch faster. This explains the shorter period observed for the specimen with 200 % elongation. However, the faster autonomous actuation appeared to be accompanied by larger fluctuations in amplitude and a shorter duration. A likely explanation is that at this large elongation, the melting-induced contraction has a more important contribution from the release of entropic elastic strain energy, so that the subsequent crystallization could not induce an elongation that matches the contraction. As the actuation goes on, the extent of irreversible contraction of the lower side of the specimen increases, creating a curvature that, at some point in the process, prevents the specimen from touching the hot surface firmly and basically puts an end to the actuation. Likewise, the specimen thickness also influences the autonomous actuation (see Fig. S2 and the related discussion in the ESI). Although the achieved hour-long, autonomous actuation self-powered from a hot surface is remarkable, what brings the actuation to an end should be discussed. In principle, to have the oscillating motion go on with a constant amplitude and period, each actuation cycle must proceed under exactly the same melting-induced contractile force, the same crystallization-induced extensional force, as well as the same frictional force between the two ends of the strip and the substrate surface. In practice, however, many factors can intervene and deny the specimen a steady-state motion. We carried out X-ray diffraction and DSC measurements on a specimen before actuation and after reaching the end of actuation lasting over 1000 cycles. No decrease in crystallinity (Fig. S3, Table S1) and no deterioration of crystallite alignment was observed after actuation (Fig. S4), implying that the end of actuation was not caused by structural changes in the EVA samples. It seems that the main cause of the decaying autonomous actuation over time is the uneven and weakening contact of the specimen with the hot surface. Generally, as the amplitude decreases, the extensional force that flattens the strip becomes smaller, which results in a “loose” contact between them and, consequently, a less effective heating of EVA and melting of crystallites. This, in turn, leads to an even smaller jump amplitude that translates into a looser contact after the

descent. Such a deteriorating cycle continues to eventually end the actuation. Experimentally, the end of actuation was approached when the specimen experienced a sudden rise in period. Another observation supported this analysis. After an hour-long actuation (over 1000 cycles) was ended, compressing the specimen slightly against the hot surface could reactivate the autonomous actuation for a similar number of jump/descent cycles. With a sample of 0.5 mm-100 % (T_{surf} = 75 °C), this manual reactivation was repeated several times, resulting in over 8000 cycles totalling 8 h of actuation!

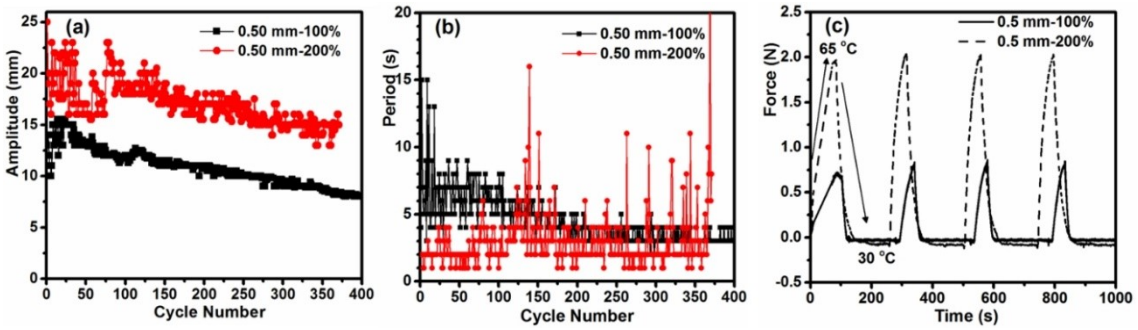

Fig. 3. Effect of specimen elongation. (a) and (b) Variation of actuation amplitude and period, respectively, with the number of jump/descent cycles for two specimens with the same dimension but different elongation degrees (100 % and 200 %) (T_{surf} = 75 °C). (c) Contractile force variation for the two specimens subjected to several cycles of heating (to 65 °C) and cooling (to 30 °C).

The autonomous motion of the polymer specimen is self-fuelled from the hot surface. Simple tests could be designed to appreciate the conversion of thermal energy to mechanical work in a self-sustained manner. During the up and down motion, the two ends of the specimen slide on the substrate surface toward and away from each other, respectively, when friction at the two ends is made similar by controlling the roughness. A low and even friction between the specimen and substrate on both sides facilitates the actuation and helps reach a steady-state of motion. However, with one end of the specimen purposely made rough to increase the friction with the substrate surface, the continuous jump and descent motion could lead to “walking” of the specimen in the direction of the end with lower friction (Fig. 4, Movie S2). In another handmade device, one end of a thin rod is attached to the upper side of a specimen and the other end is joined to the arm of a

wheel. By putting the specimen on the substrate surface, the up and down actuation could make the wheel rotate 25 times over 1 min (Fig. 5, Movie S3), mimicking a diaphragm pump. As a final note, in all autonomous motion tests, despite the fact that the two ends of specimen were in constant contact with the substrate surface, rigid skeleton domains should remain because T_{surf} was lower than $T_{m,high}$. Even with all crystallites melted in the two ends over time, the autonomous motion of the central section of the specimen would continue as long as the thermo-mechano-thermal feedback loop persisted.

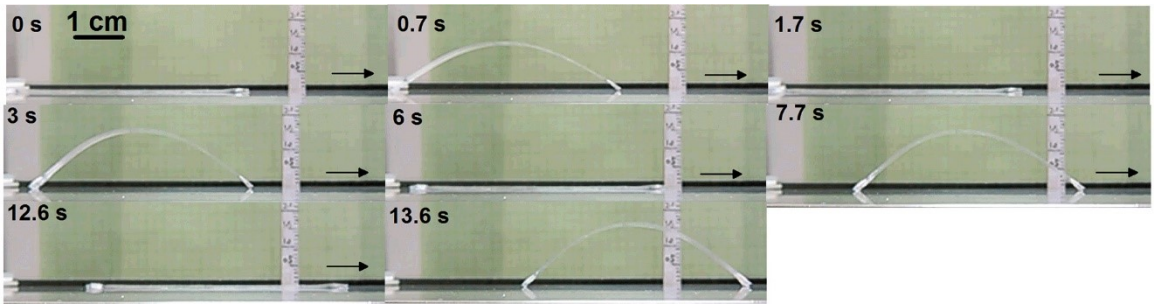

Fig. 4. Snapshots showing the self-walking of a specimen (100 % elongation, 65 × 3 × 0.5 mm^3) on the substrate surface (T_{surf} = 75 °C). The left end of the specimen was made to have more friction with the substrate than the right end.

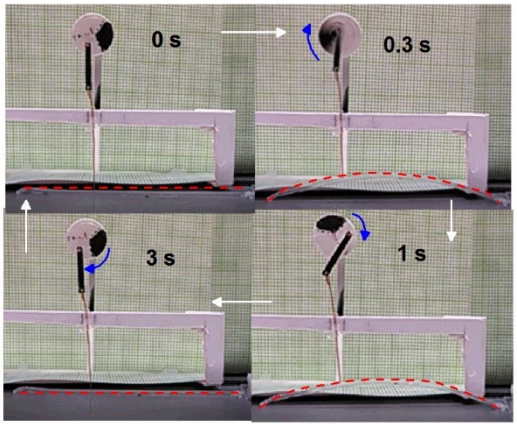

Fig. 5. Snapshots showing the rotation of a wheel driven by the autonomous actuation of a specimen (100 % elongation, 65 × 3 × 0.9 mm^3) on the substrate surface (T_{surf} = 75 °C). The strip actuator is marked with red dashed line for clarity.

2.3.4 Conclusions

In summary, we have demonstrated a strategy that allows thermal phase transition-based polymer actuators, like crosslinked EVA, that can undergo repeated contraction/elongation upon repeated heating/cooling cycles, to exhibit autonomous, self-sustained motion with no need for temperature switching. We showed that by placing a flat specimen of EVA with aligned crystallites on the surface of a heated substrate, crystallite melting-induced longitudinal contraction occurs on the lower side of the specimen in contact with the substrate, and the unbalanced contraction force elevates the central section of the specimen to form an arch. Once in the air, the specimen is cooled down and oriented chain segments recrystallize, which induces an extensional force on the same side that brings the specimen back to the flat state and, by doing so, causes the specimen to touch the substrate surface to reinitiate the actuation cycle. This way, a thermo-mechano-thermal feedback loop can be created, which is indispensable for the autonomous actuation only fuelled by the hot substrate surface. We investigated the effect of substrate surface temperature, specimen elongation and thickness on the jump amplitude and the period of the oscillating motion. Hour-long actuation with over a thousand cycles of motion was achieved. Such continuous motion of a solid polymer driven by thermal energy and without on/off temperature switching is unprecedented. Based on the validated mechanism, potentially exploitable polymer actuators are not limited to semicrystalline polymers like EVA. Any polymer that displays reversible contraction and elongation associated with a reversible thermal phase transition could be applied for such autonomous actuation. Moreover, the potential of doing mechanical work on a hot substrate subsurface by making use of direct thermomechanical energy conversion was demonstrated.

Acknowledgements

Y. Zhao acknowledges financial support from the Natural Sciences and Engineering Research Council of Canada (NSERC) and le Fonds de recherche du Québec: Nature et technologies (FRQNT). F. Ge thanks FRQNT and China Scholarship Council (CSC) for awarding him a scholarship. W. Fan and D. Fortin are acknowledged for DSC and XRD measurements, respectively. Y. Zhao is a member of the FRQNT-funded Center for Self-

Assembled Chemical Structures (CSACS) and the Centre québécois sur les matériaux fonctionnels (CQMF).

Notes and references

1 (a) L. Hines, K. Petersen, G. Z. Lum and M. Sitti, *Adv. Mater.*, 2017, **29**, 1603483; (b) H. Meng and G. Li, *J. Mater. Chem. A*, 2013, **1**, 7838; (c) D. Rus and M. T. Tolley, *Nature*, 2015, **521**, 467.

2 T. Masuda, M. Hidaka, Y. Murase, A. M. Akimoto, K. Nagase, T. Okano and R. Yoshida, *Angew. Chem.*, 2013, **52**, 7468.

3 (a) S. Maeda, Y. Hara, T. Sakai, R. Yoshida and S. Hashimoto, *Adv. Mater.*, 2007, **19**, 3480; (b) R. Tamate, A. Mizutani Akimoto and R. Yoshida, *Chem. Rec.*, 2016, **16**, 1852; (c) R. Yoshida, *Adv. Mater.*, 2010, **22**, 3463.

4 (a) H. Arazoe, D. Miyajima, K. Akaike, F. Araoka, E. Sato, T. Hikima, M. Kawamoto and T. Aida, *Nat. Mater.*, 2016, **15**, 1084; (b) B. Li, T. Du, B. Yu, J. van der Gucht and F. Zhou, *Small*, 2015, **11**, 3494; (c) M. Ma, L. Guo, D. G. Anderson and R. Langer, *Science*, 2013, **339**, 186.

5 (a) X. Zhang, Z. Yu, C. Wang, D. Zarrouk, J. W. Seo, J. C. Cheng, A. D. Buchan, K. Takei, Y. Zhao, J. W. Ager, J. Zhang, M. Hettick, M. C. Hersam, A. P. Pisano, R. S. Fearing and A. Javey, *Nat. Commun.*, 2014, **5**, 2983; (b) A. H. Gelebart, G. Vantomme, B. E. Meijer and D. J. Broer, *Adv. Mater.*, 2017, **29**, 1616712; (c) Y. Li and H. F. Yu, *ACS Appl. Mater. Interfaces,* 2015, **7**, 3834.

6 S. Palagi, A. G. Mark, S. Y. Reigh, K. Melde, T. Qiu, H. Zeng, C. Parmeggiani, D. Martella, A. Sanchez-Castillo, N. Kapernaum, F. Giesselmann, D. S. Wiersma, E. Lauga and P. Fischer, *Nat. Mater.*, 2016, **15**, 647.

7 (a) M. Yamada, M. Kondo, J.-i. Mamiya, Y. Yu, M. Kinoshita, C. J. Barrett, and T. Ikeda, *Angew. Chem.*, 2008, **47**, 4986; (b) H. F. Yu and T. Ikeda, *Adv. Mater.*, 2011, **23**, 2149; (c) E. Uchida, R. Azumi and Y. Norikane, *Nat. Commun.*, 2015, **6**, 7310.

8 (a) T. J. White, N. V. Tabiryan, S. V. Serak, U. A. Hrozhyk, V. P. Tondiglia, H. Koerner, R. A. Vaia and T. J. Bunning, *Soft Matter*, 2008, **4**, 1796; (b) S. Serak, N. Tabiryan, R. Vergara, T. J. White, R. A. Vaia and T. J. Bunning, *Soft Matter*, 2010, **6**, 779; (c) K. M. Lee, M. L. Smith, H. Koerner, N. Tabiryan, R. A. Vaia, T. J. Bunning and T. J. White, *Adv. Funct. Mater.*, 2011, **21**, 2913.

9 K. Kumar, C. Knie, D. Bleger, M. A. Peletier, H. Friedrich, S. Hecht, D. J. Broer, M. G. Debije and A. P. Schenning, *Nat. Commun.*, 2016, **7**, 11975.

10 (a) H. Zhang, W. Duan, L. Liu and A. Sen, *J. Am. Chem. Soc.*, 2013, **135**, 15734; (b) H. Zhang, K. Yeung, J. S. Robbins, R. A. Pavlick, M. Wu, R. Liu, A. Sen and S. T. Phillips, *Angew. Chem.*, 2012, **51**, 2400.

11 (a) R. F. Ismagilov, A. Schwartz, N. Bowden and G. M. Whitesides, *Angew. Chem. Int. Ed.*, 2002, **41**, 652; (b) T. Mirkovic, N. S. Zacharia, G. D. Scholes and G. A. Ozin, *Small*, 2010, **6**, 159.

12 X. He, M. Aizenberg, O. Kuksenok, L. D. Zarzar, A. Shastri, A. C. Balazs and J. Aizenberg, *Nature*, 2012, **487**, 214.

13 M. Behl, K. Kratz, U. Noechel, T. Sauter and A. Lendlein, *Proc. Natl. Acad. Sci. U. S. A.*, 2013, **110**, 12555.

14 M. Behl, K. Kratz, J. Zotzmann, U. Nöchel, A. Lendlein, *Adv. Mater.* 2013, **35**, 4466.

15 F. Ge, X. Lu, J. Xiang, X. Tong and Y. Zhao, *Angew. Chem., Int. Ed.,* 2017, **56**, 6126.

2.3.5 Supporting Information

Materials and Methods

Sample preparation 6 g EVA (containing 18 wt.% of VA, Sigma-Aldrich, Canada) was first dissolved in 50 ml toluene at 80 ℃ under magnetic stirring to form homogeneous solution, which was then cooled to 55 ℃ and subsequently added with 0.123 g DCP (dicumyl peroxide, Sigma-Aldrich, Canada) and continuously stirred for 10 min. The above solution was first cast into a petri dish to allow evaporation of the solvent overnight in the hood, then moved to a vacuum oven and dried at 60 ℃ for 48 hours to remove the residual solvent. The obtained composite containing 2.0 wt.% DCP was cut into particulates and then hot-compressed (170 ℃ and 2.5 MPa for 10 min, then 190 ℃ and 3.0 MPa for 10 min, and finally 200 ℃ and 3.5 MPa for 25 min) and crosslinked (using Carver Laboratory Press, Model C, Fred S. Carver Inc., USA) in metal molds into sheets with desired dimensions.

Programming aligned specimens Strips were cut off from the above prepared samples, and stretched manually at a rate of about 5 mm s^{-1} (above 90 ℃) with tweezers to desired elongations ε_p, $\varepsilon_p = 100\ \% \times (L_p - L_0) / (L_0 - 5\ mm)$, where L_0 is the original length before programming, L_p is the length after stretching. In the above equation, 5 mm was subtracted since the corresponding parts (with a total length of 5 mm) covered by the tweezers at the two ends were not stretched. For example, a strip with original dimension of 35 mm in length, 4.3 mm in width and 0.7 mm in thickness was stretched to 75 mm with ε_p of 133 %, and then heated on the hot surface at 75 ºC to reduce the length to 65 mm, with final ε_p of 100 %. Then the elongated samples were cooled in air under constant strain at room temperature for shape fixation. For the strips with final elongation of 200 %, the original length and width were 2.5 mm and 4.8 mm, respectively. All samples were programmed to the final length of 65 mm and width of 3 mm to perform the tests and measurements.

Tests The autonomous oscillating motion was characterized by monitoring the amplitude and period for each cycle for a given specimen put on a hot surface made of steel and heated under control by a hot plate (Fisher Scientific, USA). All tests were conducted in a hood (equipped with AFA 1000 airflow monitor, motto manufacturing LTD, England) with

velocity of air flow at 160 ± 5 fpm. Both the amplitude and the period were read from the video.

Measurements The isostrain experiments were performed at a given temperature in a tensile machine (Instron 5965 universal testing system equipped with a chamber oven and controlled by Bluehill 3 software, UK). Samples were clamped and held at constant strain in the chamber, and subjected to heating at 36 °C min^{-1} and cooling at 10 °C min^{-1} while the forces were monitored in real time. The temperature change of the sample during a motion cycle was measured by an infrared thermometer (FLIR TG165). DSC measurements were carried on a TA Q200 instrument. Samples were heated from 20 °C to 100 °C at a rate of 5 °C min^{-1} under nitrogen flow with a rate of 50 ml min^{-1}. Data from the first scan were collected for analysis. WAXS and SAXS patterns were collected with a Bruker AXS Nanostar system equipped with a Microfocus Copper Anode at 45 kV / 0.65 mA, MONTAL OPTICS and a VANTEC 2000 2D detector at 90 mm distance (WAXS) and 1070 mm distance (SAXS), respectively, from the samples calibrated with a Silver Behenate standard.

Additional Results and Discussion

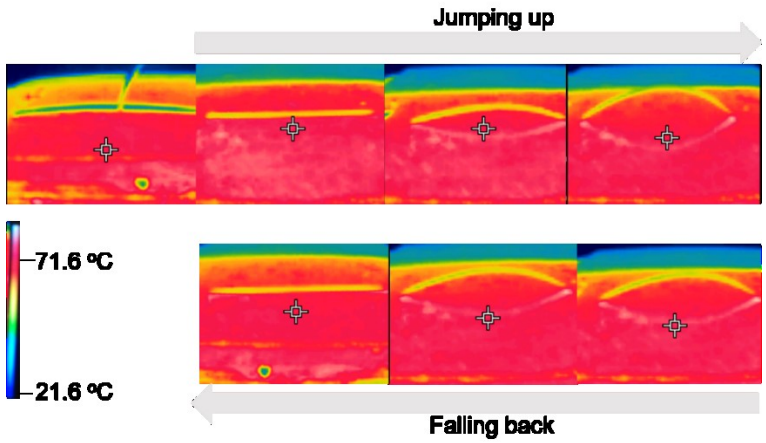

Fig. S1 Infrared images showing the temperature variation in a strip of 0.5 mm-100 % during one up/down motion cycle on the substrate surface at T_{surf} = 75 °C. The first image on the left of the upper row was recorded with the strip in the air before being deposited on the hot surface.

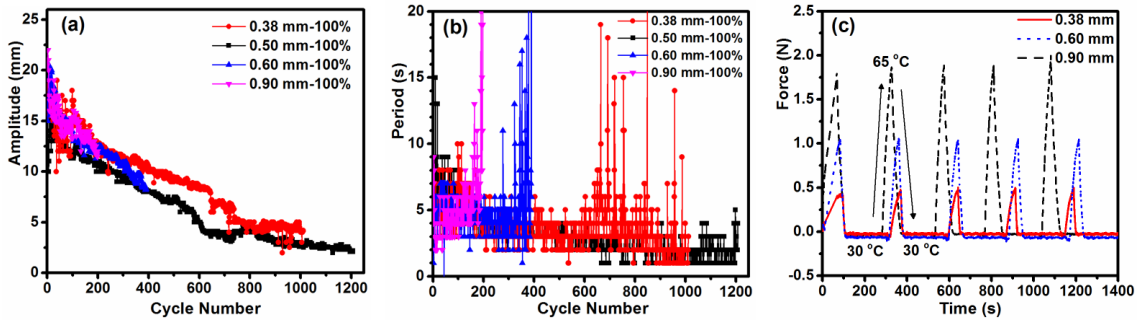

Fig. S2 Effect of specimen thickness. (a) and (b) Variation of actuation amplitude and period, respectively, over the number of jump/descent cycles for specimens of different thicknesses (100 % elongation and on substrate surface at T_{surf} = 75 °C). (c) Contractile force variation for three specimens of different thicknesses subjected to several cycles of heating (to 65 °C) and cooling (to 30 °C).

To investigate the effect of specimen thickness, four samples were prepared to have the same elongation degree (100 %), length and width but different thicknesses ranging from 0.38 to 0.90 mm. The results using T_{surf} = 75 °C show that the thickness had an important effect on the number of completed cycles, i.e., the total actuation time (Fig. S2a and S2b). While the thicker ones stopped jumping earlier in time with fewer cycles, the two thinner samples could autonomously actuate much longer, over 1 h. As expected, the contraction force generated by the whole volume of specimen increased with increasing the thickness (Fig. S2c), which, however, is not telling about the contraction force responsible for the jumping up and down actuation. At the same T_{surf}, the amount of melted crystallites would be similar in all specimens regardless of the thickness, which means a larger fraction of melted crystallites and thus larger proportion of actuation domains for a thinner specimen. This appears to be necessary for a sustainable, self-powered actuation. From the above, it appears certain that the performance of the autonomous actuation, in terms of amplitude, speed and duration, is affected by the interplay of a number of parameters. Although a precise and complete control on the actuation seems difficult at this point, the key role of some parameters is clear. On the one hand, the jump amplitude is mostly governed by the melting-induced contraction force. At a given specimen thickness, bigger contraction force can be obtained by using either higher T_{surf} to increase the fraction of melted crystallites,

or higher elongation degree to store more strain energy in the specimen. On the other hand, the period is mainly determined by the time required for the specimen to flatten from the arch shape. Large extensional force from fast crystallization would induce fast actuation with short period. However, what induces a large contraction force upon crystallite melting cannot ensure fast actuation, which is the case of using high T_{surf} that could warm the air around the specimen and thus slow down the crystallization.

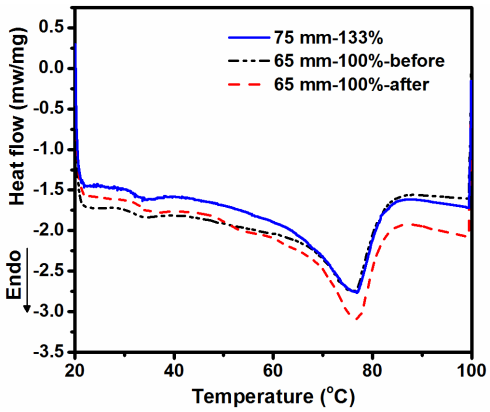

Fig. S3 DSC (first heating) curves for samples preprogrammed (blue solid), before jumping (black dash dot dot) and after jumping (red dash).

Table S1. Thermal parameters of EVA samples obtained from DSC measurement.

Sample	T_m [°C][a)]	ΔH_m [J g^{-1}] [b)]	X_c [%][c)]
75 mm-133 %	76.8	-46.43	16.8
65 mm-100 %-before	76.5	-45.31	16.4
65 mm-100 %-after	76.8	-48.73	17.6

[a)] T_m is the peak melting temperature during the first heating cycle. [b)] ΔH_m is the enthalpy of melting. [c)] X_c is the crystallinity obtained from the first heating using $X_c = (\Delta H_m/\Delta H^*_m) \times 100$ %, where ΔH^*_m is the enthalpy of melting of perfect polyethylene crystal, 277.1 J g^{-1} based on reference[s1].

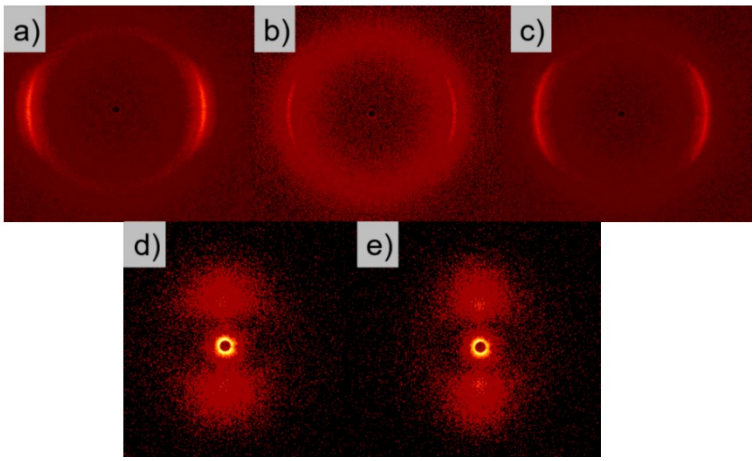

Fig. S4 2D-WAXS patterns (upper series) for preprogrammed sample 75 mm-133 % (a), sample 65 mm-100 % before jumping (b), after jumping for 1000 cycles (c) and 2D-SAXS patterns (lower series) for sample 65 mm-100 % before jumping (d) and after jumping for 8000 cycles (e).

Supporting References

[s1] R. P. Quirk and M. A. A. Alsamarraie in *Polymer handbook*, *3rd edition* (Eds.: J. Brandrup, E. H. Immergut), Wiley-Interscience Publication, New York, **1989,** pp. V/19.

2.4 Summary of the Project

In this project, we have created a smart actuator system in which a crosslinked EVA strip with aligned crystallites continuously arches up and flattens down when placed on a substrate of constant temperature, free of temperature on/off switching or other external intervention. This autonomous, self-sustained motion is inspired by the reversible actuation of the EVA/AuNPs optical actuators, which bend toward the light source upon light illumination and unbend when the light is turned off. It has been confirmed in Chapter 1 that the bending is driven by the asymmetric melting-induced-contraction (MIC), which can be induced by a temperature gradient across the thickness of the strip, while the unbending is induced by the asymmetric cooling-induced-elongation (CIE), which occurs when the directed crystallization proceeds in air. Our design is to put the strip at the interface of a hot solid substrate at T_{surf} and a cold gaseous phase (air) and establish a temperature gradient from the bottom layer to the top layer of the strip. Once in contact with the hot substrate, the strip is activated to bend up due to the unbalanced contraction; once in air, the strip expands due to directed crystallization and recovers to flat shape, which is reactivated again to a bent arch shape to continue the motion cycle. The thermo-mechano-thermal feedbackloop is thereby put forward and responsible for the oscillation. We investigated the effect of T_{surf}, sample thickess and sample elongation on the actuation amplitude and the period. It was found that the amplitude increased with the increase in T_{surf} and elongation, while the period decreased with the increase of elongation. Higher T_{surf} kept the motion for a longer time while larger thickness and elongation ended the oscillation earlier. Hour-long and more than 1000 cycles of motion were achieved. It was speculated that the loose contact between the strip surface and the substrate surface in the later stage was the main reason for the decay of the oscillation. We demonstrated that the autonomous motion could be transformed into linear self-walking and rotational motion of a wheel, proving the direct conversion of thermal energy to physical work or mechanical energy.

CHAPTER 3 A MULTIFUNCTIONAL DYE-DOPED LIQUID CRYSTAL POLYMER ACTUATOR: LIGHT-GUIDED TRANSPORTATION, TURNING IN LOCOMOTION, AND AUTONOMOUS MOTION

3.1 About the Project

We have demonstated in the previous two chapters that polymer actuators based on semicrystalline EVA can display two types of bending/unbending behaviors. One is controlled by on/off switching of a laser, while the other is autonomous oscillation on a substrate at constant temperature. Both cases allow only partial melting of the crystsallites during actuation to avoid melting of the skeleton crystallites required for the reversibility. In addition to this constraint, the whole material is uniformly crosslinked and aligned, meaning that the motion is limited to simple modes. Therefore, the adaptivity and multifunctionality for polymer actuators are not satisfied with EVA actuators. In contrast, the diversity of mesogen alignments combined with polymer network elasticity enables various reversible actuation in LCN-based actuators, including exotic shape changes and motions. So far, it remains rare to make monolithic LCN-based actuators multifunctional and controllable by one stimulus. In this work, we have developed a multifunctional LCE-based photoactuator doped with an NIR dye. We program a hierarchical structure consisting of polydomain and monodomain in a monolithic LCE strip through inhomogeneous photocrosslinking. The programmed strip is confined on a substrate at two ends, with the monodomain side set downward, and scanned by an NIR laser from one end to the other. After scanning, a bump emerges at the near-laser end of the strip and is found to be able to drive a rod-like object rolling forward as the bump is scanned again by the laser toward the other end. We cut the scanned strip into two parts, one containing the bump and the other being flat. With two ends free, the strip can crawl and turn in a wanted direction during asymmetric laser scanning. When suspended in air with one end attached to the substrate and illuminated constantly with a laser, the strip can produce multiple modes of autonomous motion under a self-shadowing mechanism. We investigate the factors that influence the locomotion speed and the mode of autonomous motion. This work paves the way toward light-controlled multifunctional soft polymer actuators and robots.

3.2 Contributions

This work was published in *Angew. Chem. Int. Ed.*, **2018**, *57*, 11758 by Feijie Ge, Rong Yang, Xia Tong, Franck Camerel and Yue Zhao. This research work was conducted in Université de Sherbrooke under the supervision of Prof. Yue Zhao. Prof. Zhao and I designed the experiments and made analysis of all the data. I conducted most of the experiments and characterizations. In detail, I prepared the actuators and measured their spectral properties, photothermal effect and photomechanical properties. I demonstrated all the functions, collected and processed all the data and created all the Figures and the Scheme. Rong Yang synthesized the liquid crystal polymer during his stay in Sherbrooke, Franck Camerel synthesized the used dye (at Université de Rennes, France) and Xia Tong helped with analysis of the photomechanical data. I wrote the first version of the manuscript, based on which Franck Camerel made a revision and Prof. Yue Zhao modified, revised and finalized the manuscript.

3.3 Paper Published in Angewandte Chemie International Edition 2018, 57, 11758.

A Multifunctional Dye-doped Liquid Crystal Polymer Actuator: Light-Guided Transportation, Turning in Locomotion and Autonomous Motion

Feijie Ge, Rong Yang, Xia Tong, Franck Camerel, and Yue Zhao*

F. Ge, X. Tong, Prof. Dr. Y. Zhao

Département de Chimie, Université de Sherbrooke, Sherbrooke, Québec, J1K 2R1, Canada.

E-mail: yue.zhao@usherbrooke.ca

Dr. R. Yang

Jiangsu Key Laboratory of Environmentally Friendly Polymeric Materials, School of Materials Science and Engineering, Changzhou University, Changzhou 213164, China

Dr. F. Camerel

Univ Rennes, CNRS, ISCR-UMR6226, F-35000 Rennes, France

3.3.1 Abstract

A strip of a liquid crystal elastomer doped with a near-infrared dye with one side crosslinked monodomain and the other crosslinked polydomain along the thickness behaves like a multifunctional photoactuator without the need for a support. A flat strip with two ends fixed on substrate surface forms a moving bump under laser scanning, which can be used as light-fueled conveyor to transport an object. Cutting off and laser scanning the bump with two free ends makes a soft and flexible millimeter-scale crawler that can not only move straight and climb an inclined surface, but also undergo light-guided turning to right or left as a result of combined out-of-plane and in-plane actuation. Based on the self-shadowing mechanism, with one end of the strip fixed on substrate surface, it can execute a variety of autonomous arm-like movements under constant laser illumination, such as bending–unbending and twisting, depending on the laser incident angles with respect to the strip actuator.

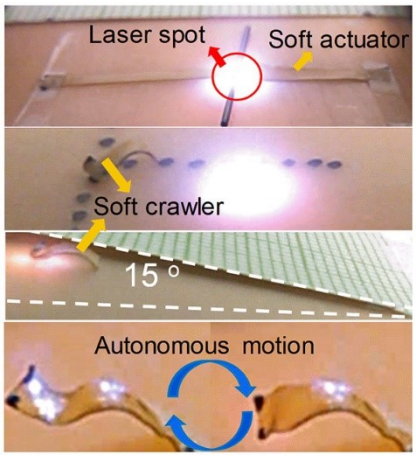

3.3.2 Introduction

Soft materials have attained more and more applications as active components that perform or transfer mechanical motions.[1] They are intrinsically or are designed to be responsive to different stimuli, such as chemicals, temperature, moisture, magnetic field, electrical field, and light.[1, 2] Photoresponsive materials stand out from the others owing to preference for clean energy, wireless and remote manipulation, and localized control.[3] However, to achieve light-enabled multifunctionality using one material is intriguing and challenging. Soft optical actuators are emerging as potential active components in soft robots, because they provide flexible shape change and sophisticated mechanical motions as required in robotic systems.[4] Smart platforms capable of manipulating objects on liquid or solid surfaces[5] and active devices possessing swimming,[6] rotating,[6b, 7] walking or crawling[8] abilities are topics of great interest in recent years owing to potential applications in robotics. Few photoresponsive systems have been achieved that drive motion of liquid droplet in tubes,[9] on modified solid[10] or liquid surfaces[11] and that enable manipulation of solid particles.[12] Those surfaces contain azobenzene-based liquid-crystalline polymer (azo-LCP) in which photoisomerization induces the changes in surface properties that drive the motion. Chiral dopant added in azo-LCP induces handed twist of the mesogens, leading to twist-nematic molecular orientation through the film thickness.[13] These films convert light energy into helical shape changes that dictate the reversible macroscopic motion of a loaded magnet. White et al. reported both in-plane bending[14] and out-of-plane twisting[15] of optical oscillating cantilevers with different frequencies, using monodomain azo-LCPs. Broer et al.[16] has recently demonstrated oscillatory waves in azo-LCP films where the mesogens are distributed in a splay-aligned configuration through the thickness direction. The waves propagate repeatedly under constant light illumination through a self-shadowing mechanism, with their directions controlled by the mesogen orientations in the planar and homeotropic sides. Therein, the azobenzene derivatives have fast *cis–trans* thermal relaxation so that reversed bumping arises rapidly after light illumination. These photoactive films, when integrated into a supporting frame, exhibit light-driven locomotion and transportation abilities. Equally important, on the other hand, are the pioneering works on light-controlled LCP soft actuators using the photothermal effect by Yang and other groups.[2b, 17] LCPs have received much attention for developing photo-responsive small

crawlers ranging from the millimeter to micrometer scale.[18] Straight walking is shown while the tunability of the moving direction is unknown. One work has reported light-controlled walking and turning but using bilayer of reduced graphene oxide (rGO)/GO-polydopamine, on which gradient structures are programmed by patterning.[19] The most frequently investigated bilayers, composed of matrix layer such as silicon rubber,[6c, 20] UV-cured polymer,[21] or polypeptide hydrogel[22] and constraint layer derived from modified graphene or carbon nanotubes, have also been transformed into optical walkers. Using the photothermal effect, Broer et al. developed LCP/photostabilizer composites with splay alignment distribution of mesogens in the thickness direction to work as mechanical oscillators.[23] However, despite much progress in the field, it remains challenging and elusive to demonstrate multifunctionality using a single light-responsive LCP without the help of another material in the form of supporting layer or frame. Herein, we report a dye-doped LCP whose single-strip actuator of uniaxial LC orientation is capable of carrying out a number of light-guided motions and functions. With strip two ends fixed, scanning an NIR laser can generate a moving wave that pushes forward or backward a rod placed on the surface; with two ends free, the actuator becomes a flexible crawler that not only can move and climb under laser control but can also turn right or left as commanded by light. If only one end is fixed, the actuator can execute a variety of autonomous arm motions depending on the direction and angle of incidence of the laser with respect to the long axis of the strip.

3.3.3 Results and Discussion

The chemical structures of the used materials are shown in Figure 1. A liquid crystal elastomer (LCE) bearing cinnamyl comonomer units for photocrosslinking of polymer chains[24, 25] and N,N'-dialkylimidazolidine-2,4,5-trithone nickel complex carrying 2-butyloctyl carbon chains as a molecular photothermal agent, denoted as imNi8(4) hereafter.[26] The metal-bis(dithiolene) complex was selected for its dominant absorption in the NIR spectral region (making the light-controlled actuator eventually appealing for biomedical uses), its high photothermal stability and high photothermal conversion efficiency, and its good dispersity in polymers.[27] Figure 1 b shows the UV/Vis-NIR absorption spectrum of the NIR dye in solution and the spectra of a LCE/imNi8(4) film

(0.2 wt %) recorded before and after photocrosslinking through dimerization of cinnamyl groups (Supporting Information, Figure S1) for different times. Even at such a small content in the polymer, the absorption peak of imNi8(4) centered at 974 nm is prominent and unchanged after 90 min UV exposure, implying the stability of the dye. Figure 1 c shows the temperature profiles measured with an infrared camera when a strip of LCE/imNi8(4) (0.2 wt %) was exposed to 980 nm laser of varying intensity. The achievable temperature depends on the laser power (similar result obtained with a thermocouple; Supporting Information, Figure S2). At the laser intensity of 3.9 W cm^{-2} or higher, the temperature rises within seconds above the nematic to isotropic phase transition temperature ($T_{NI} \approx 55$ °C; Supporting Information, Figure S3), while it drops once the laser is turned off. DSC measurements show that while the presence of 0.2 wt % of imNi8(4) has no effect on the thermal phase transition temperatures (T_g, smectic–nematic T_{SN} and T_{NI}; Supporting Information, Figure S4), the crosslinking broadens the LC–isotropic phase transition region owing to the confinement of the smectic ordering within crosslinked chain network. Although weakened, the persistence of a smectic phase was confirmed by XRD (Supporting Information, Figure S5). Therefore, loading a small amount of the NIR dye allows the use of 980 nm laser to control the order–disorder phase transition and thus the actuation of the LCE-based materials. Unless otherwise stated, to prepare a multifunctional photoactuator, prior to photocrosslinking the LCE/imNi8(4) (0.2 wt %) mixture was thermally compressed into films with desired thicknesses (0.2 mm, 0.3 mm, or 0.4 mm), cut into thin strips (10 mm in length, 3.5 mm in width), and stretched in nematic state (50–52 °C) to 330 % strain to yield monodomain of uniaxial LC orientation along the stretching direction (Supporting Information, Figure S6).

To fabricate multifunctional LCE/imNi8(4) actuators, a non-uniform photocrosslinking of the LC monodomain of the sample is crucial. A typical example of preparation is as follows: after stretching a strip of 0. 2 mm thick to 330 % strain for uniaxial LC orientation, one side of the sample was exposed to UV light (320 nm, 160 mW cm^{-2}) for 20 min for polymer chain crosslinking. The sample was then placed in hot water at 60 °C (in the isotropic state) for relaxation and equilibrium (it curled towards the non-crosslinked side). Following cooling back to room temperature, the non-crosslinked side was exposed to UV light for 40 min for photocrosslinking of LC polydomain. The LCE/imNi8(4) actuator

prepared above is denoted as 0.2 mm-UV20+40, with the three numbers indicating the thickness of the strip before stretching, UV irradiation time for the monodomain side and that for the polydomain side, respectively. It comprises essentially an actuating side (crosslinked monodomain) and a non-actuating side (crosslinked polydomain). In reality, a gradient of crosslinking density likely exists. Depending on the preparation conditions used, such as the sample thickness, UV irradiation intensity, and UV irradiation time for either side, the relative proportion of the actuating and non-actuating sides of the strip can be varied, which affect the properties of the actuator such as actuation force and reversible shape change in the ordered and disordered states (Supporting Information, Figure S7). For this actuator, the reversible contraction and extension of the actuation side in the isotropic and LC states, respectively, leads to the reversed curling of the strip as shown in Figure 1 d. As demonstrated below, 980 nm laser-controlled order–disorder phase transition in spatially localized regions of the actuators, being accompanied by reversible shape change at light on and off states, enables the multiple functions of the single strip of LCE/imNi8(4).

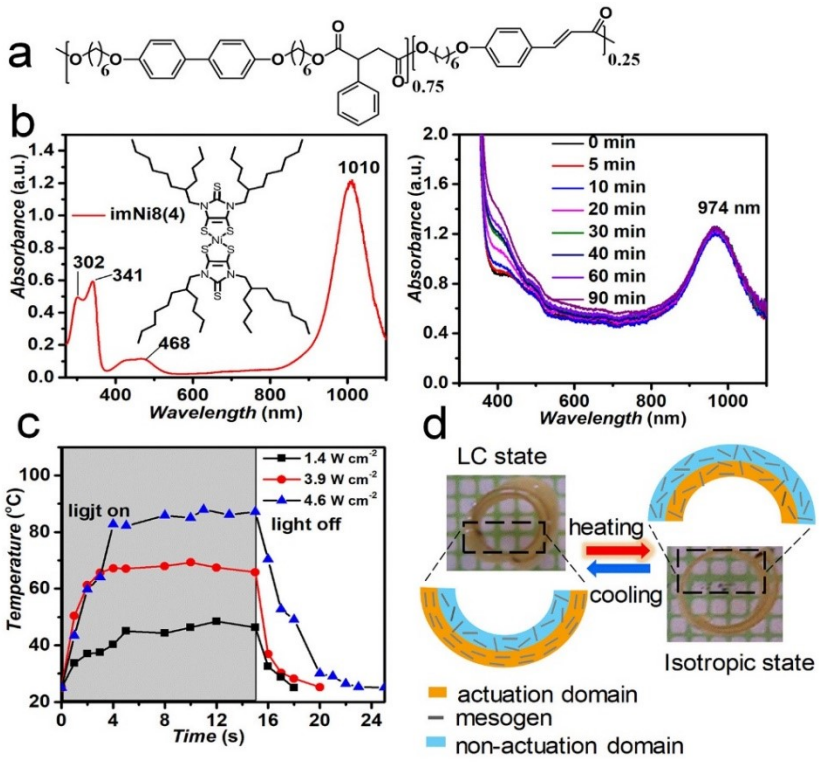

Figure 1. a) Chemical structure of the liquid crystal elastomer (LCE) used. b) Chemical structure of the near-infrared dye (imNi8(4)), UV/Vis-NIR absorption spectra of the dye in

dichloromethane (9.5×10^{-6} M), and (right) a film of LCE/imNi8(4) (0.2 wt % dye) before and after exposure to UV light (160 mW cm^{-2}) for photocrosslinking of the polymer for different times. c) Temperature variation of the LCE/imNi8(4) (0.2 wt %) film with time over 980 nm laser on/off at different intensities. The sample used is 0.2 mm-UV20+40. d) Reversible curling for the film 0.2 mm-UV20+40 between nematic and isotropic states.

The first function of the actuator strip is light-driven transportation of an object sitting on the surface as a result of moving laser generated wave propagation. This is shown in Figure 2. A strip of 0.2 mm-UV20+60 was attached at both ends on a fluorescent plate (to visualize the 980 nm NIR laser spot, Figure 2 a) and kept flat and straight, with the actuating side downward. When the 980 nm laser (3.9 W cm^{-2}) was applied from the top for several seconds and then moved away, an upward bump was formed at the initial laser spot (Supporting Information, Figure S8). Although in the isotropic phase under laser irradiation the actuating side tends to contract and curl the strip, the large bump formation is intriguing, because with the two ends fixed the straight strip should not be able to contract. The bump formation suggests that in the isotropic phase and under the contractile stress exerted by the actuating side, polymer chains underwent reorganization leading to a form of plastic flow, followed by elongation of the strip during cooling. As the 980 nm laser spot moved from right to left, the bump followed the spot, while the bump formed earlier shrank. This is likely explained by two actions. As the laser spot moves away, the initially irradiated spot cools and the bottom side of the strip extends due to the formation of LC monodomain. In the same time, as the new bump is formed nearby on the laser spot, the bottom side contracting of the strip can stretch the initial bump to form a new bump. In other words, the initial bump may arise mainly from polymer chain reorganization, the subsequent bump moving with the laser spot uses the extra length of the strip from the initial bump. This leads to the large-amplitude wave propagation guided by the laser. It should be emphasized that the wave propagation realized here differs from the known systems[16, 28] where it is necessary to fix the two ends of a strip at a distance shorter than the length of the strip to allow the bump formation. The laser-controlled wave propagation is robust and can go both ways (right–left followed by left–right). As a test, within 38 min, more than 100 single trips from end to end were realized without obvious fatigue (Supporting Information, Movie S1). To demonstrate a possible use of the moving wave to carry out a physical work, Figure 2

b shows light-driven transportation of an object. When a rod (carbon, glass, or copper) was placed on the strip in the vicinity of the bump, under laser scanning along the strip (about 0.8 mm s^{-1}), the bump moved with the laser spot and propelled the rod rolling forward step by step (Supporting Information, Movie S2). Therefore, a laser-controlled conveyor was created for rod-like objects, with the LCE/imNi8(4) actuator acting as a moving belt for transportation. In fact, parameters including light power, crosslinking density, and sample thickness are important for the moving bump and object transportation. Too low intensity is insufficient for increasing the temperature, while too high intensity leads to overheating and subsequent slow cooling unfavorable for quick isotropic–LC phase transition. For thinner samples (0.08 mm), lower intensity (3.9 W cm^{-2}) was chosen, while for thicker strips (0.17 mm), higher intensity (4.6 W cm^{-2}) was found to be effective for the moving bump (Supporting Information, Figure S9, Movie S3). The light-guided wave propagation velocity obviously is related to the laser scanning speed. But this can hardly be quantified with the manual manipulation. The laser scanning speed should be appropriate, because too fast scanning cannot promote the required order–disorder phase transition while too slow scanning makes the strip contract so much that the strip became totally flat without any wave during scanning.

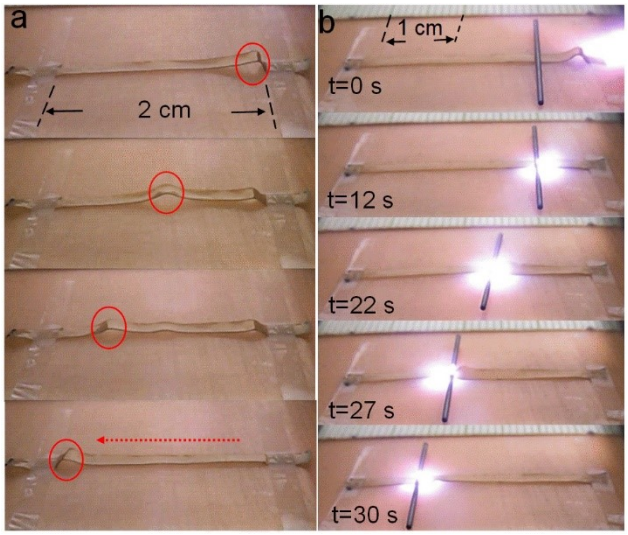

Figure 2. a) Photographs showing the generation and movement of a bump in a strip of LCE/imNi8(4) (0.2 mm-UV20+60) under 980 nm laser irradiation and end-to-end scanning. b) Photographs showing the laser-driven transportation of a carbon rod on the actuator strip

as being pushed by the propagating wave (Supporting Information, Movie S2), laser intensity 3.9 W cm^{-2}.

The second function of the LCE/imNi8(4) strip actuator is behaving like a light-guided flexible micro crawler that can not only move along a straight line or an inclined surface (15°) but also crawl in an on-demand direction. Basically, a worm-like crawler was prepared by cutting off the bump section from the scanned strip, with the two ends unattached and the actuating side of the strip still setting downward. As shown in Figure 3 a, being released from stress, the bump section with the end previously attached to the tape folded upward as head and the other part lied down as body. When scanned with a laser from the neck to the tail, the crawler body ascended to curl downward owing to asymmetric contraction, with the tail lifted and displaced forward while the head remained on the surface due to frictional forces. As the light spot left the tail, the body descended and elongated with the tail sticking on the surface and the head pushed forward owing to smaller friction of the fold against the surface. Repeating the above procedure made the crawler move forward step by step. A particularly interesting feature of this soft crawler is its ability to turn right or left as guided by laser (Figure 3 a). Scanning the laser spot on one edge of a quarter section from the neck and then uniformly to the tail of the crawler could deflect its motion as desired, as a result of asymmetric in-plane contraction in the width direction. Figure 3 shows that the crawler was scanned by light to walk on a specified route with a T-shape intersection. It was manipulated to turn to the left (Figure 3 b; Supporting Information, Movie S4) or to the right (Figure 3 c; Supporting Information, Movie S5) by asymmetric laser scanning. A laser-guided 180-degree U-turn was also achieved with a micro-crawler of 3 mm in length (Supporting Information, Movie S6). Furthermore, Figure 3 d shows that the crawler was able to crawl on a surface inclined by 15° (Supporting Information, Movie S7).

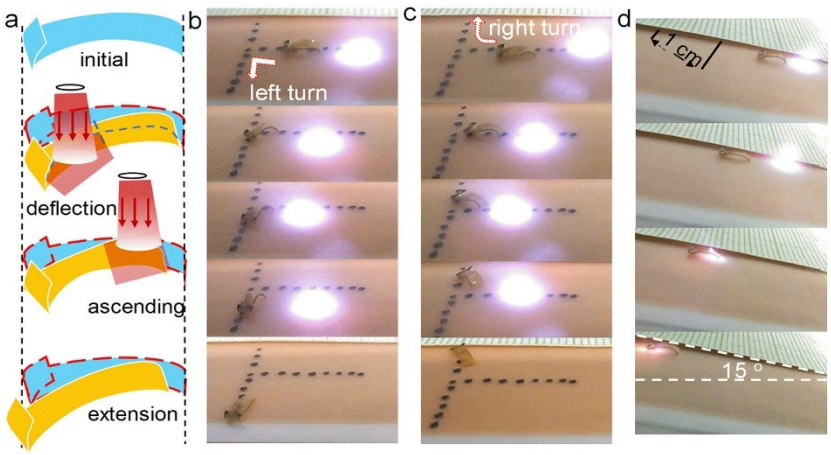

Figure 3. Laser-directed locomotion of a crawler on a fluorescent plate surface. a) Illustration of asymmetric scanning-induced direction deflection. b) Photographs showing a left turn at right angle (Supporting Information, Movie S4). c) Photographs showing a right turn at right angle (Supporting Information, Movie S5). d) Photographs showing climbing at speed of 12 mm min^{-1} on an inclined surface at 15° (Supporting Information, Movie S7), laser intensity being 1.4 W cm^{-2}. The crawler was prepared from strips of 0.2 mm-UV20+90.

The size of the flexible crawler and the intensity of the guiding laser can affect the crawling speed. Their effects were investigated for crawling on a horizontal surface and the results are reported in Figure 4. On the one hand, under a constant laser intensity of 3.9 W cm^{-2}, the maximum crawling speed was observed to increase from about 0.15 cm min^{-1} at body length of 2.5 mm to about 2 cm min^{-1} at the body length of 5 mm (Figure 4 a). Longer strips contracted and expanded more than the shorter ones in each cycle, enabling a larger step length and thus a faster movement. At 6 mm, the crawler maintained the maximum speed at 2 cm min^{-1}; above 6 mm, however, the sample easily fell down and therefore was not investigated further. On the other hand, using the same crawler of 6 mm in length, the crawling speed appears to increase linearly with the laser power. The speed was 1.2 cm min^{-1} at 1.4 W cm^{-2} and increased to 2.3 cm min^{-1} at 4.6 W cm^{-2}. Basically, higher laser intensity generated faster asymmetrical contraction and moved the crawler faster.

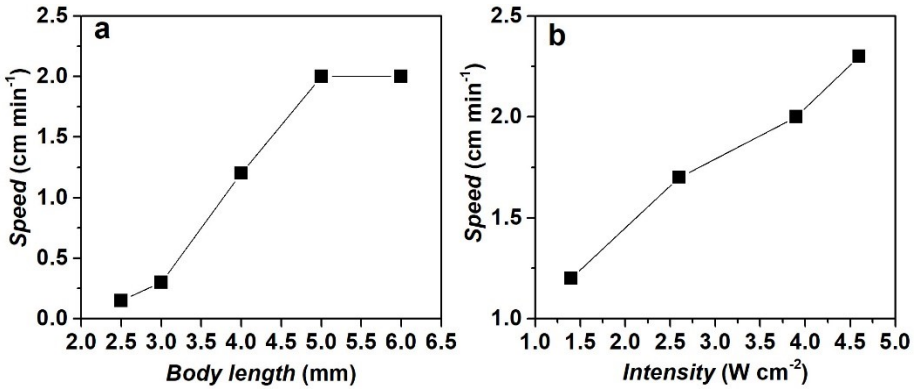

Figure 4. Speed of crawling as a function of a) body length (laser intensity, 3.9 W cm^{-2}) and b) laser intensity (body length, 6 mm). Samples were prepared from films of 0.2 mm-UV20+90.

The third function of the LCE/imNi8(4) actuator is the autonomous arm-like motion under constant light illumination. This can be achieved by tethering one end of an actuator strip (with the actuation side down) to substrate surface and leaving the other end suspending in air. When laser is applied through a certain angle, the sections of the strip hit by the laser spot deform due to heating-induced order-disorder phase transition; if the deformation deflects those sections from the laser path, the actuator undergoes a back-motion upon cooling-induced disorder–order phase transition and, by doing so, are hit by the laser again, which initiates new cycle of motion. Most interesting is the ability of the flexible actuator to execute versatile self-sustained motions by adjusting the incident laser direction. With the free strip section set essentially horizontal, the laser was applied along the long axis of the strip (the uniaxial LC orientation direction) at a grazing angle of 15° (angle between laser beam and surface). As seen in Figure 5 a, the section receiving light bent upward first (after 5 s) and then bent downward (7 s), thus deviating from the laser beam. Once bent and unirradiated, the head section cooled naturally in air and unbent to the flat position, where the laser hit the head again to resume the same cycle of motions consisted of upward bending (29 s), downward bending (31 s) and return to level. As such, a photothemo-mechano-thermal feedback loop was established, which elicited the autonomous motion continuously for 345 cycles within 66 min (Figure 5 a; Supporting Information, Figure S10 and Movie S8).

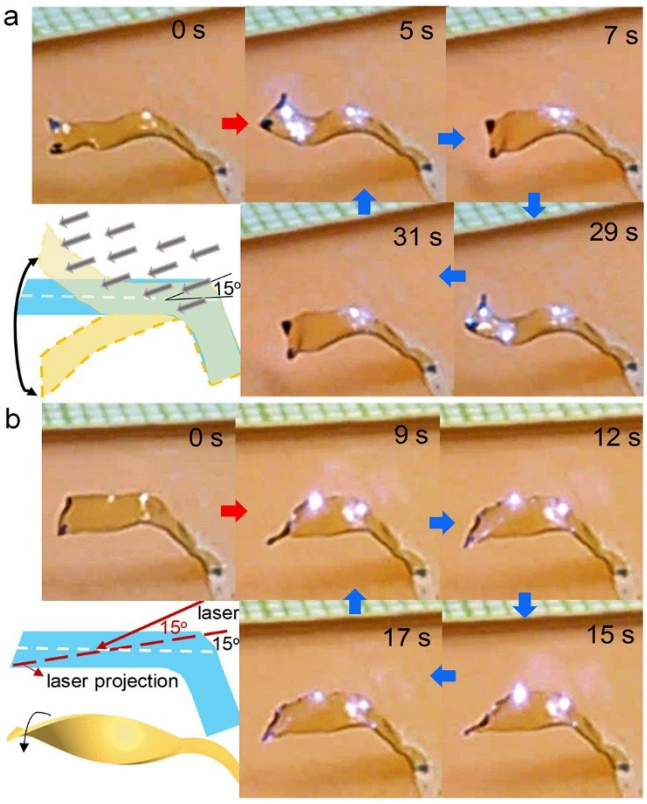

Figure 5. Autonomous arm-like motions of the strip actuator (10 mm in length, cut from a laser-scanned specimen 0.2 mm-UV20+90) under constant illumination of laser (1.4 W cm^{-2}) over time: a) laser applied at a grazing angle of 15° and along the actuator (laser beam projection coincides with the long axis of the strip; Supporting Information, Movie S8); and b) laser applied at a grazing angle of 15° while being rotated by 15° around the surface normal (laser beam projection makes an angle of 15° with the long axis of the strip; Supporting Information, Movie S9).

In this case, when the laser beam hits the surface, it takes some time for uniform heating above T_{NI} across the thickness; thus within the first few seconds, the actuating areas are near the surface, giving rise to the upward bending. As time goes on, the actuating areas propagate to the bottom, and the overall asymmetrical contraction leads to downward bending. Therefore, under the laser direction used, the self-sustained motion mode is mainly upward–downward bending. In contrast, as shown in Figure 5 b, while keeping the 15° grazing angle, if the laser beam was rotated by only 15°around the surface normal (that is, the projection of the beam making an angle of 15° with the long axis of the strip),

twisting motion was generated as the laser beam was deflected from the long axis of the strip (Figure 5 b; Supporting Information, Movie S9). For the twisting mode, the width of the strip was only partially irradiated by the laser and, as a result, the asymmetrical contraction in both the width and thickness directions contributed to the twisting motion. The autonomous twisting lasted 35 min with a total of 112 cycles (slower than the bending motion). Changing the laser intensity (Supporting Information, Figure S11 and Movie S10), grazing angle (Figure S12 and Movie S11), or applying a constant vibrating laser beam (Movie S12) are among the variables that affect the motion mode, amplitude, and speed, leading to a variety of light-driven autonomous arm-like motions (see the Supporting Information).

3.3.4 Conclusions

In summary, we have obtained light-controlled conveyor, walker, and autonomous arm-like motion using a single-layer strip of NIR dye-doped LCE whose reversible shape change is governed by thermal order–disorder phase transition. We show that through the use of photocrosslinking to prepare strip actuator with crosslinked LC monodomain of uniaxial orientation on one side (actuating side) and crosslinked LC polydomain on the other side (non-actuating side), the soft actuator is multifunctional and capable of exhibiting a variety of actuation modes. By attaching the two ends of a flat strip to the substrate surface, laser exposure generates a bump as a result of structural rearrangement, and subsequent laser scanning can cause the bump to propagate, which can be used to realize end-to-end transportation of an object. By fixing one end of the strip, the free side of the actuator can undergo versatile light-driven arm-like movements that are self-sustained and determined mainly by the incident laser direction with respect to the actuator. The photothermo-mechano-thermal feedback loop responsible for the autonomous motion is explained by a self-shadowing mechanism. Finally, the actuator with two free ends can be guided by laser to crawl straight either horizontally or on a slope and, more particularly, to turn right or left in an on-demand manner owing to combined asymmetrical contractions both in-plane and out of plane. The demonstrated multifunctions of the soft actuator are a significant step forward in the field.

Acknowledgements

This work receives financial support from the Natural Sciences and Engineering Research Council of Canada (NSERC) and le Fonds de recherche du Québec: Nature et technologies (FRQNT). F.G. acknowledges FRQNT and China Scholarship Council (CSC) for a scholarship. D. Fortin is acknowledged for performing XRD measurements. F.C. thanks the CNRS, Rennes Métropole, and the Région Bretagne for their financial supports.

Conflict of interest

The authors declare no conflict of interest.

Keywords: autonomous motion · liquid crystal elastomers · photoactuators · polymer actuators · soft robots

References

[1] L. Hines, K. Petersen, G. Z. Lum, M. Sitti, *Adv. Mater.* **2017**, *29*, 1603483.

[2] a) A. S. Lubbe, T. van Leeuwen, S. J. Wezenberg, B. L. Feringa, *Tetrahedron* **2017**, *73*, 4837–4848; b) L. T. de Haan, C. Sanchez-Somolinos, C. M. Bastiaansen, A. P. Schenning, D. J. Broer, *Angew. Chem. Int. Ed.* **2012**, *51*, 12469–12472; *Angew. Chem.* **2012**, *124*, 12637–12640.

[3] a) T. Seki, *Bull. Chem. Soc. Jpn.* **2018**, *91*, 1026–1057; b) M. Yamada, M. Kondo, R. Miyasato, Y. Naka, J.-i. Mamiya, M. Kinoshita, A. Shishido, Y. Yu, C. J. Barrett, T. Ikeda, *J. Mater. Chem.* **2009**, *19*, 60–62; c) H. Yu, T. Ikeda, *Adv. Mater.* **2011**, *23*, 2149-2180.

[4] H. Zeng, P. Wasylczyk, D. S. Wiersma, A. Priimagi, *Adv. Mater.* **2018**, *30*, 1703554.

[5] a) M. Kobayashi, J. Abe, *J. Am. Chem. Soc.* **2012**, *134*, 20593–20596; b) W. Wang, Y.-Q. Liu, Y. Liu, B. Han, H. Wang, D.-D. Han, J.-N. Wang, Y.-L. Zhang, H.-B. Sun, *Adv. Funct. Mater.* **2017**, *27*, 1702946; c) D. Okawa, S. J. Pastine, A. Zettl, J. M. J. Fréchet, *J. Am. Chem. Soc.* **2009**, *131*, 5396–5398.

[6] a) M. Camacho-Lopez, H. Finkelmann, P. Palffy-Muhoray, M. Shelley, *Nat. Mater.* **2004**, *3*, 307–310; b) S. Palagi, A. G. Mark, S. Y. Reigh, K. Melde, T. Qiu, H. Zeng, C. Parmeggiani, D. Martella, A. Sanchez-Castillo, N. Kapernaum, F. Giesselmann, D. S. Wiersma, E. Lauga, P. Fischer, *Nat. Mater.* **2016**, *15*, 647–653; c) W. Jiang, D. Niu, H. Liu, C. Wang, T. Zhao, L. Yin, Y. Shi, B. Chen, Y. Ding, B. Lu, *Adv. Funct. Mater.* **2014**, *24*, 7598–7604.

[7] G. Vantomme, A. H. Gelebart, D. J. Broer, E. W. Meijer, *Tetrahedron* **2017**, *73*, 4963–4967.

[8] a) E. Diller, J. Zhuang, G. Zhan Lum, M. R. Edwards, M. Sitti, *Appl. Phys. Lett.* **2014**, *104*, 174101; b) T. Shen, M. G. Font, S. Jung, M. L. Gabriel, M. P. Stoykovich, F. J. Vernerey, *Sci. Rep.* **2017**, *7*, 16178.

[9] J. A. Lv, Y. Liu, J. Wei, E. Chen, L. Qin, Y. Yu, *Nature* **2016**, *537*, 179–184.

[10] a) J. Berná, D. A. Leigh, M. Lubomska, S. M. Mendoza, E. M. Pérez, P. Rudolf, G. Teobaldi, F. Zerbetto, *Nat. Mater.* **2005**, *4*, 704–710; b) K. Ichimura, S.-K. Oh, M. Nakagawa, *Science* **2000**, *288*, 1624–1626; c) S.-K. Oh, M. Nakagawa, K. Ichimura, *J. Mater. Chem.* **2002**, *12*, 2262–2269.

[11] a) A. Diguet, R. M. Guillermic, N. Magome, A. Saint-Jalmes, Y. Chen, K. Yoshikawa, D. Baigl, *Angew. Chem. Int. Ed.* **2009**, *48*, 9281–9284; *Angew. Chem.* **2009**, *121*, 9445–9448; b) N. Kavokine, M. Anyfantakis, M. Morel, S. Rudiuk, T. Bickel, D. Baigl, *Angew. Chem. Int. Ed.* **2016**, *55*, 11183–11187; *Angew. Chem.* **2016**, *128*, 11349–11353.

[12] a) A. Kausar, H. Nagano, Y. Kuwahara, T. Ogata, S. Kurihara, *Chem. Eur. J.* **2011**, *17*, 508–515; b) A. Kausar, H. Nagano, T. Ogata, T. Nonaka, S. Kurihara, *Angew. Chem. Int. Ed.* **2009**, *48*, 2144–2147; *Angew. Chem.* **2009**, *121*, 2178–2181.

[13] S. Iamsaard, S. J. Aßhoff, B. Matt, T. Kudernac, J. J. Cornelissen, S. P. Fletcher, N. Katsonis, *Nat. Chem.* **2014**, *6*, 229–235.

[14] a) T. J. White, N. V. Tabiryan, S. V. Serak, U. A. Hrozhyk, V. P. Tondiglia, H. Koerner, R. A. Vaia, T. J. Bunning, *Soft Matter* **2008**, *4*, 1796–1798; b) T. J. White, S. V. Serak, N. V. Tabiryan, R. A. Vaia, T. J. Bunning, *J. Mater. Chem.* **2009**, *19*, 1080–1085.

[15] K. M. Lee, M. L. Smith, H. Koerner, N. Tabiryan, R. A. Vaia, T. J. Bunning, T. J. White, *Adv. Funct. Mater.* **2011**, *21*, 2913–2918.

[16] A. H. Gelebart, D. J. Mulder, M. Varga, A. Konya, G. Vantomme, E. W. Meijer, R. L. B. Selinger, D. J. Broer, *Nature* **2017**, *546*, 632–636.

[17] a) L. Liu, M.-H. Liu, L.-L. Deng, B.-P. Lin, H. Yang, *J. Am. Chem. Soc.* **2017**, *139*, 11333–11336; b) M. Wang, B.-P. Lin, H. Yang, *Nat. Commun.* **2016**, *7*, 13981; c) L.-X. Guo, M.-H. Liu, S. M. Sayed, B.-P Lin, P. Keller, X.-Q. Zhang, Y. Sun, H. Yang, *Chem. Sci.* **2016**, *7*, 4400–4406; d) R. R. Kohlmeyer, J. Chen, *Angew. Chem. Int. Ed.* **2013**, *52*, 9234–9237; *Angew. Chem.* **2013**, *125*, 9404–9407.

[18] a) M. Rogóż, H. Zeng, C. Xuan, D. S. Wiersma, P. Wasylczyk, *Adv. Opt. Mater.* **2016**, *4*, 1689–1694; b) H. Zeng, O. M. Wani, P. Wasylczyk, A. Priimagi, *Macromol. Rapid Commun.* **2018**, *39*, 1700224; c) H. Zeng, P. Wasylczyk, C. Parmeggiani, D. Martella, M. Burresi, D. S. Wiersma, *Adv. Mater.* **2015**, *27*, 3883–3887.

[19] J. Mu, C. Hou, H. Wang, Y. Li, Q. Zhang, M. Zhu, *Sci. Adv.* **2015**, *1*, e1500533.

[20] Y. Hu, J. Liu, L. Chang, L. Yang, A. Xu, K. Qi, P. Lu, G. Wu, W. Chen, Y. Wu, *Adv. Funct. Mater.* **2017**, *27*, 1704388.

[21] M. Ji, N. Jiang, J. Chang, J. Sun, *Adv. Funct. Mater.* **2014**, *24*, 5412–5419.

[22] E. Wang, M. S. Desai, S. W. Lee, *Nano Lett.* **2013**, *13*, 2826–2830.

[23] A. H. Gelebart, G. Vantomme, B. E. Meijer, D. J. Broer, *Adv. Mater.* **2017**, *29*, 1606712.

[24] a) R. Yang, Y. Zhao, *Angew. Chem. Int. Ed.* **2017**, *56*, 14202–14206; *Angew. Chem.* **2017**, *129*, 14390–14394; b) R. Yang, Y. Zhao, *ACS Macro Lett.* **2018**, *7*, 353–357.

[25] A. Lendlein, H. Jiang, O. Junger, R. Langer, *Nature* **2005**, *434*, 879–882.

[26] K. Mebrouk, F. Camerel, O. Jeannin, B. Heinrich, B. Donnio, M. Fourmigué, *Inorg. Chem.* **2016**, *55*, 1296–1303.

[27] M. Ciancone, K. Mebrouk, N. Bellec, C. Le Goff-Gaillard, Y. Arlot-Bonnemains, T. Benvegnu, M. Fourmigué, F. Camerel, S. Cammas-Marion, *J. Mater. Chem. B* **2018**, *6*, 1744–1753.

[28] L. Dong, X. Tong, H. Zhang, M. Chen, Y. Zhao, *Mater. Chem. Front.* **2018**, *2*, 1383–1388.

3.3.5 Supporting Information

Experimental Procedures

Materials

Dichloromethane was purchased from Sigma-Aldrich and used as received. LCE and imNi8(4) was previously synthesized and characterized in supporting references s1 and s2, respectively.

Composite film preparation

Dye-doped LCE was prepared by mixing 3 g of LCE and 6 mg of imNi8(4) in 30 ml dichloromethane followed by complete evaporation of the solvent in hood at room temperature. After drying in a vacuum oven at 40 ℃ for 48h, LCE/imNi8(4) containing 0.2 wt % photothermal agent was formed. The composite was thermally compressed at 80 ℃ for 2h in a Teflon mold with desired thickness (0.2 mm, 0.3 mm and 0.4 mm).

Sample strips preparation

The compressed films (0.2 mm in thickness) were cut into 10 mm × 3.5 mm in length and width, respectively, and then stretched with tweezers at 50-52 ℃ in water to 37 mm × 1.38 mm × 0.08 mm, with the final strain at 350 ± 20 %. For samples with original thickness of 0.3 mm and 0.4 mm, the final thickness after stretching was 0.13 mm and 0.17 mm, respectively. Crosslinking was carried out using a UV Spot Curing System (Omnicure 1000 series) through a filter with wavelength in the range of 320-480 nm. The UV light intensity was measured using a photometer set at 320 nm. As an example (Scheme S1), sample 0.2 mm-UV20+40 was prepared by first UV-crosslinking the monodomain sample at one side for 20 min on a hot plate set at 47 ℃, at an UV light intensity of 160 mW cm^{-2}, followed by immersing in hot water (60 ℃) for stress relaxation in free state. After cooling naturally to r.t., the sample was dried and transferred back to the hot plate, kept flat and then crosslinked of the other side for 40 min. For the sample referred to as 60+80 ℃+60, the monodomain sample was UV-crosslinked at intensity of 80 mW cm^{-2} for 60 min first,

followed by constant length (80-90 % of the original) stress relaxation at 80 ℃ on the hot plate and then crosslinked the other side for another 60 min.

Preparation of a conveyor, crawler and autonomous arm

The fabrication process is shown in Scheme S1. First, scanning slowly (1 mm s^{-1}) a flattened strip that was attached at both ends to a substrate from one end to the other. As the laser spot was removed from one end of the strip, a bump arose from the end (Figure 2 and Scheme S1). Then, the strip was cut by a razor into two segments, from the dividing line between the bump and the flat part. The tape attached to the section containing the bump was peeled off carefully to avoid any stretching or damage to the material. The bump with a head was used as crawler. As the body length was decreased below 3 mm, the head was reduced in length correspondingly so as to adjust the friction force between the head and the substrate. The autonomous actuator with length of 10 mm was cut off from the flat part of the same scanned strip. With the initially crosslinked layer (actuation domain) facing the substrate, the right end of the actuator was attached to the substrate while the left end was suspended freely in air. The laser was fixed at the right side of the actuator, with its light beam tilted for 15° or 20° with the substrate surface. The long axis of the actuator was set at a position where the projection of the laser beam on the substrate was parallel to that of the actuator (for in plane bending-unbending autonomous motion) or forming an angle of 15°.

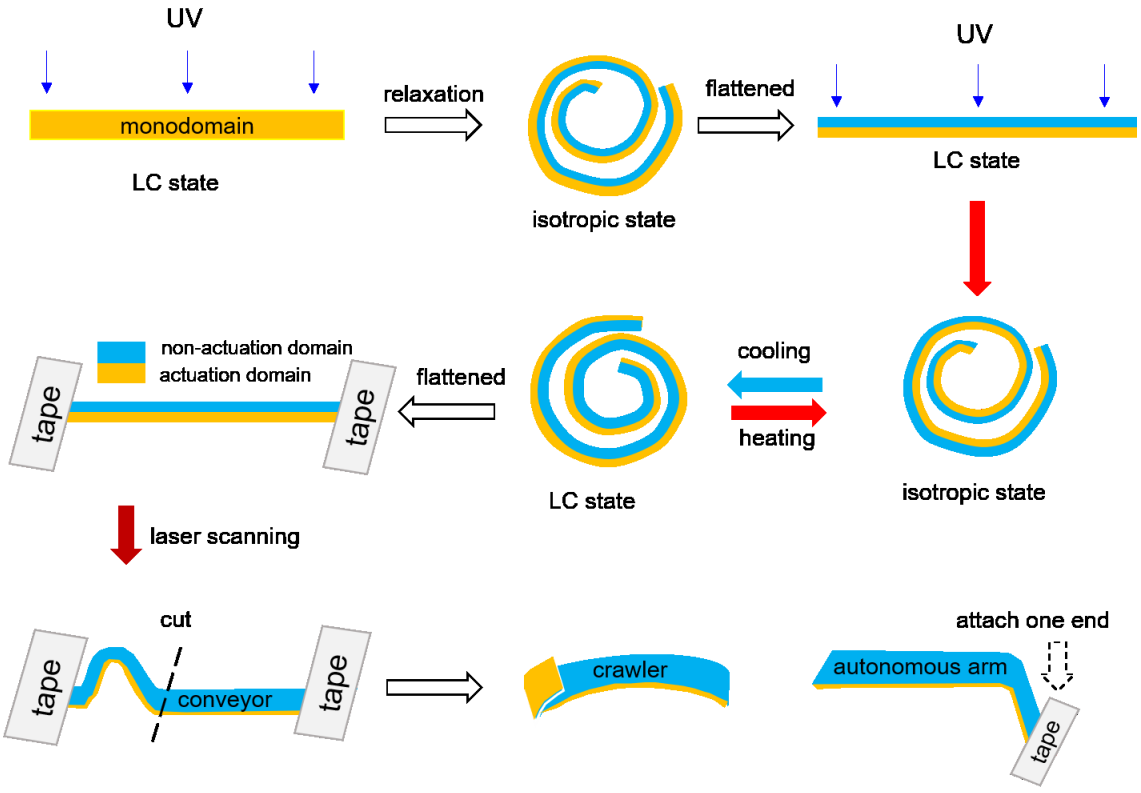

Scheme S1. A strip stretched to monodomain was UV-crosslinked on one side in LC state first, followed by immersing in water (60 °C) for stress relaxation. When cooled to LC state the strip was flattened and UV-crosslinked of the reverse side. The non-uniformly crosslinked strip was again immersed in water (60 °C) and cooled to LC state to show a curling and reversal curling performance. The strip was then flattened with the actuation domain downward and the two ends fixed on the substrate. After laser scanning from right to left, a bump was formed where the laser left the strip, and this scanned strip was fabricated as a photo conveyor. The bump was cut off from the strip, peeled off of the tape, cut to desired length and used as a crawler, while the flat section was cut to 10 mm in length and then attached one end to the substrate to work as an autonomous arm. The bending of the autonomous arm was caused by laser illumination to establish the self-shadowing.

Characterizations

UV-Vis-NIR spectrometer (Varian) was used to measure the absorption spectra of imNi8(4) in solution and the composite film from 190 nm to 1100 nm. Phase transition temperatures were determined by a differential scanning calorimeter (DSC, TA) in the range of -20 to

100 °C at a rate of 5 °C min^{-1}, under protection of nitrogen flowing at 50 ml min^{-1}. Laser power was measured by a power meter (TURNER, gentec-co). Laser light intensity was calculated by dividing the measured power over the area of the laser spot (with a radius of 0.94 ± 0.02 mm). Photothermally induced temperature rise was recorded by using thermocouple and infrared camera (Testo 875i). Wide-angle X-ray scattering (WAXS) were performed on a Bruker AXS Nanostar system with a microfocus copper anode, MONTAL OPTICS and a VANTEC 2000 2D detector at 90 mm from the samples. The X-ray wavelength was 0.154 nm.

Photomechanical forces were measured using a tensile machine (Instron 5965 with a load of 5N). Strips were held by clamping the two ends at a distance of 23.5 mm. Stress-relaxation mode was used, and a preload of 0.003 N was applied to the strips before irradiation to keep them straight. Laser (LaserSource 4300 Series, Arroyo Instruments) with wavelength of 980 nm was used to irradiate the strips from a constant distance of 15 cm.

Supporting Figures

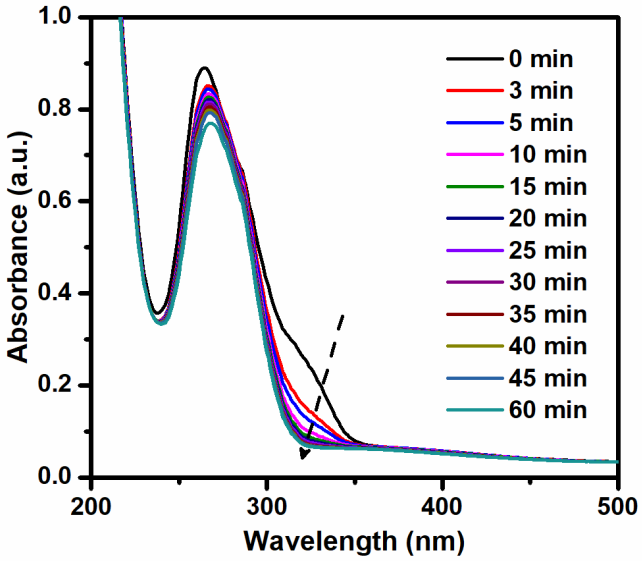

Figure S1. UV-Vis absorption spectra of an LCE/imNi8(4) film (thickness ca. 10 µm) spin-coated on quartz with different time of UV-crosslinking. The content of imNi8(4) was 0.2 wt % and the UV light intensity was 80 mW cm^{-2}.

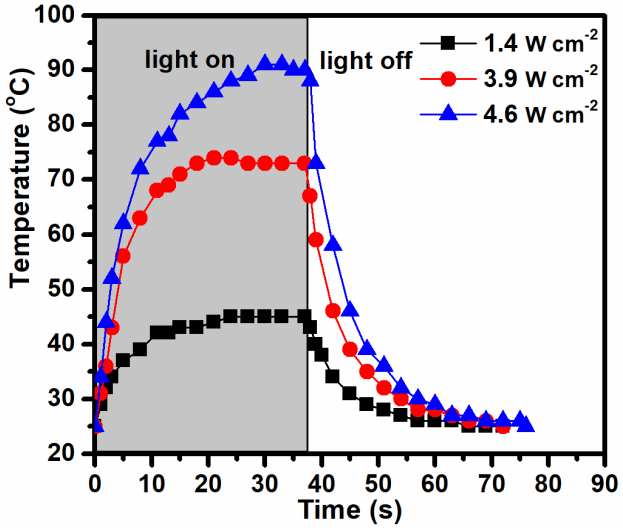

Figure S2. Temperature variation of the LCE/imNi8(4) (0.2 wt %) film upon exposure to 980 nm laser at different intensities and after turning off the laser. A thermocouple was used to measure the temperature change.

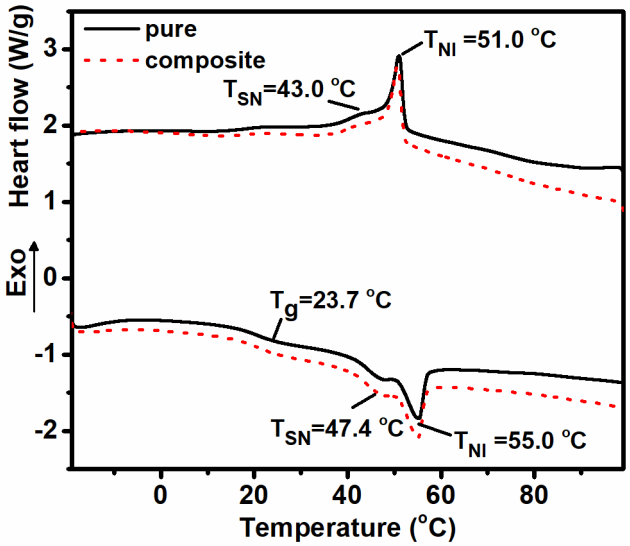

Figure S3. DSC traces for LCE and LCE/imNi8(4) (0.2 wt %) composite measured on second heating and first cooling before crosslinking.

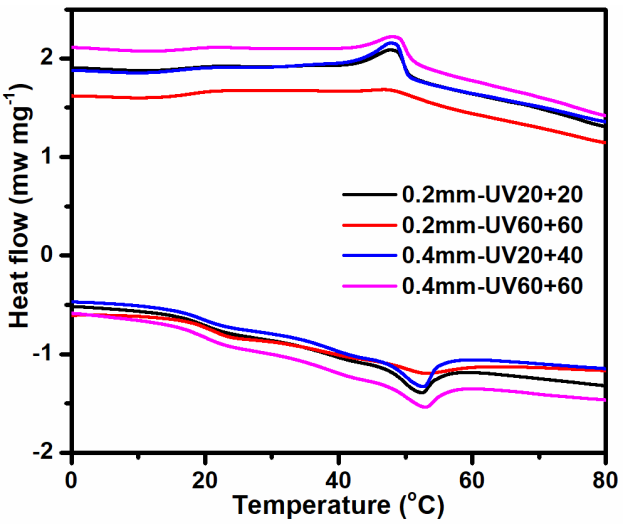

Figure S4. DSC traces for LCE/imNi8(4) (0.2 wt %) composite with different crosslinking times.

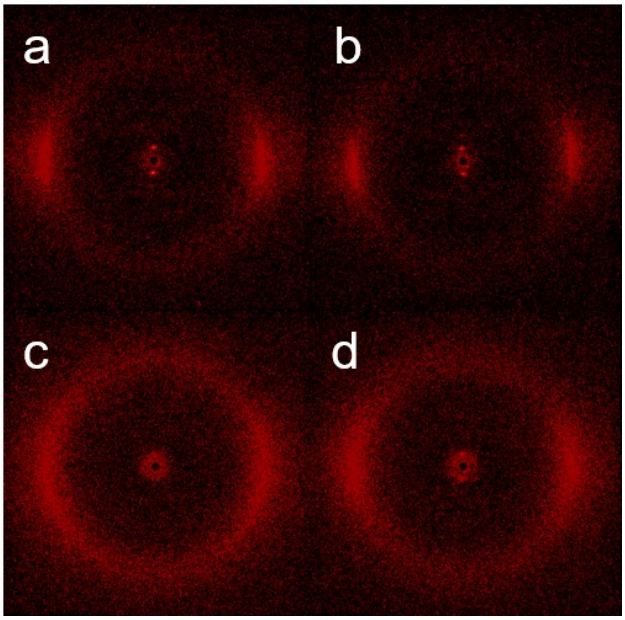

Figure S5. 2D-XRD patterns for a) pure LCE film (0.2 mm-UV20+40, b) composite film (0.2 mm-UV20+40, c) the bump section generated in composite film (0.2 mm-UV20+90, and d) the flat section neighboring the bump after laser scanning. All films were initially stretched to a strain of 330 %.

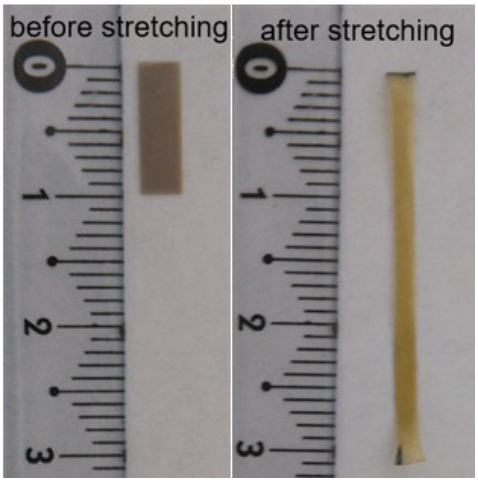

Figure S6. Transformation of LCE film (0.2 mm-thick) from polydomain (left) to monodomain (right) by stretching in nematic state. The obtained film has a strain of around 330 % and thickness of about 80 μm.

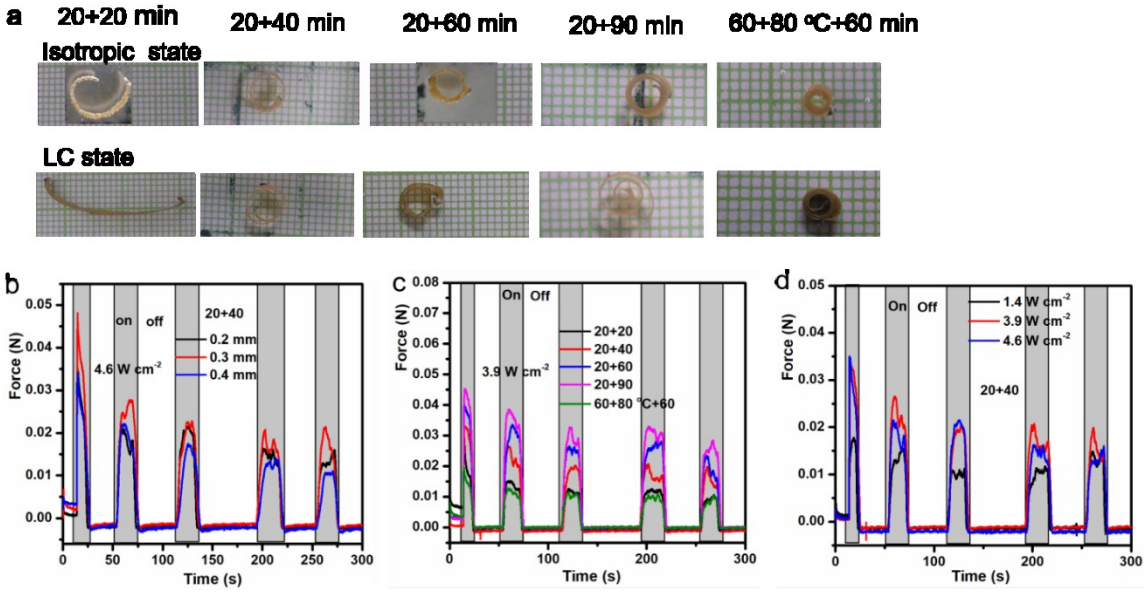

Figure S7. Effect of crosslinking time of the non-actuating side on the reversible shape change of the strips in water (a) and effect of different parameters, thickness (b), crosslinking time (c), and laser illumination intensity (d) on photomechanical forces generated in stress relaxation mode. In (a) and (c), 60+80 °C+60 indicates the monodomain sample was UV-crosslinked for 60 min first, followed by constant length (80-90% of the original) stress relaxation at 80 °C and then crosslinked the other side for another 60 min.

Samples crosslinked non-uniformly showed contraction and expansion reversibly accompanied by curling and reversal curling (Figure S7a) with a reversible degree (RD, defined as elongation of sample in liquid crystal state over the length in isotropic state) of about 40 % as common LCEs manifest during heating and cooling, while sample 60+80 ℃+60 had a reversible degree of 18% (Figure S7a, right). However, crosslinking at lower intensity (80 mW cm^{-2} for sample 60+80 ℃+60) endowed the sample with much larger curvature (Figure S7a, right) than crosslinking at higher intensity (160 mW cm^{-2}, Figure S7a, the first four pictures). In the former case, primarily only the surface layer was crosslinked due to weaker light intensity, and then the length was intentionally shortened for constant-strain thermal relaxation. During relaxation, the sample shrank and flattened with the strain energy in the uncrosslinked layer released, while polymer chains in the crosslinked layer were reorganizing as confined by crosslinking point. When the strip was cooled under constant strain to room temperature, polydomain formed in the uncrosslinked layer while monodomain was regained in the crosslinked layer. Subsequently the polydomain was crosslinked at the same light intensity for 60 min to enhance rigidity of the sample. When the sample was again immersed into hot water, isotropic transition of the monodomain led to contraction significantly while the polydomain layer showed little contraction. As a result, the sample had to curl to the maximum with the initially crosslinked layer inside, endowing the sample with very large curvature. During cooling, the inner side expanded as monodomain reformed and finally reversed the curling with comparably large curvature (Figure S7a, right). In the latter case with crosslinking intensity at 160 mW cm^{-2}, however, the curvature was smaller (Figure S7a) due to likely a gradient crosslinking density and decreased with the decrease of the crosslinking time of the non-actuating layer.

Samples with different thickness and crosslinking density were subjected to photomechanical test. The strip, clamped at their two ends at constant distance, were irradiated by laser spot covering their width and the forces generated were monitored. Figure S7b shows that for samples with different thickness, the forces generated were comparable at photothermal temperature above T_{NI} due to a similar proportion of monodomain, despite the crosslinking procedure was the same. For thicker samples, both photothermal heating and cooling speeds were slower compared with thinner ones, thus

was not used as crawler or arm-like autonomous actuator. Figure S7c shows that the photomechanical forces increased with the time of crosslinking, which agrees with the fact that higher crosslinking density prevent the polymer networks from severe relaxation, thus samples 0.2 mm-UV20+90 min were mainly used as autonomous actuators. Due to existence of polydomains in sample 60+80 °C+60, which was crosslinked at much lower UV light intensity, the contraction in isotropic state was limited, producing weak contractile forces (Figure S7c). At higher laser illumination intensity (Figure S7d), the generated forces were increased faster due to stronger photothermal effect, and this contributed to the increase of crawling speed with laser scanning intensity.

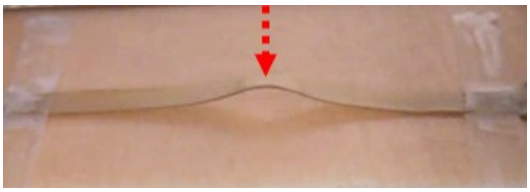

Figure S8. Strip sample 0.2 mm-UV20+60 ready for laser illumination were flattened and constrained at both ends, with the crosslinked actuation layer downward facing the fluorescent plate. The sample was irradiated by laser (at 3.9 W cm^{-2}) in the middle for 10 seconds, after which a convex bump emerged at the irradiated region as the laser was removed.

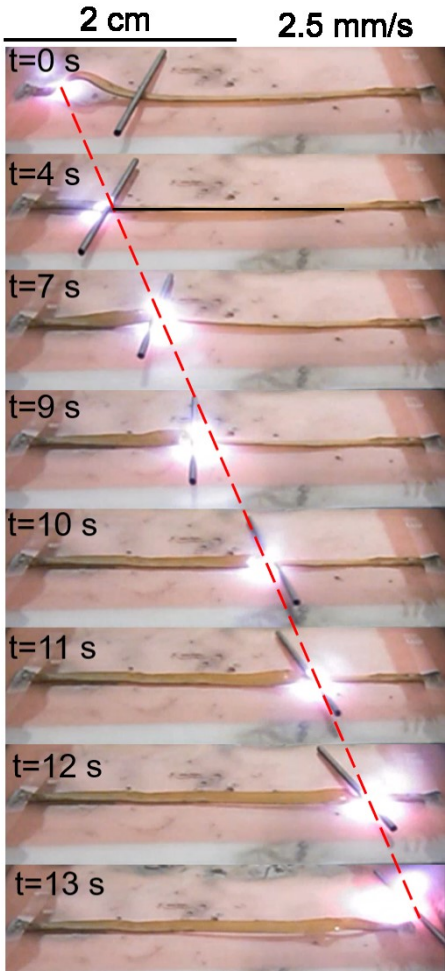

Figure S9. Screenshots (taken from Movie S3) showing the positional variation with time during laser scanning (at the intensity of 4.6 W cm^{-2}) for sample 0.4 mm-UV20+40 as optical conveyor. The average velocity of the rod movement was 2.5 mm s^{-1}. Red dashed line indicates the position of laser spot.

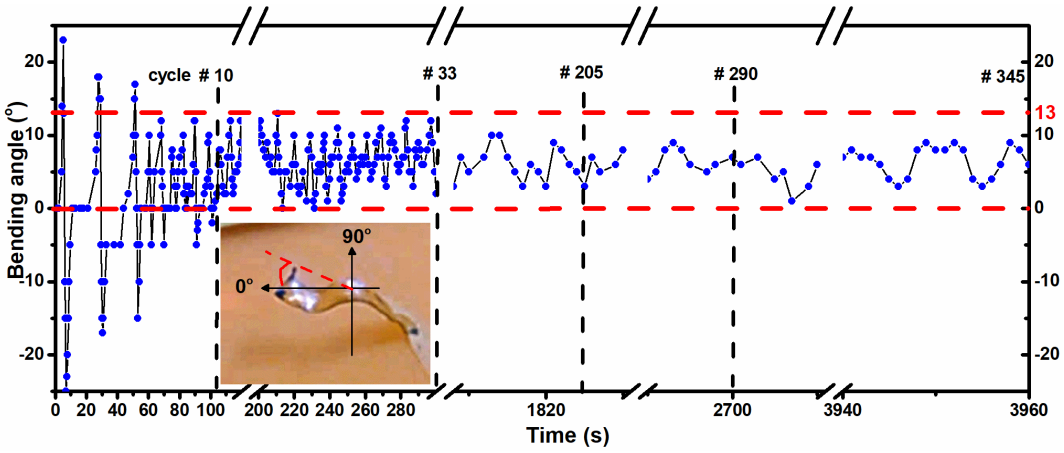

Figure S10. Bending angle of the autonomous arm (10 mm in length, cut from the scanned film conveyor 0.2 mm-UV20+90) as function of time of constant laser illumination. The grazing angle was 15° and the laser intensity was 1.4 W cm^{-2}. The inset picture shows the way to measure the bending angle, with the position at 0° being the initial position of the strip.

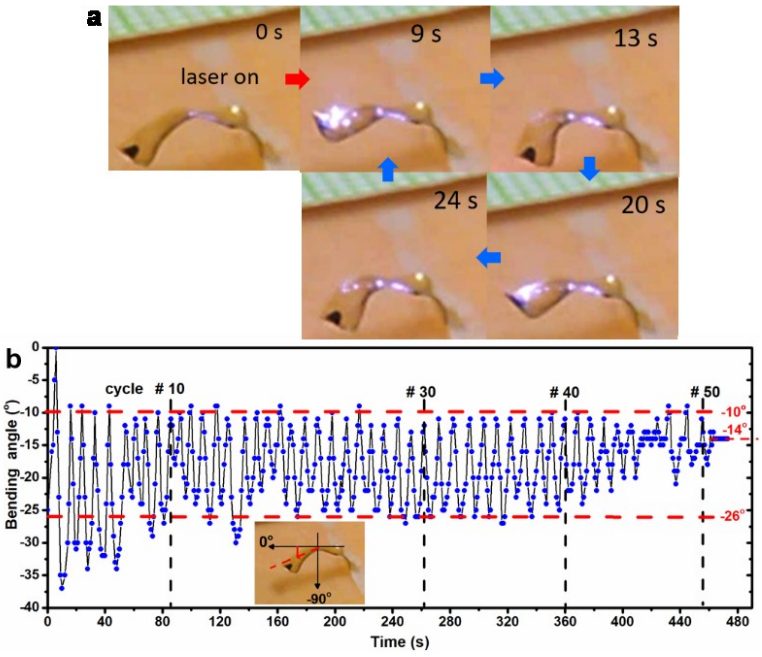

Figure S11. a) Autonomous motion of the strip actuator (10 mm in length, cut from a scanned film conveyor 0.2 mm-UV20+90) with time of constant laser illumination (3.9 W cm^{-2} in intensity) at a grazing angle of 15°. b) Bending angle as a function of time of laser illumination. Screenshots were taken from Movie S10.

The grazing angle was first set at 15° to investigate the effect of laser intensity on the autonomous motion of the prepared strip actuator. At lower laser intensity, as shown in Figure 5a and Figure S10, the mode of motion is upward-downward bending, in which the actuator bends upward first relative to the initial position (0°) because of non-uniform heating, with the actuating areas being near the surface, and then bends downward as the actuating areas propagate toward the bottom. The bending angle of the initial three cycles presents relatively large amplitude, which decays rapidly to smaller values with time. After 10 cycles of motion, only positive bending angles are observed. In fact, the motion is not 100 % bending, it is accompanied by slight twisting, which helps to deflect the strip away from light exposure so that self-shadowing can be established. Due to the softness of the material, the exposed areas of the strip may vary a little bit from cycle to cycle and the strip surface may reach the light path in asynchronous manner, causing slight twisting and fluctuation in bending angle. As time goes on, imperfection of LC transition in air may cause gradual decay of the bending angle. At the intensity of 1.4 W cm^{-2} and grazing angle of 15°, the autonomous motion lasts 345 cycles within 66 min and will continue if not stopped intentionally. In comparison, at higher laser intensity as shown in Figure S11, the bending amplitude is larger in average and the bending mode is downward-upward bending with positive bending angles being lost. The reason is that at higher intensity, the uniform heating is reached rapidly, leading to downward bending first as the bottom layer is the actuation domain. The downward-upward bending mode is relatively stable between the 10^{th} and the 40^{th} cycle, after which an obviously continued decay is observed due to insufficient cooling time. At the same grazing angle of 15° but higher intensity of 3.9 W cm^{-2}, this bending mode lasts 50 cycles in total within about 7 min, with the average speed of motion faster than that at lower laser intensity due to faster photothermal heating.

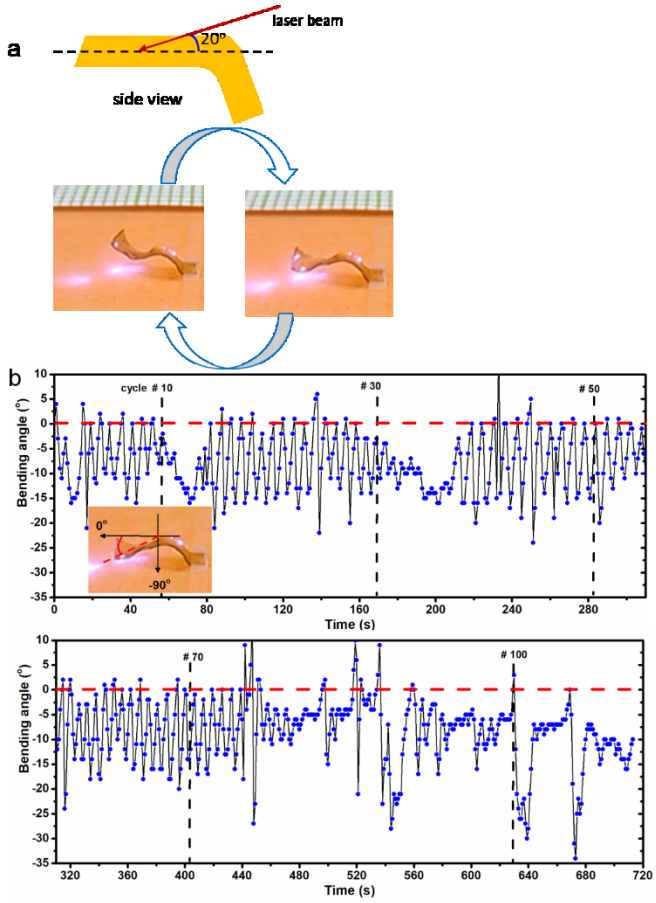

Figure S12. a) Autonomous motion of the strip actuator (10 mm in length, cut from a scanned film conveyor 0.2 mm-UV20+90) with time of constant laser illumination (1.4 W cm^{-2} in intensity) at grazing angle of 20°. b) Bending angle of the actuator as function of time of laser illumination. The strip was attached at one end to the substrate. Screenshots were taken from Movie S11.

With the same light intensity as in Figure 5a and Figure S10, the grazing angle was increased to 20° as shown in Figure S12a. At this larger grazing angle, the mode of autonomous motion is mainly downward-upward bending accompanied by small-amplitude twisting (Movie S11). The twisting is mainly observed during recovery to the initial position at 0°. During recovery, as the material is soft, the strip surface may reach the light path in asynchronous manner. In this case, one edge of the strip in the long axis direction reaches the light path earlier to be heated by the laser while the other edge, before reaching the laser path, is cooling and recovering toward the laser beam. The heated section

tends to bend downward while the section in cooling is unbending upward, producing a twisting motion. When uniform heating above T_{NI} is reached, the downward bending is regained. In this way, at a grazing angle of 20°, the mode of motion is mainly downward-upward bending accompanied by small-amplitude twisting. Within 12 min, about 110 cycles were achieved. The fluctuation in bending angle was large, which was caused by the accompanied twisting motion, while the decay and halt of bending were attributed to the thermal equilibrium reached finally.

As the grazing angle was decreased to 5°, the motion is quite random and complicated because the section exposable to light is longer and many different areas along the strip can be exposed to the laser beam. At constant laser illumination, the photothemo-mechano-thermal feedback loop was hardly established since the downward bending was impeded by the substrate and the strip was easily deflected away from the light path. When a hand-held slightly vibrating laser beam was applied, however, a self-shadowing effect was realized and the resulted snake-like or wave-like motion lasted 1 min (Movie S12).

When the grazing angle was maintained at 15° and the laser beam was rotated by 15° around the strip surface normal so that the projection of the laser beam on the strip surface was in 15° with the long axis of the strip (Figure 5b), a twisting mode of motion was achieved. In this mode, the strip was only partially irradiated by the laser in the width. The lower edge received light irradiation first and was bent toward the actuation domain, while the upper edge received little light and remain straight. As a result, the asymmetrical contraction in both the width and thickness directions contributed to the twisting motion. The twisting is 3D dynamic in space and difficult to be quantitatively analyzed. However, the twisting amplitude is large enough to be visualized and distinguished from other modes of motion (Movie S9).

Supporting Movie Captions

Movie S1. Light-guided moving of a bump from one end of the actuator strip to the other end reversibly.

Movie S2. Light-guided transportation of a carbon rod by the actuator prepared from sample 0.2 mm-UV20+60.

Movie S3. Light-guided transportation of a carbon rod by the actuator prepared from sample 0.4 mm-UV20+60.

Movie S4. A crawler capable of walking and turning to the left on a specific route under asymmetric scanning by laser.

Movie S5. The same crawler as in Movie S4 capable of walking and turning to the right under asymmetric scanning by laser.

Movie S6. A crawler capable of walking and turning for 180° under control of asymmetrical laser scanning.

Movie S7. A crawler capable of climbing an inclined surface under laser scanning.

Movie S8. Autonomous upward bending and downward bending of the actuator prepared from sample 0.2 mm-UV20+90.

Movie S9. Autonomous twisting motion of the actuator prepared from sample 0.2 mm-UV20+90.

Movie S10. Autonomous bending and unbending motion of the actuator prepared from sample 0.2 mm-UV20+90. The grazing angle was 15°, and the laser intensity was 3.9 W cm^{-2}.

Movie S11. Autonomous movement of the actuator prepared from sample 0.2 mm-UV20+90. The grazing angle was 20°, and the projection of the laser beam on the film surface was parallel with the long axis.

Movie S12. Autonomous 'snake-like' locomotion of the actuator prepared from sample 0.2 mm-UV20+90. The grazing angle was 5°, and a hand-held vibrating laser source was applied at an intensity of 1.4 W cm^{-2}.

Supporting References

[s1] R. Yang, Y. Zhao, *Angew. Chem.* **2017**, *129*, 14390-14394; *Angew. Chem. Int. Ed.* **2017**, *56*, 14202-14206.

[s2] K. Mebrouk, F. Camerel, O. Jeannin, B. Heinrich, B. Donnio, M. Fourmigue, *Inorg. Chem.* **2016**, *55*, 1296-1303.

3.4 Summary of the Project

In this study, we have used a single-layer LCE strip doped with an NIR dye to obtain an NIR light-controlled polymer actuator and demonstrated its multiple functions. The strip can be programmed by photocrosslinking in LC monodomain in one side and polydomain in the other side. When flattened with the monodomain side downward on a substrate and fixed at two ends, irradiating the strip with a 980 nm laser elicits a bump from the strip upon removal of the laser spot, resulting from polymer chain reorganization in isotropic state and subsequent cooling-induced disorder-order phase transition of the monodomain side. A rod-shape object put beside the bump can be transported forward step by step as the bump is scanned by the laser from end to end, mimicking the function of a conveyor belt. As the bump is cut off and set free, it can not only crawl straightly on both flat and inclined surfaces under uniform laser scanning, but also turn to the right, to the left and even along a “U” shape path controlled by asymmetric laser scanning that induces both in plane and out of plane deformations. The crawling speed increases with the laser intensity and the body length of the crawler within a certain range. With one end attached to the substrate and the other part suspended in air, the strip gives rise to multiple forms of autonomous motion under constant laser irradiation controlled at different incident angles with respect to the strip surface and the strip long axis. Up-and-down bending, twisting and combined autonomous motion have been enabled under a self shadowing mechanism. These achievements have further advanced the development of soft actuators based on LCEs.

CHAPTER 4. GENERAL DISCUSSION AND PERSPECTIVE

4.1 General Discussion

The research conducted in this thesis focuses on developing soft polymer actuators that convert thermal or light stimulus into mechanical energy through reversible actuation, which is based on an order–disorder phase transition. For optical actuators, crosslinked semicrystalline EVA and a main-chain LCP are the two primary polymeric materials used with addition of a small amount of light-absorbing and heat-generating agents. During programming, EVA has to be deformed in melted state followed by cooling constant strain to induce oriented crystallization along the deforming direction. The reversible actuation of EVA is based on the rSME, in which the aligned crystallites with higher T_m function as the solid confining framework, while the crystallites with lower T_m work as the active domain where melting and crystallization occur at light on and off states, respectively. For LCPs, in contrast, the mesogens are oriented in LC state and the alignment has to be locked in through chain crosslinking. It was reported by some studies that in free-standing state the reversible degree for LCPs can reach 400 % in microscale and 110 % at macroscopic scale (104, 160), driven by LC–isotropic phase transition. In the case of SCPs, the maximum value reported is 80% (71), but less than 20 % for EVA, induced by melting–crystallization transition. Generally, making full use of these soft actuators to achieve complicated shape changes or motions requires not only sophisticated programming procedures, but also a uniform heating and cooling as the on/off trigger. To this regard, a significant progress in our studies is that our projects have delicately taken advantage of asymmetric contraction/expansion of our easily programmed samples to amplify the actuation magnitude and complexity, simply using a laser beam or a heated substrate at constant temperature for actuation control. The asymmetric actuation can arise from either a temperature gradient generated in a uniformly programmed sample or from a nonuniformly programmed sample triggered by uniform stimulation. Laser is used in two of our projects and has enabled remote, local and precise control of the actuators with robust and multiple functions. In the third project, constant temperature actuation has rendered a smart autonomous motion. Our approaches and strategies have greatly contributed to the development of soft polymer actuators.

We have demonstrated in Chapter 1 that the melting–crystallization phase transition of aligned crystallites in EVA can be controlled by a gradient photothermal effect and leads to an optical

actuator capable of bending and unbending, which is tunable in magnitude and speed. As a commercialized polymeric elastomer, EVA is cheap in price and fast in crystallization, with the latter being an asset for rapid shape recovery. Moreover, the good mechanical property allows thick samples to be programmed by stretching. With the presence of AuNPs stabilized by modified EVA as ligands, it can be expected that the ligands on the surface of AuNPs may also be crosslinked with the matrix EVA during curing that further enhances the mechanical strength as well as the crosslinking density of the actuator and thus contributes to accelerating the optical actuation. In spite of the advantages, one obvious limitation is that during actuation, the laser intensity or power should be controlled such that T_{light} does not exceed $T_{m,high}$ in order to retain the reversibility. Above $T_{m,high}$, the skeleton crystallites are melted, which will lead to undirected crystallization during cooling and thus loss of the reversible actuation. Overheating is always a threat to this type of photoactuators as the photothermal effect is hard to be precisely controlled. Another potential limitation is the small force of actuation using laser, which only locally irradiates the actuator and induces a simple folding/unfolding motion like that of a hinge, although remote manipulation and localized actuation are available. Applying large light source like a flash torch or using a laser spot amplifier will not only expand the irradiated region to induce stronger actuation force, but also allow actuation of more complicated structures. Despite the fact that the laser intensity in use is relatively high compared with natural sunlight, adding more light-absorbing and heat-generating additives may alleviate this issue. For a pristine EVA strip with uniaxially aligned crystallites, a temperature gradient is readily created across the thickness by placing the strip on a substrate at constant temperature, and this establishes a thermal (melting)-mechano (asymmetric MIC and CIE)-thermal (crystallization) feedback loop that drives the autonomous up-and-down motion without externally controlled on/off switching of the temperature. This achievement has been presented in Chapter 2. The autonomous motion is hour-long and can be used to directly convert thermal energy into mechanical energy continuously. One of the prominent strengths of the autonomous actuator is that the motion is self-sustained; it needs no complicated devices or programs to control the temperature increase/decrease. The preparation of the actuator is simple and convenient, with the only need of stretching a crosslinked strip in melted state, followed by a cooling under constant strain. Besides, the repetitive motion is reminiscent of living systems and thus remain valuable for preparation of biomimetic devices. It is worth mentioning that the displacement in the horizontal direction along the substrate also deserves utilization.

Through a facile design, it is possible to prepare smart robots that can work automatically on an isothermal plate. The decay of the oscillation over time and the eventually halted oscillation remain an unsolved issue. The amplitude decreases gradually with time and comes to zero finally. Should there be a perfect match between the contractile force during melting and the expansion force during cooling in each cycle, and the frictional forces at the two ends of the actuator do not change, the oscillation may last perpetually with an almost constant amplitude.

A primary concern for SCPs is still the trick that the maximum T_m should not be exceeded, while for LCPs this is not an issue. The uniform crosslinking and uniaxial alignment of SCPs also greatly restrict the complexity of the reversible actuation. The thermo-mechano-thermal feedback loop concept demonstrated here can be extended to other materials like LCPs (147) and bilayers with different coefficients of thermal expansion (161). Given a coating layer containing appropriate photothermal agent, it is possible to carry out the autonomous motion on the substrate layer under constant light illumination, thus indirectly turning light energy into mechanical energy. If the actuator is integrated with a piezoelectric material, it may also produce electricity from either thermal or light energy benefiting from the autonomous motion.

The order–disorder phase transition of LCPs is in fact LC–isotropic transition, which is usually faster than the 3D melting–crystallization transition for many SCPs. Conventional LCP-based actuators are also uniaxially aligned and uniformly crosslinked, giving rise to simple contraction/expansion. As photocrosslinkable LC monomers emerge and new LC alignment techniques are developed, complex director profiles are generated and bring LCP-based actuators with diverse reversible actuation behaviors and functions. Although multifunctionality will bring actuators a step closer to artificial intelligence, few works have been done on developing multifunctional LCP-based actuators. We have obtained such a monolithic multifunctional actuator controllable by an NIR laser. The actuator is a single-layer, dye-doped LCE strip nonuniformly crosslinked. The dye generates heat through non-radiative emission after NIR light absorption, with its photothermal conversion efficiency higher than some gold nanostructures and close to polydopamine nanoparticles. With two ends fixed and the monodomain side set downward, the strip behaves as a light-guided conveyor capable of transporting rod-like objects. With two ends free, the strip turns into a flexible crawler bearing ability of walking, climbing and turning in locomotion under uniform or asymmetric laser scanning. When suspended in air, the arm-like strip

is capable of bending, twisting and biomimetic autonomous motions under constant laser illumination. Thanks to the incorporation of UV-crosslinkable cinnamyl moieties and the attenuation of UV light penetration, the LCEs affords non-uniform crosslinking of the oriented monodomain so that the active domains can be selectively distributed in the finally crosslinked actuator, causing non-uniform deformations during actuation. This shows that the used LCEs are superior to EVA and many other LCPs in terms of structured and complex actuation. In addition, the alignment of our LCPs is associated with plastic flow induced by mechanical stretching, which makes it easier to produce thicker and larger strips than using surface alignment methods. The softness of the LCEs is another advantage in terms of potential application as biomimetic robots and biomedical implants. A potential issue our LCEs are facing is the stability of the doped dye. After over 100 times of laser scanning or autonomous motion under constant laser illumination for over an hour, the photothermal effect is not affected even though the autonomous motions ceases, which is caused by the loss of self-shadowing effect due to the balance between the viscoelasticity and the elasticity of the material during constant light illumination. But in the long run, potential risks of migration and degradation of the physically incorporated additives are unknown. To reduce the risks, the dye can also be functionalized with reactive groups to covalently immobilize the chromophores during polymerization so that the dye is resistant to migration. The laser-driven autonomous motions are slower in speed compared with the autonomous motion of EVA and the oscillation of other LCN-based actuators, probably due to the remained slight degree of mesogen order in the polydomain that is caused by the crosslinking density gradient in the thickeness direction of the strip. As light falls on the superficial layer, the polydomain tends to bend upward first. However, as heat diffuses downward the monodomain layer contracts and bends the strip downward. The competition between the two domains slows down a cycle of bending/unbending or twisting. The slow autonomous motion may find application in situations where low frequency of oscillation is needed. Considering the softness and the numerous functions of LCE actuators, potential applications in haptic devices, wearable products and even biomedical devices are very attractive and promising. An obstacle to these applications is the high temperature at which these functions come into effect, i.e. the order–disorder phase transition temperature is too high, usually above body temperature (T_{bd}). Therefore, it remains meaningful to find approaches to lowering the LC–isotropic transition temperature of LCEs and make the actuation triggerable at T_{bd}. This future study will be described briefly in the following section.

4.2 Future Studies

4.2.1 Solar light-driven Autonomous Motion on a Substrate for Light-to-Heat Energy Conversion

The autonomous motion of the EVA actuators is based on melting–crystallization thermal phase transition and driven by the thermo-mechano-thermal feedback loop. Thermal energy is drawn from the hot substrate and converted to the jump/descent motion continuously as long as the substrate temperature is maintained constant. This robust function can be used to collect thermal energy dissipated from industrial production and output mechanical energy at a relatively low efficiency. However, a source of thermal energy needs to be provided wherever the autonomous motion is carried out. Inspired by the photothermal effect of AuNPs, it can be envisioned that given an appropriate substrate capable of absorbing sunlight and releasing heat to raise the substrate temperature high enough to melt partial EVA crystallites, the autonomous motion would be also attainable using EVA strips. Our previous results have validated that the surface temperature T_{surf} of the substrate should be around 75 ℃ to attain the hour-long motion. However, at the sunlight intensity level, AuNPs have rarely been reported to enable such a high temperature in spite of their high extinction coefficient. In addition, AuNPs abosorb mostly light with wavelength matching their SPR band, thus solar light is not fully utilized. In contrast, graphene and CNTs absorb light spanning from UV to NIR region due to the conjugated chemical structure and are proved to be outstanding photothermal agents. The rGO/CNTs photothermal layer can be prepared by virtue of vacuum filtration of the mixed solution through a commercial PVDF membrane. Benefiting from the similar network structure and the π-π interaction, rGO and CNTs easily form a compatible and compact layer, of which the surface temperature can reach as high as 78 ℃ at only one-sun level of light intensity (162). The strong photothermal effect is promising to drive the autonomous motion of an aligned EVA strip placed on the rGO/CNTs photothermal layer under sunlight illumination. By laminating EVA and a piezoelectric material (e.g. PVDF), the bilayer structure may also produce electric signal arising from the autonomous bending-unbending motion, thereby indirectly converting solar energy into electrical energy. By extending the thermo-mechano-thermal feedback loop to photothermal-mechano-thermal feedback loop, the simple combination of SCPs with a light-to-heat generating substrate opens an avenue for making better use of solar energy to produce mechanical energy as well as electrical energy.

4.2.2 LCE Actuators Working between Body Temperature and Room Temperature

Few studies have reported LCP-based actuators displaying reversible actuation between T_{bd} and RT as most LCPs have a high T_{iso}, which greatly restricts the application for biomedical purposes. LCP materials with T_{iso} between RT and T_{bd} can be actuated inside human body and recovered when taken outside. This behavior may lead to biomedical devices that work spontaneously at the ambient temperature within body with no need of direct or indirect heating that may burn the tissues. More interestingly, if the actuation can be activated by contact with human fingers at around 32 ℃ and recovered without contact, it will be promising to make haptic or anti-counterfeiting devices that allow manipulation or actuation of the actuator with a finger, which makes the operation very convenient. Our previous results presented in Chapter 3 have showcased the softness of the used LCEs which have T_g at around RT and T_{NI} around 55 ℃ which is much higher than T_{bd}. Fortunately, it has been proved that the incorporation of non-mesogenic monomers can effectively decrease the T_{iso} of LCPs (114). Since the LCEs are polyesters synthesized by polycondensation, a functionalized non-mesogenic monomer can be easily introduced as comonomer to tune the T_{iso} of the final copolymer. We choose to use the non-mesogenic monomer (BHPBZ, provided by Dr. Franck Camerel) as depicted in Scheme 1 for two reasons. One is the good compatibility between benzil group and all the other monomers, and the other is the flexible long spacers attached at the two ends to retain the softness of the material. The hindering effect stemming from the out-of-plane configuration of the core benzil group and the dilution effect will greatly weaken the LC formation and decrease the T_{iso} effectively, likely giving rise to a temperature close to that within or on the skin of human body. Using the same programming method by stretching the prepared LCE strip followed by crosslinking through the UV light-induced dimerization of the cinnamyl groups, crosslinked monodomain can be obtained to endow the LCE actuator with reversible actuation capability. Indeed, our preliminary experimental results in Figure 18a have shown that with increase of the BHPBZ content, T_{NI} of the resulted LCPs can be decreased from 50.4 ℃ to 33 ℃. By crosslinking the LCP (synthesized at the monomer molar ratio of x : y : z = 65 : 20 : 15) in monodomain for different times at two sides, the obtained LCE is capable of gradual bending during heating from 18 ℃ to 41 ℃, as shown in Figure 18b, and unbending upon cooling back, as a result of asymmetric contraction in isotropic state and expansion in LC state, respectively. The curvature at 37 ℃ is large and the flat shape is almost completely recovered at 18 ℃. The large-magnitude response within the above temperature range

makes the synthesized LCEs potential candidates for practical applications in orthodontic devices as well as haptic materials. If embedded or integrated with a piezoelectric material, the LCE might convert the sensed body temperature into mechanical motion and further transduce the motion into electrical signal, making the device work as a sensor or detector.

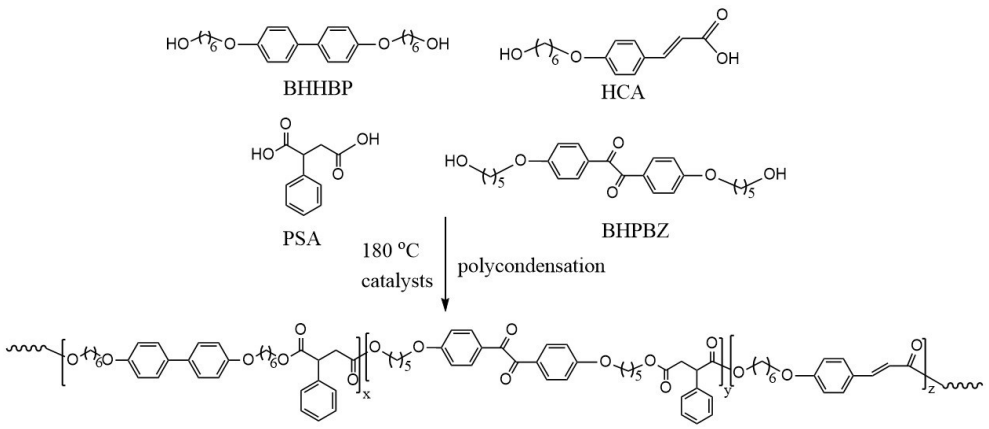

Scheme 1. Synthetic route of an LCE through polycondensation from monomers 4,4'-bis(6-hydroxyhexyloxy) biphenyl (BHHBP), phenylsuccinic acid (PSA), 4-(6-hydroxyhexyloxy) cinnamic acid (HCA) and 4,4'-bis(5-hydroxypentyloxy) benzil (BHPBZ).

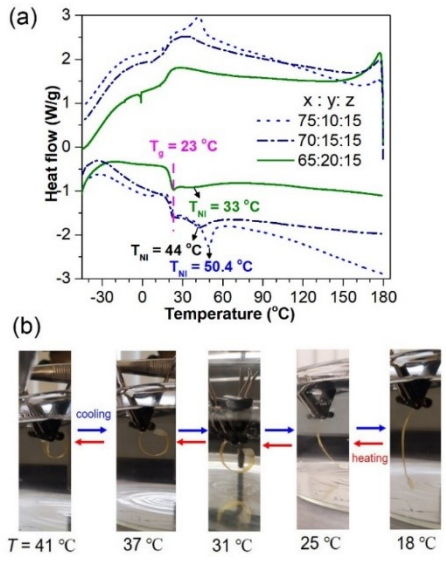

Figure 18. (a) DSC curves of the synthesized LCEs at different monomer ratios. (b) An LCE strip (synthesized from feeding molar ratio x : y : z = 65 : 20 : 15) crosslinked nonuniformly at two sides in monodomain showing reversible bending and unbending actuation between 18 °C and 41°C.

4.2.3 Anisotropic LCP-Based Adhesive as Active Actuation Domains

So far, most of the polymer actuators based on LCPs have been constructed from a monolithic film with a uniform or heterogeneous director profile of mesogens, while the others are made from bilayers (163) or even trilayers (164) with anisotropic LCP layer as the active actuation domain. The usage of single material obviates the assembling procedure required in preparing layered structures, but the programming process necessary for building the distribution of the internal mesogenic order can be tedious and more complicated. Most of all, the single LCP developed may not meet all requirements for application in different fields in terms of the material mechanical property, available stimuli, biocompatibility, degradability and so on, thus new LCP for specific application purposes will need to be designed and synthesized, which consumes time and efforts. Conventional LCP-based bilayer actuators need a sticky tape to be attached with the oriented LCP layer. The tape is the passive layer which bends or curls as the LCP layer undergoing order-disorder transition under stimulation. However, the useful tapes are limited in number and materials properties. Now, imaging that an LCP is sticky and able to be oriented into monodomain, then several individual parts of the same or different materials can be combined into one integrated structure through adhesion with the oriented LCP adhesive, resulting in assembled actuators capable of reversible actuation driven by the order–disorder phase transition of the LCP. Considering that the adhesion mechanism can be based on mechanical interlocking, covalent bonding, interfacial diffusion, hydrogen bonding and electrostatic interaction (165), numerous materials can be integrated into an actuator under one of the above principles using the anisotropic LCP adhesive. In fact, our synthesized LCP in the above section is a promising candidate for the adhesive. The T_{NI} can be tuned to be around 33 °C, which is easily reached by slight heating. During cooling from isotropic state at the temperature several degrees higher than T_{NI}, the viscosity of the LCP material is relatively low and oriented monodomain can be induced by extrusion from a syringe or a 3D printer on the selected passive material, leading to adhesion between the materials as well as orientation of mesogens. The aligned LCP in monodomain can be fixed by dimerization induced crosslinking under UV light illumination. Figure 19a shows a simple combination between two parts by the anisotropic LCP adhesive with the mesogen orientation along the long axis. In isotropic state, the contraction of the LCP may induce folding as Figure 19a-ii shows. By assembling several parts into one structure in symmetric (Figure 19b) or asymmetric (Figure 19c)

manners with or without assistance of origami-kirigami technique, complex shape changes as well as directional motions driven by LC order-to-isotropic disorder phase transition can be expected.

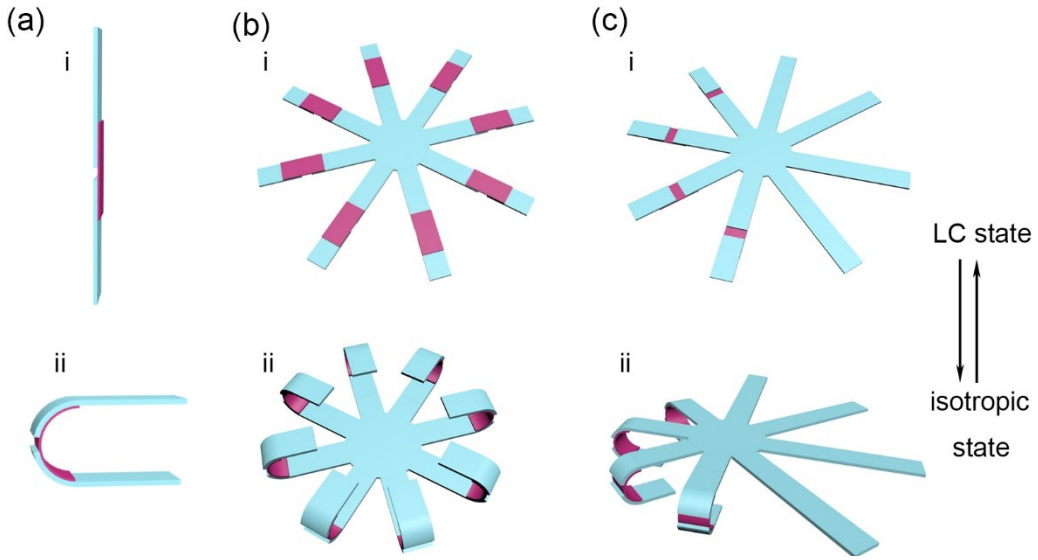

Figure 19. Schematic illustration of assembled actuators based on anisotropic LCP adhesive and passive materials, and the reversible actuation. (a) Two strips connected by the oriented LCP adhesive in LC state (i) and folding of the actuator activated in isotropic state (ii). (b) Symmetric assembly and (c) asymmetric assembly of actuators using the active LCP adhesive and inactive materials. Actuators are in LC state in row i and isotropic stage in row ii, respectively. Red, active LCP actuation domains. Light blue, inactive strips. The LCP adhesive is in the upper layer in Figure 19b and in the bottom layer in Figure 19c, respectively.

CONCLUSIONS

In this thesis, three research works have been conducted on the design, preparation and development of soft polymer actuators with the ability of thermal- and/or light-regulated reversible actuation, which are based on order-disorder phase transitions. Semicrystalline polymer EVA was chosen as the material in the first two projects for constructing two types of polymer actuators, respectively, both of which are dependent on the rSME of EVA. In Chapter 1, we showed that by loading a small amount of AuNPs into crosslinked EVA with uniaxially oriented crystallites, an optical actuator capable of reversible bending and unbending under on/off control of a 532 nm laser can be obtained. The bending is induced by a temperature gradient across the thickness of the strip. Our systematic study revealed that the reversible actuation is tunable in both magnitude and speed by varying the laser intensity, content of AuNPs, the specimen elongation and the thickness. The second type of polymer actuators presented in Chapter 2 are based on pure EVA and capable of autonomous bending and unbending oscillation on a substrate of constant temperature with no need of on/off temperature switching. A temperature gradient is generated from the bottom to the surface of the strip and activates the non-uniform contraction, inducing an arch shape which then expands due to directed crystallization and falls back to the substrate surface to reactivate the cycle. The continuous motion is guaranteed by a deftly established thermo-mechano-thermal feedback loop. The amplitude and period of the oscillation is related to the substrate temperature, the strip elongation and the sample thickness. It was revealed that the jumping amplitude increases with the substrate surface temperature and the strip elongation while it hardly changes with the strip thickness. Large elongation shortens the period and durability of the oscillation, and the durability decreases with increasing the strip thickness. The autonomous motion can last hour-long for 800–1000 cycles when the substrate temperature lies between 70–85 °C, below which the durability is much decayed. The autonomous motion can convert thermal energy into mechanical energy in forms of self-walking and driving the rotation of a model wheel. In Chapter 3, we demonstrated that by doping an LCE strip with a small fraction of an NIR dye and crosslinking the strip non-uniformly from two sides, a single-layer multifunctional actuator capable of laser-guided transportation, turning in walking direction and versatile autonomous motions can be achieved. The light-guided transportation stems from the laser irradiation-induced bump which propagates with the scanning laser and pushes forward a rod-shape object. The speed of locomotion increases with the laser intensity and the body length of the strip. By

unsymmetrically scanning the cut bump cross the width direction, both in-plane contraction and out-of-plane bending induces the direction turning. By adjusting the incident laser direction with respect to the actuator surface or applying slight vibration to the laser, the modes of autonomous motion alters as well, ranging from bending, twisting to worm-like rocking motions.

In conclusion, our research works have contributed significantly to the advancement of knowledge in the field of soft polymer actuators by developing robust optical actuators and thermal actuators driven by order-disorder phase transitions. Our approaches are simple, universal and robust. They can be extended to many other materials not restricted to SCPs and LCPs for exploitation of new functions, properties and applications.

BIBLIOGRAPHY

1 Zupan, M.; Ashby, M. F.; Fleck, N. A., *Adv. Eng. Mater.* **2002,** *4*, 933-940.

2 Wei, M.; Gao, Y.; Li, X.; Serpe, M. J., *Polym. Chem.* **2017,** *8*, 127-143.

3 Lendlein, A.; Kelch, S., *Angew. Chem. Int. Ed.* **2002,** *41*, 2034-2057.

4 Romasanta, L. J.; Lopez-Manchado, M. A.; Verdejo, R., *Prog. Polym. Sci.* **2015,** *51*, 188-211.

5 Li, H.; Go, G.; Ko, S. Y.; Park, J.-O.; Park, S., *Smart Mater. Struct.* **2016,** *25*, 027001.

6 Gong, J.; Lin, H.; Dunlop, J. W. C.; Yuan, J., *Adv. Mater.* **2017,** *29*, 1605103.

7 Treml, B. E.; McKenzie, R. N.; Buskohl, P.; Wang, D.; Kuhn, M.; Tan, L. S.; Vaia, R. A., *Adv. Mater.* **2018,** *30*, 1705616.

8 Leeladhar; Singh, J. P., *ACS Appl. Mater. Interfaces* **2018,** *10*, 33956-33965.

9 Lan, R.; Sun, J.; Shen, C.; Huang, R.; Zhang, L.; Yang, H., *Adv. Funct. Mater.* **2019**, *29*, 1900013.

10 Erb, R. M.; Martin, J. J.; Soheilian, R.; Pan, C.; Barber, J. R., *Adv. Funct. Mater.* **2016,** *26*, 3859-3880.

11 Wang, L.; Razzaq, M. Y.; Rudolph, T.; Heuchel, M.; Nöchel, U.; Mansfeld, U.; Jiang, Y.; Gould, O. E. C.; Behl, M.; Kratz, K.; Lendlein, A., *Mater. Horiz.* **2018,** *5*, 861-867.

12 White, T. J., *J. Polym. Sci. Polym. Phys.* **2012,** *50*, 877-880.

13 Zeng, H.; Wasylczyk, P.; Wiersma, D. S.; Priimagi, A., *Adv. Mater.* **2018,** *30*, 1703554.

14 Geryak, R.; Tsukruk, V. V., *Soft Matter* **2014,** *10*, 1246-1263.

15 Ionov, L., *Langmuir* **2015,** *31*, 5015-5024.

16 Shepherd, R. F.; Ilievski, F.; Choi, W.; Morin, S. A.; Stokes, A. A.; Mazzeo, A. D.; Chen, X.; Wang, M.; Whitesides, G. M., *Proc. Natl. Acad. Sci. U. S. A.* **2011,** *108*, 20400-20403.

17 Wang, W.; Xiang, C.; Liu, Q.; Li, M.; Zhong, W.; Yan, K.; Wang, D., *J. Mater. Chem. A* **2018,** *6*, 22599-22608.

18 Zhang, L.; Chizhik, S.; Wen, Y.; Naumov, P., *Adv. Funct. Mater.* **2016,** *26*, 1040-1053.

19 Zhang, Y.; Liao, J.; Wang, T.; Sun, W.; Tong, Z., *Adv. Funct. Mater.* **2018**, *28*, 1707245.

20 Shang, Y.; Liu, J.; Zhang, M.; He, W.; Cao, X.; Wang, J.; Ikeda, T.; Jiang, L., *Soft Matter* **2018,** *14*, 5547-5553.

21 Lin, H.; Zhang, S.; Xiao, Y.; Zhang, C.; Zhu, J.; Dunlop, J. W. C.; Yuan, J., *Macromol. Rapid Commun.* **2019,** *40*, 1800896.

22 Nakahata, M.; Takashima, Y.; Hashidzume, A.; Harada, A., *Angew. Chem. Int. Ed.* **2013,** *52*, 5731-5735.

23 Maeda, S.; Hara, Y.; Sakai, T.; Yoshida, R.; Hashimoto, S., *Adv. Mater.* **2007,** *19*, 3480-3484.

24 White, B. T.; Long, T. E., *Macromol. Rapid Commun.* **2019,** *40*, 1800521.

25 Li, Q.; Liu, C.; Lin, Y.-H.; Liu, L.; Jiang, K.; Fan, S., *ACS Nano* **2015,** *9*, 409-418.

26 Sang, W.; Zhao, L.; Tang, R.; Wu, Y.; Zhu, C.; Liu, J., *Macromol. Mater. Eng.* **2017,** *302*, 1700239.

27 Hu, W.; Lum, G. Z.; Mastrangeli, M.; Sitti, M., *Nature* **2018,** *554*, 81-85.

28 Kim, Y.; Yuk, H.; Zhao, R.; Chester, S. A.; Zhao, X., *Nature* **2018,** *558*, 274-279.

29 Yu, H.; Ikeda, T., *Adv. Mater.* **2011,** *23*, 2149-2180.

30 Pelrine, R.; Kornbluh, R.; Pei, Q.; Joseph, J., *Science* **2000,** *287*, 836.

31 Kim, O.; Kim, S. J.; Park, M. J., *Chem. Commun.* **2018,** *54*, 4895-4904.

32 Hines, L.; Petersen, K.; Lum, G. Z.; Sitti, M., *Adv. Mater.* **2017,** *29*, 1603483.

33 Brochu, P.; Pei, Q., *Macromol. Rapid Commun.* **2010,** *31*, 10-36.

34 Shankar, R.; Ghosh, T. K.; Spontak, R. J., *Soft Matter* **2007,** *3*, 1116-1129.

35 Qiu, Y.; Zhang, E.; Plamthottam, R.; Pei, Q., *Acc. Chem. Res.* **2019,** *52*, 316-325.

36 Pelrine, R.; Kornbluh, R.; Joseph, J.; Heydt, R.; Pei, Q.; Chiba, S., *Mater. Sci. Eng. C* **2000,** *11*, 89-100.

37 Biggs, J.; Danielmeier, K.; Hitzbleck, J.; Krause, J.; Kridl, T.; Nowak, S.; Orselli, E.; Quan, X.; Schapeler, D.; Sutherland, W.; Wagner, J., *Angew. Chem. Int. Ed.* **2013,** *52*, 9409-9421.

38 Vatankhah-Varnoosfaderani, M.; Daniel, W. F. M.; Zhushma, A. P.; Li, Q.; Morgan, B. J.; Matyjaszewski, K.; Armstrong, D. P.; Spontak, R. J.; Dobrynin, A. V.; Sheiko, S. S., *Adv. Mater.* **2017,** *29*, 1604209.

39 Armstrong, D. P.; Spontak, R. J., *Adv. Funct. Mater.* **2018**, *28*, 1803467.

40 Inal, S.; Rivnay, J.; Suiu, A. O.; Malliaras, G. G.; McCulloch, I., *Acc. Chem. Res.* **2018,** *51*, 1368-1376.

41 Huang, L.; Jiang, R.; Wu, J.; Song, J.; Bai, H.; Li, B.; Zhao, Q.; Xie, T., *Adv. Mater.* **2017,** *29*, 1605390.

42 Kim, J.; Hanna, J. A.; Byun, M.; Santangelo, C. D.; Hayward, R. C., *Science* **2012,** *335*, 1201-1205.

43 Wang, E.; Desai, M. S.; Lee, S. W., *Nano Lett.* **2013,** *13*, 2826-2830.

44 Lee, E.; Kim, D.; Kim, H.; Yoon, J., *Sci. Rep.* **2015,** *5*, 15124.

45 Kim, D.; Kim, H.; Lee, E.; Jin, K. S.; Yoon, J., *Chem. Mater.* **2016,** *28*, 8807-8814.

46 Shang, J.; Le, X.; Zhang, J.; Chen, T.; Theato, P., *Polym. Chem.* **2019,** *10*, 1036-1055.

47 Shang, J.; Theato, P., *Soft Matter* **2018,** *14*, 8401-8407.

48 Hu, Y.; Kahn, J. S.; Guo, W.; Huang, F.; Fadeev, M.; Harries, D.; Willner, I., *J. Am. Chem. Soc.* **2016,** *138*, 16112-16119.

49 Zhang, X.; Pint, C. L.; Lee, M. H.; Schubert, B. E.; Jamshidi, A.; Takei, K.; Ko, H.; Gillies, A.; Bardhan, R.; Urban, J. J.; Wu, M.; Fearing, R.; Javey, A., *Nano Lett.* **2011,** *11*, 3239-3244.

50 Zheng, W. J.; An, N.; Yang, J. H.; Zhou, J.; Chen, Y. M., *ACS Appl. Mater. Interfaces* **2015,** *7*, 1758-1764.

51 Hu, Y.; Liu, J.; Chang, L.; Yang, L.; Xu, A.; Qi, K.; Lu, P.; Wu, G.; Chen, W.; Wu, Y., *Adv. Funct. Mater.* **2017,** *27*, 1704388.

52 Deng, J.; Li, J.; Chen, P.; Fang, X.; Sun, X.; Jiang, Y.; Weng, W.; Wang, B.; Peng, H., *J. Am. Chem. Soc.* **2016,** *138*, 225-230.

53 Kohlmeyer, R. R.; Chen, J., *Angew. Chem. Int. Ed.* **2013,** *52*, 9234-9237.

54 Zhang, X.; Yu, Z.; Wang, C.; Zarrouk, D.; Seo, J. W.; Cheng, J. C.; Buchan, A. D.; Takei, K.; Zhao, Y.; Ager, J. W.; Zhang, J.; Hettick, M.; Hersam, M. C.; Pisano, A. P.; Fearing, R. S.; Javey, A., *Nat. Commun.* **2014,** *5*, 2983.

55 Hu, Y.; Wu, G.; Lan, T.; Zhao, J.; Liu, Y.; Chen, W., *Adv. Mater.* **2015,** *27*, 7867-7873.

56 Li, X.; Cai, X.; Gao, Y.; Serpe, M. J., *J. Mater. Chem. B* **2017,** *5*, 2804-2812.

57 Sun, P.; Zhang, H.; Xu, D.; Wang, Z.; Wang, L.; Gao, G.; Hossain, G.; Wu, J.; Wang, R.; Fu, J., *J. Mater. Chem. B* **2019,** *7*, 2619-2625.

58 Zhang, L.; Qiu, X.; Yuan, Y.; Zhang, T., *ACS Appl. Mater. Interfaces* **2017,** *9*, 41599-41606.

59 Hu, J.; Zhu, Y.; Huang, H.; Lu, J., *Prog. Polym. Sci.* **2012,** *37*, 1720-1763.

60 Zhou, J.; Sheiko, S. S., *J. Polym. Sci. Polym. Phys.* **2016,** *54*, 1365-1380.

61 Mandelkern, L.; Roberts, D. E.; Diorio, A. F.; Posner, A. S., *J. Am. Chem. Soc.* **1959,** *81*, 4148-4157.

62 Zotzmann, J.; Behl, M.; Hofmann, D.; Lendlein, A., *Adv. Mater.* **2010,** *22*, 3424-3429.

63 Chung, T.; Romo-Uribe, A.; Mather, P. T., *Macromolecules* **2008,** *41*, 184-192.

64 Kuang, W.; Mather, P. T., *Polymer* **2018,** *156*, 228-239.

65 Bothe, M.; Pretsch, T., *Macro. Chem. Phys.* **2012,** *213*, 2378-2385.

66 Hong, S. J.; Yu, W.-R.; Youk, J. H., *Smart Mater. Struct.* **2010,** *19*, 035022.

67 Li, J.; Rodgers, W. R.; Xie, T., *Polymer* **2011,** *52*, 5320-5325.

68 Behl, M.; Kratz, K.; Zotzmann, J.; Nochel, U.; Lendlein, A., *Adv. Mater.* **2013,** *25*, 4466-4469.

69 Behl, M.; Kratz, K.; Noechel, U.; Sauter, T.; Lendlein, A., *Proc. Natl. Acad. Sci. U. S. A.* **2013,** *110*, 12555-12559.

70 Wu, X.; Huang, W.; Zhao, Y.; Ding, Z.; Tang, C.; Zhang, J., *Polymers* **2013,** *5*, 1169-1202.

71 Li, Q.; Zhou, J.; Vatankhah-Varnoosfaderani, M.; Nykypanchuk, D.; Gang, O.; Sheiko, S. S., *Macromolecules* **2016,** *49*, 1383-1391.

72 Zharinova, E.; Heuchel, M.; Weigel, T.; Gerber, D.; Kratz, K.; Lendlein, A., *Polymers* **2016,** *8*, 412.

73 Dolynchuk, O.; Kolesov, I.; Jehnichen, D.; Reuter, U.; Radusch, H.-J.; Sommer, J.-U., *Macromolecules* **2017,** *50*, 3841-3854.

74 Meng, Y.; Jiang, J.; Anthamatten, M., *ACS Macro Lett.* **2015,** *4*, 115-118.

75 Lu, L.; Cao, J.; Li, G., *Sci. Rep.* **2018,** *8*, 14233.

76 Kolesov, I.; Dolynchuk, O.; Borreck, S.; Radusch, H.-J., *Polym. Adv. Technol.* **2014,** *25*, 1315-1322.

77 Farhan, M.; Rudolph, T.; Nochel, U.; Yan, W.; Kratz, K.; Lendlein, A., *ACS Appl. Mater. Interfaces* **2017,** *9*, 33559-33564.

78 Yang, G.; Liu, X.; Tok, A. I. Y.; Lipik, V., *Polym. Chem.* **2017,** *8*, 3833-3840.

79 Stroganov, V.; Al-Hussein, M.; Sommer, J. U.; Janke, A.; Zakharchenko, S.; Ionov, L., *Nano Lett.* **2015,** *15*, 1786-1790.

80 Lu, L.; Li, G., *ACS Appl. Mater. Interfaces* **2016,** *8*, 14812-14823.

81 Bothe, M.; Pretsch, T., *J. Mater. Chem. A* **2013,** *1*, 14491-14497.

82 Gao, Y.; Liu, W.; Zhu, S., *ACS Appl. Mater. Interfaces* **2017,** *9*, 4882-4889.

83 Peterson, G. I.; Dobrynin, A. V.; Becker, M. L., *Adv. Healthcare Mater.* **2017,** *6*, 1700694.

84 Gong, T.; Zhao, K.; Wang, W.; Chen, H.; Wang, L.; Zhou, S., *J. Mater. Chem. B* **2014,** *2*, 6855-6866.

85 Kularatne, R. S.; Kim, H.; Boothby, J. M.; Ware, T. H., *J. Polym. Sci. Polym. Phys.* **2017,** *55*, 395-411.

86 Beyer, P.; Braun, L.; Zentel, R., *Macromol. Chem. Phys.* **2007,** *208*, 2439-2448.

87 Beyer, P.; Terentjev, E. M.; Zentel, R., *Macromol. Rapid Commun.* **2007,** *28*, 1485-1490.

88 Krause, S.; Dersch, R.; Wendorff, J. H.; Finkelmann, H., *Macromol. Rapid Commun.* **2007,** *28*, 2062-2068.

89 Yang, R.; Chen, L.; Ruan, C.; Zhong, H.-Y.; Wang, Y.-Z., *J. Mater. Chem. C* **2014,** *2*, 6155-6164.

90 Deng, L.-L.; Guo, L.-X.; Lin, B.-P.; Zhang, X.-Q.; Sun, Y.; Yang, H., *Polym. Chem.* **2016,** *7*, 5265-5272.

91 Kim, D.-Y.; Shin, S.; Yoon, W.-J.; Choi, Y.-J.; Hwang, J.-K.; Kim, J.-S.; Lee, C.-R.; Choi, T.-L.; Jeong, K.-U., *Adv. Funct. Mater.* **2017,** *27*, 1606294.

92 Zhang, Z.-Y.; Zhang, Q.-K.; Shen, Z.; Yu, J.-P.; Wu, Y.-X.; Fan, X.-H., *Macromolecules* **2016,** *49*, 475-482.

93 Finkelmann, H.; Kock, H.-J.; Rehage, G., *Makromol. Chem., Rapid Commun.* **1981,** *2*, 317-322.

94 Küpfer, J.; Finkelmann, H., *Makromol. Chem., Rapid Commun.* **1991,** *12*, 717-726.

95 Fridrikh, S. V.; Terentjev, E. M., *Phys. Rev. E* **1999,** *60*, 1847-1857.

96 Jiang, H.; Li, C.; Huang, X., *Nanoscale* **2013,** *5*, 5225-5240.

97 Finkelmann, H.; Nishikawa, E.; Pereira, G. G.; Warner, M., *Phys. Rev. Lett.* **2001,** *87*, 015501.

98 Bisoyi, H. K.; Li, Q., *Chem. Rev.* **2016,** *116*, 15089-15166.

99 Ikeda, T.; Mamiya, J.; Yu, Y., *Angew. Chem. Int. Ed.* **2007,** *46*, 506-528.

100 Liu, W.; Guo, L.-X.; Lin, B.-P.; Zhang, X.-Q.; Sun, Y.; Yang, H., *Macromolecules* **2016,** *49*, 4023-4030.

101 Jiang, Z. C.; Xiao, Y. Y.; Tong, X.; Zhao, Y., *Angew. Chem. Int. Ed.* **2019,** *58*, 5332-5337.

102 Yang, R.; Zhao, Y., *Angew. Chem. Int. Ed.* **2017,** *56*, 14202-14206.

103 Yang, R.; Zhao, Y., *ACS Macro Lett.* **2018,** *7*, 353-357.

104 Liu, L.; Liu, M. H.; Deng, L. L.; Lin, B. P.; Yang, H., *J. Am. Chem. Soc.* **2017,** *139*, 11333-11336.

105 Naciri, J.; Srinivasan, A.; Jeon, H.; Nikolov, N.; Keller, P.; Ratna, B. R., *Macromolecules* **2003,** *36*, 8499-8505.

106 Ohm, C.; Morys, M.; Forst, F. R.; Braun, L.; Eremin, A.; Serra, C.; Stannarius, R.; Zentel, R., *Soft Matter* **2011,** *7*, 3730.

107 Agrawal, A.; Yun, T.; Pesek, S. L.; Chapman, W. G.; Verduzco, R., *Soft Matter* **2014,** *10*, 1411-1415.

108 Pei, Z.; Yang, Y.; Chen, Q.; Terentjev, E. M.; Wei, Y.; Ji, Y., *Nat. Mater.* **2014,** *13*, 36-41.

109 Yang, Y.; Pei, Z.; Li, Z.; Wei, Y.; Ji, Y., *J. Am. Chem. Soc.* **2016,** *138*, 2118-2121.

110 Li, Z.; Yang, Y.; Wang, Z.; Zhang, X.; Chen, Q.; Qian, X.; Liu, N.; Wei, Y.; Ji, Y., *J. Mater. Chem. A* **2017,** *5*, 6740-6746.

111 Kotikian, A.; Truby, R. L.; Boley, J. W.; White, T. J.; Lewis, J. A., *Adv. Mater.* **2018,** *30*, 1706164.

112 Ambulo, C. P.; Burroughs, J. J.; Boothby, J. M.; Kim, H.; Shankar, M. R.; Ware, T. H., *ACS Appl. Mater. Interfaces* **2017,** *9*, 37332-37339.

113 Lopez-Valdeolivas, M.; Liu, D.; Broer, D. J.; Sanchez-Somolinos, C., *Macromol. Rapid Commun.* **2018,** *39*, 1700710.

114 Saed, M. O.; Ambulo, C. P.; Kim, H.; De, R.; Raval, V.; Searles, K.; Siddiqui, D. A.; Cue, J. M. O.; Stefan, M. C.; Shankar, M. R.; Ware, T. H., *Adv. Funct. Mater.* **2019,** *29*, 1806412.

115 Nocentini, S.; Martella, D.; Parmeggiani, C.; Zanotto, S.; Wiersma, D. S., *Adv. Opt. Mater.* **2018,** *6*, 1800167.

116 Zeng, H.; Wasylczyk, P.; Parmeggiani, C.; Martella, D.; Burresi, M.; Wiersma, D. S., *Adv. Mater.* **2015,** *27*, 3883-3887.

117 Zeng, H.; Martella, D.; Wasylczyk, P.; Cerretti, G.; Lavocat, J. C.; Ho, C. H.; Parmeggiani, C.; Wiersma, D. S., *Adv. Mater.* **2014,** *26*, 2319-2322.

118 White, T. J.; Broer, D. J., *Nat. Mater.* **2015,** *14*, 1087-1098.

119 de Haan, L. T.; Sanchez-Somolinos, C.; Bastiaansen, C. M.; Schenning, A. P.; Broer, D. J., *Angew. Chem. Int. Ed.* **2012,** *51*, 12469-12472.

120 Liu, D.; Broer, D. J., *Langmuir* **2014,** *30*, 13499-13509.

121 Ichimura, K., *Chem. Rev.* **2000,** *100*, 1847-1874.

122 Yaroshchuk, O.; Reznikov, Y., *J. Mater. Chem.* **2012,** *22*, 286-300.

123 Lee, K. W.; Paek, S. H.; Lien, A.; Durning, C.; Fukuro, H., *Macromolecules* **1996,** *29*, 8894-8899.

124 Thomsen, D. L.; Keller, P.; Naciri, J.; Pink, R.; Jeon, H.; Shenoy, D.; Ratna, B. R., *Macromolecules* **2001,** *34*, 5868-5875.

125 Xia, Y.; Cedillo-Servin, G.; Kamien, R. D.; Yang, S., *Adv. Mater.* **2016,** *28*, 9637-9643.

126 Ware, T. H.; McConney, M. E.; Wie, J. J.; Tondiglia, V. P.; White, T. J., *Science* **2015,** *347*, 982.

127 Ahn, S.-k.; Ware, T. H.; Lee, K. M.; Tondiglia, V. P.; White, T. J., *Adv. Funct. Mater.* **2016,** *26*, 5819-5826.

128 McConney, M. E.; Martinez, A.; Tondiglia, V. P.; Lee, K. M.; Langley, D.; Smalyukh, II; White, T. J., *Adv. Mater.* **2013,** *25*, 5880-5885.

129 Liu, L.; Geng, B.; Sayed, S. M.; Lin, B. P.; Keller, P.; Zhang, X. Q.; Sun, Y.; Yang, H., *Chem. Commun.* **2017,** *53*, 1844-1847.

130 Lee, K. M.; Bunning, T. J.; White, T. J., *Adv. Mater.* **2012,** *24*, 2839-2843.

131 Wie, J. J.; Lee, K. M.; Smith, M. L.; Vaia, R. A.; White, T. J., *Soft Matter* **2013,** *9*, 9303.

132 Elias, A. L.; Harris, K. D.; Bastiaansen, C. W. M.; Broer, D. J.; Brett, M. J., *J. Mater. Chem.* **2006,** *16*, 2903-2912.

133 Iamsaard, S.; Aßhoff, S. J.; Matt, B.; Kudernac, T.; Cornelissen, J. J.; Fletcher, S. P.; Katsonis, N., *Nat. Chem.* **2014,** *6*, 229-235.

134 Yao, Y.; Waters, J. T.; Shneidman, A. V.; Cui, J.; Wang, X.; Mandsberg, N. K.; Li, S.; Balazs, A. C.; Aizenberg, J., *Proc. Natl. Acad. Sci. U. S. A.* **2018,** *115*, 12950-12955.

135 Rogóż, M.; Zeng, H.; Xuan, C.; Wiersma, D. S.; Wasylczyk, P., *Adv. Opt. Mater.* **2016,** *4*, 1689-1694.

136 Zeng, H.; Wani, O. M.; Wasylczyk, P.; Priimagi, A., *Macromol. Rapid Commun.* **2018,** *39*, 1700224.

137 Camacho-Lopez, M.; Finkelmann, H.; Palffy-Muhoray, P.; Shelley, M., *Nat. Mater.* **2004,** *3*, 307.

138 Palagi, S.; Mark, A. G.; Reigh, S. Y.; Melde, K.; Qiu, T.; Zeng, H.; Parmeggiani, C.; Martella, D.; Sanchez-Castillo, A.; Kapernaum, N.; Giesselmann, F.; Wiersma, D. S.; Lauga, E.; Fischer, P., *Nat. Mater.* **2016,** *15*, 647-653.

139 Serak, S.; Tabiryan, N.; Vergara, R.; White, T. J.; Vaia, R. A.; Bunning, T. J., *Soft Matter* **2010,** *6*, 779-783.

140 Gelebart, A. H.; Vantomme, G.; Meijer, E. W.; Broer, D. J., *Adv. Mater.* **2017,** *29*, 1606712.

141 Kumar, K.; Knie, C.; Bleger, D.; Peletier, M. A.; Friedrich, H.; Hecht, S.; Broer, D. J.; Debije, M. G.; Schenning, A. P., *Nat. Commun.* **2016,** *7*, 11975.

142 Gelebart, A. H.; Jan Mulder, D.; Varga, M.; Konya, A.; Vantomme, G.; Meijer, E. W.; Selinger, R. L. B.; Broer, D. J., *Nature* **2017,** *546*, 632-636.

143 Wei, W.; Zhang, Z.; Wei, J.; Li, X.; Guo, J., *Adv. Opt. Mater.* **2018**, *6*, 1800131.

144 White, T. J.; Tabiryan, N. V.; Serak, S. V.; Hrozhyk, U. A.; Tondiglia, V. P.; Koerner, H.; Vaia, R. A.; Bunning, T. J., *Soft Matter* **2008,** *4*, 1796.

145 Vantomme, G.; Gelebart, A. H.; Broer, D. J.; Meijer, E. W., *Tetrahedron* **2017,** *73*, 4963-4967.

146 Wie, J. J.; Shankar, M. R.; White, T. J., *Nat. Commun.* **2016,** *7*, 13260.

147 Ahn, C.; Li, K.; Cai, S., *ACS Appl. Mater. Interfaces* **2018,** *10*, 25689-25696.

148 Martella, D.; Nocentini, S.; Nuzhdin, D.; Parmeggiani, C.; Wiersma, D. S., *Adv. Mater.* **2017,** *29*, 1704047.

149 Wani, O. M.; Zeng, H.; Priimagi, A., *Nat. Commun.* **2017,** *8*, 15546.

150 Wang, C.; Sim, K.; Chen, J.; Kim, H.; Rao, Z.; Li, Y.; Chen, W.; Song, J.; Verduzco, R.; Yu, C., *Adv. Mater.* **2018,** *30*, 1706695.

151 de Haan, L. T.; Verjans, J. M.; Broer, D. J.; Bastiaansen, C. W.; Schenning, A. P., *J. Am. Chem. Soc.* **2014,** *136*, 10585-10588.

152 de Haan, L. T.; Gimenez-Pinto, V.; Konya, A.; Nguyen, T.-S.; Verjans, J. M. N.; Sánchez-Somolinos, C.; Selinger, J. V.; Selinger, R. L. B.; Broer, D. J.; Schenning, A. P. H. J., *Adv. Funct. Mater.* **2014,** *24*, 1251-1258.

153 Yang, L.; Setyowati, K.; Li, A.; Gong, S.; Chen, J., *Adv. Mater.* **2008,** *20*, 2271-2275.

154 Yang, Y.; Zhan, W.; Peng, R.; He, C.; Pang, X.; Shi, D.; Jiang, T.; Lin, Z., *Adv. Mater.* **2015,** *27*, 6376-6381.

155 Bisoyi, H. K.; Urbas, A. M.; Li, Q., *Adv. Opt. Mater.* **2018,** *6*, 1800458.

156 Marshall, J. E.; Terentjev, E. M., *Soft Matter* **2013,** *9*, 8547.

157 Vantomme, G.; Gelebart, A. H.; Broer, D. J.; Meijer, E. W., *J. Polym. Sci. Poly. Chem.* **2018,** *56*, 1331-1336.

158 Herbert, K. M.; Schrettl, S.; Rowan, S. J.; Weder, C., *Macromolecules* **2017,** *50*, 8845-8870.

159 Wang, M.; Sayed, S. M.; Guo, L.-X.; Lin, B.-P.; Zhang, X.-Q.; Sun, Y.; Yang, H., *Macromolecules* **2016,** *49*, 663-671.

160 Yang, H.; Buguin, A.; Taulemesse, J.-M.; Kaneko, K.; Méry, S.; Bergeret, A.; Keller, P., *J. Am. Chem. Soc.* **2009,** *131*, 15000-15004.

161 Wang, X. Q.; Tan, C. F.; Chan, K. H.; Lu, X.; Zhu, L.; Kim, S. W.; Ho, G. W., *Nat. Commun.* **2018,** *9*, 3438.

162 Wang, Y.; Wang, C.; Song, X.; Megarajan, S. K.; Jiang, H., *J. Mater. Chem. A* **2018,** *6*, 963-971.

163 Lu, X.; Guo, S.; Tong, X.; Xia, H.; Zhao, Y., *Adv. Mater.* **2017,** *29*, 1606467.

164 Dong, L.; Zhao, Y., *Mater. Chem. Frontiers* **2018,** *2*, 1932-1943.

165 Li, J.; Turunen, M.; Niiranen, S.; Chen, H.; Paulasto-Kröckel, M., *Microelectron. Reliab.* **2012,** *52*, 2962-2969.